

AO-A101 991

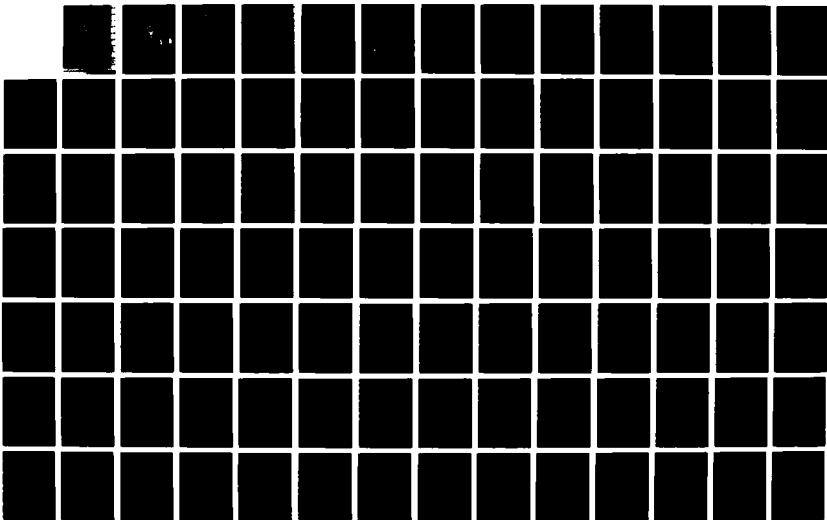
IMPORTANCE OF ROTATION SHEAR STRESS FOR ENTRAINMENT IN  
THE OCEAN MIXED LAYER(U) NAVAL POSTGRADUATE SCHOOL  
MONTEREY CA P C GALLACHER JUN 87

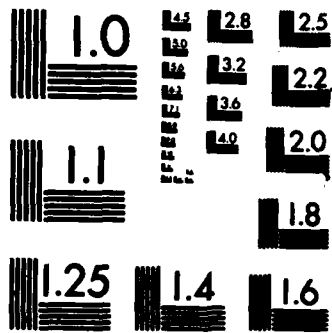
1/2

UNCLASSIFIED

F/G 8/3

NL





MICROCOPY RESOLUTION TEST CHART  
NATIONAL BUREAU OF STANDARDS-1963-A

AD-A181 991

2

DTIC FILE COPY

# NAVAL POSTGRADUATE SCHOOL

Monterey, California



DTIC  
ELECTE  
JUL 08 1987  
S E D

## THESIS

IMPORTANCE OF ROTATION SHEAR STRESS  
FOR  
ENTRAINMENT IN THE OCEAN MIXED LAYER

by

Patrick C. Gallacher

June 1987

Dissertation Supervisor:

R. W. Garwood, Jr.

Approved for public release; Distribution is unlimited

## **DISCLAIMER NOTICE**

**THIS DOCUMENT IS BEST QUALITY PRACTICABLE. THE COPY FURNISHED TO DTIC CONTAINED A SIGNIFICANT NUMBER OF PAGES WHICH DO NOT REPRODUCE LEGIBLY.**

AD-A181 991

REPORT DOCUMENTATION PAGE

1a REPORT SECURITY CLASSIFICATION <b>Unclassified</b>		1b RESTRICTIVE MARKINGS	
2a SECURITY CLASSIFICATION AUTHORITY		3 DISTRIBUTION/AVAILABILITY OF REPORT Approved for public release; Distribution is unlimited.	
2b DECLASSIFICATION/DOWNGRADING SCHEDULE			
4 PERFORMING ORGANIZATION REPORT NUMBER(S)		5 MONITORING ORGANIZATION REPORT NUMBER(S)	
6a NAME OF PERFORMING ORGANIZATION Naval Postgraduate School	6b OFFICE SYMBOL (If applicable) 68	7a NAME OF MONITORING ORGANIZATION Naval Postgraduate School	
6c ADDRESS (City, State, and ZIP Code) Monterey, CA 93943-5000		7b ADDRESS (City, State, and ZIP Code) Monterey, CA 93943-5000	
8a NAME OF FUNDING/SPONSORING ORGANIZATION ONR, NSF	8b OFFICE SYMBOL (If applicable)	9 PROCUREMENT INSTRUMENT IDENTIFICATION NUMBER	
8c ADDRESS (City, State, and ZIP Code)		10 SOURCE OF FUNDING NUMBERS	
		PROGRAM ELEMENT NO	PROJECT NO
		TASK NO	WORK UNIT ACCESSION NO
11 TITLE (Include Security Classification) Importance of Rotation Shear Stress for Entrainment in the Ocean Mixed Layer			
12 PERSONAL AUTHOR(S) Gallacher, Patrick C.			
13a TYPE OF REPORT PhD Dissertation	13b TIME COVERED FROM TO	14 DATE OF REPORT (Year, Month Day) 1987 June	15 PAGE COUNT 143
16 SUPPLEMENTARY NOTATION			
17 COSATI CODES		18 SUBJECT TERMS (Continue on reverse if necessary and identify by block number)	
FIELD	GROUP	→ Air-Sea Interactions; Upper Ocean Processes	
		Coriolis Effects	
		Turbulence and Mixing Processes	
19 ABSTRACT (Continue on reverse if necessary and identify by block number) The interaction of the northward component of planetary rotation and the east-west Reynolds stress affects the isotropy of the integral scale turbulence in the upper ocean by redistributing turbulent kinetic energy (TKE) among the components. This "rotation stress" mechanism is incorporated into a vertically integrated model of the ocean mixed layer. Simulations of Ocean Weather Stations P (50°N, 145°W) and N (30°N, 140°W) are used to compare this model with the Garwood (1977) model and with observations. The significant effect is the augmentation (for easterly winds) or reduction (for westerly winds) of the ratio of vertical to horizontal TKE. The rate of entrainment is affected by the change in the vertical convergence of TKE at the interface between the mixed layer and the pycnocline. Rotation stress significantly alters the mixing on diurnal to synoptic time scales during late winter and early spring. With rotation stress, retreat is 10-30% greater than without rotation stress. Typically, the ratio of vertical to total TKE is three times larger when rotation stress is included and the dissipation enhancement of Garwood (1977) is neglected.			
20 DISTRIBUTION/AVAILABILITY OF ABSTRACT <input checked="" type="checkbox"/> UNCLASSIFIED/UNLIMITED <input type="checkbox"/> SAME AS RPT <input type="checkbox"/> DTIC USERS		21 ABSTRACT SECURITY CLASSIFICATION Unclassified	
22a NAME OF RESPONSIBLE INDIVIDUAL R. W. Garwood, Jr.		22b TELEPHONE (Include Area Code) 408-646-3260	22c OFFICE SYMBOL 68Gd

UNCLASSIFIED

SECURITY CLASSIFICATION OF THIS PAGE (When Data Entered)

The resulting TKE distribution is more isotropic and in better agreement with laboratory results for neutrally stratified shear flows. This study demonstrates the need for measurements of the TKE budget in the upper ocean to confirm these findings and to further test the hypotheses of TKE models in oceanic applications. *Keywords: field 18*

Accession For	
NTIS GRA&I	<input checked="" type="checkbox"/>
DTIC TAB	<input type="checkbox"/>
Unannounced	<input type="checkbox"/>
Justification	
By _____	
Distribution/	
Availability Codes	
Dist	Avail and/or Special
A-1	



Approved for public release; distribution is unlimited.

**Importance of Rotation Shear Stress  
for  
Entrainment in the Ocean Mixed Layer**

by

Patrick C. Gallacher  
B.S., Xavier University, 1972  
M.S., Physics, University of Cincinnati, 1974  
M.S., Oceanography, Oregon State University, 1978

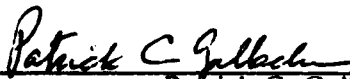
Submitted in partial fulfillment of the  
requirements for the degree of

**DOCTOR OF PHILOSOPHY IN PHYSICAL OCEANOGRAPHY**

from the

**NAVAL POSTGRADUATE SCHOOL  
June 1987**

Author:

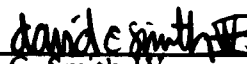
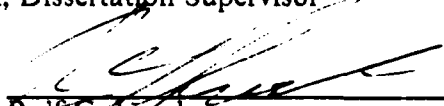


Patrick C. Gallacher

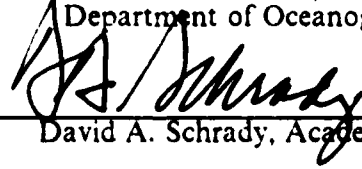
Approved by:



Roland W. Garwood, Jr.  
Associate Professor of Oceanography  
Committee Chairman, Dissertation Supervisor

  
David C. Smith IV  
Assistant Professor of Oceanography  
Rolf G. Lueck  
Chesapeake Bay Institute  
Johns Hopkins University  
Herman Medwin  
Professor Emeritus of Physics  
Russell L. Elsberry  
Professor of Meteorology

Edward B. Thornton, Chairman,  
Department of Oceanography

  
David A. Schrady, Academic Dean

## ABSTRACT

The interaction of the northward component of planetary rotation and the east-west Reynolds stress affects the isotropy of the integral scale turbulence in the upper ocean by redistributing turbulent kinetic energy (TKE) among the components. This "rotation stress" mechanism is incorporated into a vertically integrated model of the ocean mixed layer. Simulations of Ocean Weather Stations P ( $50^{\circ}\text{N}$ ,  $145^{\circ}\text{W}$ ) and N ( $30^{\circ}\text{N}$ ,  $140^{\circ}\text{W}$ ) are used to compare this model with the Garwood (1977) model and with observations. The significant effect is the augmentation (for easterly winds) or reduction (for westerly winds) of the ratio of vertical to horizontal TKE. The rate of entrainment is affected by the change in the vertical convergence of TKE at the interface between the mixed layer and the pycnocline. Rotation stress significantly alters the mixing on diurnal to synoptic time scales during late winter and early spring. With rotation stress, retreat events occur more frequently, and the mixed layer depth change during retreat is 10-30% greater than without rotation stress. Typically, the ratio of vertical to total TKE is three times larger when rotation stress is included and the dissipation enhancement of Garwood (1977) is neglected. The resulting TKE distribution is more isotropic and in better agreement with laboratory results for neutrally stratified shear flows. This study demonstrates the need for measurements of the TKE budget in the upper ocean to confirm these findings and to further test the hypotheses of TKE models in oceanic applications.



## TABLE OF CONTENTS

I.	INTRODUCTION .....	11
A.	STATEMENT OF THE PROBLEM AND PLAN OF ATTACK .....	11
B.	BACKGROUND .....	13
1.	Governing equations and definitions of terms .....	13
2.	A Physical Mechanism .....	18
3.	The Closure Problem and Parameterizations .....	20
C.	HYPOTHESES .....	26
II.	LITERATURE REVIEW .....	29
A.	BULK OCEAN MIXED LAYER MODELS .....	29
B.	STUDIES OF THE EFFECTS OF ROTATION ON TURBULENT FLOWS .....	31
C.	PRESSURE-RATE OF STRAIN PARAMETERIZATIONS .....	37
III.	THEORY .....	39
A.	MODEL DEVELOPMENT .....	39
B.	NONDIMENSIONAL EQUATIONS .....	44
C.	IMPLICATIONS FOR THE ENERGY BUDGET .....	48
D.	COMPARISON OF RSTAR AND ZSTAR MODELS .....	50
IV.	SIMULATIONS .....	54
A.	SURFACE FLUX CALCULATIONS .....	56
B.	DESCRIPTION OF OCEAN WEATHER STATION DATA .....	57
C.	SYNOPTIC-SCALE INTERCOMPARISONS OF MODELS .....	60
D.	TUNING USING ANNUAL SIMULATIONS .....	69
E.	SEASONAL AND ANNUAL SCALE INTERCOMPARISONS OF MODELS .....	73

V. SUMMARY AND RECOMMENDATIONS .....	81
APPENDIX : FIGURES .....	85
LIST OF REFERENCES .....	132
INITIAL DISTRIBUTION LIST .....	140

## LIST OF TABLES

1. NUMERICAL VALUES OF $\gamma_1$ FROM ZEMAN AND TENNEKES (1975) .....	25
2. THE NONDIMENSIONAL VARIABLES .....	45
3. THE RSTAR MODEL: $P_* = P_*(R_*, H_*)$ .....	46
4. THE ZSTAR MODEL: $P_* = P_*(Z_*, H_*)$ .....	46
5. THE HSTAR MODEL: $P_* = P_*(H_*)$ .....	46
6. DIMENSIONAL, DEPTH-AVERAGED VARIABLES .....	49
7. ANNUAL AVERAGE SURFACE FLUXES AT OWS P AND N .....	60
8. ESTIMATES OF THE ISOTROPY OF WALL-BOUNDED SHEAR LAYERS .....	68
9. MODEL CONSTANTS FOR OWS SIMULATIONS .....	73
10. COMPARISON OF MODELS AT OWS P, 1967 .....	78
11. COMPARISON OF MODELS AT OWS P, 1965 .....	79
12. COMPARISON OF MODELS AT OWS P, 1966 .....	79
13. COMPARISON MODELS AT OWS P, 1961 .....	80
14. COMPARISON OF MODELS AT OWS N, 1961 .....	80

## LIST OF FIGURES

1.1	The elongation of turbulent eddies by planetary vorticity .....	85
1.2	Mean density and velocity profiles in the upper ocean .....	86
1.3	$L_{\Omega}$ vs. the ratio of rotation stress to buoyancy flux .....	87
2.1	The Obukhov depth ( $L_o$ ) vs. longitude at the equator .....	88
2.2	As in Figure 2.1, except the equilibrium depth is $L_{\Omega}$ .....	89
2.3	Schematic of the rotating channel of Johnston <i>et al.</i> (1972) .....	90
2.4	Orientation of rotation stress compared to curvature stress .....	91
3.1	Schematic of TKE budget including entrainment .....	92
3.2a	$P_*(H_*, Z_*)$ , nondimensional entrainment rate for ZSTAR .....	93
3.2b	$P_*(H_*, R_*)$ , for the RSTAR model. $R_* > 0$ for westerly winds .....	94
3.3a	$W_*^2/E_*$ , vertical over total nondimensional TKE for ZSTAR .....	95
3.3b	$W_*^2/E_*$ , for the RSTAR model. $R_* > 0$ for westerly winds .....	96
4.1a	The distribution of XBT casts at OWS P for 1961 .....	97
4.1b	The distribution of XBT casts at OWS P for 1965 .....	98
4.1c	The distribution of XBT casts at OWS P for 1966 .....	99
4.1d	The distribution of XBT casts at OWS P for 1967 .....	100
4.1e	The distribution of XBT casts at OWS N for 1961 .....	101
4.2	1967 Days 101-108, OWS P, a) h, b) D, c) P for RSTAR, HSTAR, ZSTAR .....	102
4.2	1967 Days 101-108, OWS P, d) G, b) R, c) H for RSTAR, HSTAR, ZSTAR .....	103
4.2	1967 Days 101-108, OWS P, g) E, h) $W^2/E$ , i) $\Pi$ -R .....	104
4.3	1965 Days 72-80, OWS P, a) h, b) D, c) P for RSTAR, HSTAR, ZSTAR .....	105
4.3	1965 Days 72-80, OWS P, d) G, b) R, c) H for RSTAR, HSTAR, ZSTAR .....	106
4.3	1965 Days 72-80, OWS P, g) E, h) $W^2/E$ , i) $\Pi$ -R .....	107
4.4	1961 Days 77-84, OWS P, a) h, b) D, c) P for RSTAR, HSTAR, ZSTAR .....	108

4.4	1961 Days 77-84, OWS P, d) G, b) R, c) H for RSTAR, HSTAR, ZSTAR .....	109
4.4	1961 Days 77-84, OWS P, g) E, h) $W^2/E$ , i) $\Pi$ -R .....	110
4.5	1967 Days 210-217, OWS P, a) h, b) D, c) P for RSTAR, HSTAR, ZSTAR .....	111
4.5	1967 Days 210-217, OWS P, d) G, b) R, c) H for RSTAR, HSTAR, ZSTAR .....	112
4.5	1967 Days 210-217, OWS P, g) E, h) $W^2/E$ , i) $\Pi$ -R .....	113
4.6	1967 Days 250-257, OWS P, a) h, b) D, c) P for RSTAR, HSTAR, ZSTAR .....	114
4.6	1967 Days 250-257, OWS P, d) G, b) R, c) H for RSTAR, HSTAR, ZSTAR .....	115
4.6	1967 Days 250-257, OWS P, g) E, h) $W^2/E$ , i) $\Pi$ -R .....	116
4.7a	Annual depth bias from tuning of RSTAR model for 1965 at OWS P .....	117
4.7b	Annual depth RMSE from tuning of RSTAR model for 1965 at OWS P .....	118
4.8a	Same as Figure 4.7a, except for temperature .....	119
4.8b	Same as Figure 4.7b, except for temperature .....	120
4.9	Annual simulations with the ZSTAR and HSTAR for 1965 at OWS P .....	121
4.10a	OWS P, 1961, mixed layer depth: observations, RSTAR and ZSTAR .....	122
4.10b	OWS P, 1961, mixed layer temperature: observations, RSTAR and ZSTAR .....	123
4.11a	OWS P, 1965, mixed layer depth: observations, RSTAR and ZSTAR .....	124
4.11b	OWS P, 1965, mixed layer temperature: observations, RSTAR and ZSTAR .....	125
4.12a	OWS P, 1966, mixed layer depth: observations, RSTAR and ZSTAR .....	126
4.12b	OWS P, 1966, mixed layer temperature: observations, RSTAR and ZSTAR .....	127
4.13a	OWS P, 1967, mixed layer depth: observations, RSTAR and ZSTAR .....	128
4.13b	OWS P, 1967, mixed layer temperature: observations, RSTAR and ZSTAR .....	129
4.14a	OWS N, 1961, mixed layer depth: observations, RSTAR and ZSTAR .....	130
4.14b	OWS N, 1961, mixed layer temperature: observations, RSTAR and ZSTAR .....	131

## ACKNOWLEDGEMENTS

Dr. Roland Garwood, Jr., my dissertation supervisor and committee chairman, provided the support, guidance and advice that made this research possible. I greatly appreciate his time and efforts spent on my behalf.

The many discussions with members of my committee, both individually and collectively, were very helpful and stimulating, and are greatly appreciated. Profs. Glen H. Jung, Thomas R. Osborn and Christopher N. K. Mooers served on my committee at various times prior to my defense. Their help is also appreciated.

I would like to thank Mr. Paul Martin for providing the surface forcing and BT data for 1961 at OWS N and P. I am also indebted to Mr. Martin for several discussions regarding the meteorological and oceanic observations, the bulk formulas used to calculate the surface fluxes, and simulations of the upper ocean at the Ocean Weather Stations. The meteorological observations and BT data for 1965, 1966 and 1967 at OWS P were obtained from the National Oceanographic Data Center.

Lastly, I wish to thank my wife, Deborah, for her continuous support and encouragement during the course of this research. Without her this work would never have been completed. I also wish to thank my son, Jordan, for his companionship during the last few late night sessions which saw this dissertation through to completion.

This research was funded by the Office of Naval Research under Contracts N00014-87-WR-24018, N00014-84-WR-24051 and N00014-82-C-03808 and through the Naval Postgraduate School Foundation Research Program. Computer time was provided by the W. R. Church Computer Center at the Naval Postgraduate School.

## I. INTRODUCTION

This dissertation is a study of one process by which planetary rotation affects the turbulent kinetic energy (TKE) budget in the well-mixed layer of the upper ocean. The process is the coupling of the east-west and vertical TKE components by the interaction of the northward component of planetary rotation and the east-west Reynolds stress. This results in a redistribution of TKE between the horizontal and the vertical TKE components.

Turbulent kinetic energy is primarily generated near the sea surface by the turbulent fluxes of momentum and buoyancy. The entrainment of nonturbulent fluid into the mixed layer occurs at the base of the mixed layer. Thus, the rate of mixed layer deepening depends on the vertical convergence of TKE at the interface between the fully turbulent ocean planetary boundary layer (OPBL) and the underlying pycnocline (Garwood, 1977). The average rate of vertical turbulent transport through the OPBL to the interface (entrainment zone) is proportional to the root mean square vertical turbulent velocity averaged over the mixed layer. Both the magnitude of the vertical TKE averaged over the mixed layer and the magnitude of the total TKE are important to the dynamics of the upper ocean mixed layer.

Through the rotation stress, that is the interaction of the northward component of planetary rotation and the east-west Reynolds stress, the mixed layer dynamics is predicted to depend on latitude and wind direction. The transfer of energy increases the east-west component of TKE and decreases the vertical TKE for westerly winds (eastward surface Reynolds stress). The decrease in the vertical TKE reduces the convergence of TKE to the entrainment zone and reduces the rate of mixed layer deepening. Conversely, the rate of deepening is augmented for easterly winds (westward surface Reynolds stress).

### A. STATEMENT OF THE PROBLEM AND PLAN OF ATTACK

This study will explore the diurnal, synoptic and annual variations in mixed layer dynamics which result from rotation stress for mid latitude mixed layers in both easterly and westerly wind regimes. A vertically integrated, second-order closure model of the OPBL will be used to calculate the time-dependent mixed layer depth and temperature and the distribution of energy between the horizontal and vertical TKE components.

The time scales for rotation stress are the earth's rotation time scale and the time scale for variations in the wind direction. The diurnal to synoptic time frame encompasses these time scales. On diurnal time scales, the mixed layer frequently retreats in response to the solar insolation then deepens at night. On synoptic time scales, increases or decreases in surface wind stress and solar insolation caused by the passage of atmospheric low pressure systems can cause the mixed layer to deepen or retreat. Following the passage of the disturbance, the mixed layer will readjust to the local atmospheric conditions and may return to approximately the same depth which existed prior to the event. For these time scales, the rotation stress may significantly alter the frequency and vertical scale of these shallowing and deepening events depending on the variations in wind direction throughout the event. This is particularly likely for cases when the wind shear production and the surface buoyant damping of TKE are nearly equal and the mixed layer is deep  $O(100m)$ .

Previous studies of the mid latitude OPBL have demonstrated that the annual cycle of mixed layer shallowing and deepening is poorly simulated unless the dissipation is increased during times of increased buoyant production of TKE (see Zilitinkevich, 1979 and Garwood, 1979 for reviews). Consequently, the dissipation in mixed layer models has been augmented in various ways to prevent excessive wintertime mixed layer deepening. The need for this enhancement of the dissipation indicates that physical processes that are important for mixed layer dynamics are not being included in the models or that the processes are being modeled incompletely. Although rotation stress has been shown to be important for the equilibrium mixed layer depth in the tropics (Garwood *et al.*, 1985b), it has not previously been included in a model of the time-dependent mixed layer. For westerly wind regimes, it is possible that the reduction in the entrainment rate due to rotation stress may reduce or eliminate the need for enhanced dissipation. Conversely, it may not be possible to achieve a neutral equilibrium depth for the OPBL based on local surface forcing for regions of predominately easterly winds. In the latter case, a net downward heat flux or a three-dimensional circulation may be required to achieve a closed annual cycle for the mixed layer depth in easterly wind regimes.

The next section of this dissertation gives the background necessary for this study. The governing equations are given, and the terms are defined and discussed. Then a physical mechanism is proposed to explain the rotation stress. The turbulence closure problem and the resulting need for parameterizations are addressed. The



parameterizations for rotation stress and dissipation are discussed briefly. The parameterization of the pressure-rate of strain term is discussed in some detail because it contains terms which, in theory, could counter the effects of the rotation stress terms. In the final section, the hypotheses and tests of these hypotheses are put forward.

Chapter II contains the literature review in three sections. The first section deals with the development of vertically integrated (bulk) mixed layer models. The second section reviews previous work concerning the effects of rotation on turbulent boundary layers. The effects of streamline curvature are also reviewed since they are mathematically identical to those for rotation. Finally, the problems involved in parameterizing the pressure-rate of strain terms are reviewed since this parameterization affects the results of this work.

In Chapter III, the vertically-integrated equations for the TKE components are developed and discussed. The nondimensional equations are derived for the models that will be used in this study. The TKE budget is examined to highlight the differences between the processes that are explored in this dissertation. The models are compared using the nondimensional framework introduced by Garwood (1977) and used for model intercomparison in Garwood (1979).

Chapter IV contains a description of the data sets extracted from Ocean Weather Station (OWS) data archives, which will be used for the simulations in this study. The results of the annual simulations are discussed for synoptic, seasonal and annual time scales. The effects of adjusting the tuning constants are also explored. Chapter V contains a summary of the conclusions and recommendations resulting from this study.

## **B. BACKGROUND**

### **1. Governing equations and definitions of terms**

The upper ocean mixed layer is approximately horizontally homogeneous if the smallest term involving vertical derivatives is sufficiently larger than the largest term involving horizontal derivatives. To formally determine if this criterion is met, all the terms in the TKE budget must be approximated systematically and the order of approximation at which different terms are eliminated must be analyzed. Pedlosky (1979) applies this technique in detail to derive the shallow water equations. However, Businger (1982) points out that the assumption of horizontal homogeneity is usually valid if  $h/L < 1$ , where  $h$  is a length scale for the vertical and  $L$  is a horizontal length scale. Since the TKE in the upper ocean responds to the local atmospheric forcing,

one relevant horizontal length scale in the mid latitudes would be that of extratropical cyclones. This length scale is  $L_s = \sqrt{g'Z_0/T} \sim 1000$  km, where  $g' = g(\rho_o - \rho)/\rho_o$  is the reduced gravity. This length scale is the baroclinic Rossby radius for the atmospheric synoptic scale with a vertical scale height  $Z \sim 10$  km (Pedlosky, 1979). The mean dynamical variables in the ocean have a synoptic spatial scale of  $L_r = \sqrt{g'Z_0/f} \sim 30$  km where  $Z_0$  is the depth scale of the permanent pycnocline  $O(500$  m). For  $L$  equal to  $L_r$  or  $L_s$ ,  $h/L \ll 1$  and horizontal homogeneity is a valid assumption. Since  $L_s > L_r$ , horizontal homogeneity is probably a better assumption for the TKE budget than for the mean flow.

A set of three equations describes the TKE budget in the OPBL. The equations are derived using Reynolds decomposition (Tennekes and Lumley, 1972). The origin of the coordinate system is at the sea surface,  $x$  is eastward,  $y$  is northward and  $z$  is upward. For the components of TKE, which are the normal Reynolds stresses, the equations are:

$$\frac{\partial \overline{u^2}}{\partial t} = \underbrace{-\overline{uw}}_{G.1} \frac{\partial \overline{U}}{\partial z} - \underbrace{\frac{\partial \overline{wu^2}}{\partial z}}_{P.1} - \underbrace{\frac{\overline{p\partial u}}{\rho\partial x}}_{\Pi.1} + \underbrace{f\overline{uv}}_{R.3} - \underbrace{2\Omega_y \overline{uw}}_{R.1} - \underbrace{\frac{\epsilon}{3}}_{D.1} \quad (1.1)$$

$$\frac{\partial \overline{v^2}}{\partial t} = \underbrace{-\overline{vw}}_{G.2} \frac{\partial \overline{V}}{\partial z} - \underbrace{\frac{\partial \overline{wv^2}}{\partial z}}_{P.2} - \underbrace{\frac{\overline{p\partial v}}{\rho\partial y}}_{\Pi.2} - \underbrace{f\overline{uv}}_{R.4} - \underbrace{\frac{\epsilon}{3}}_{D.2} \quad (1.2)$$

$$\frac{\partial \overline{w^2}}{\partial t} = \underbrace{-\overline{wb}}_{H} - \underbrace{\frac{\partial \overline{ww^2}}{\partial z}}_{P.3} - \underbrace{\frac{\overline{p\partial w}}{\rho\partial z}}_{\Pi.3} - \underbrace{\frac{\partial \overline{wp}}{\rho\partial z}}_{P.4} + \underbrace{2\Omega_y \overline{uw}}_{R.2} - \underbrace{\frac{\epsilon}{3}}_{D.3} \quad (1.3)$$

Here, the lower case letters represent fluctuations of the variables about the means, which are shown as upper case letters. The overbars represent ensemble averages.

Turbulence is isotropic if the statistically averaged properties of the flow are invariant under arbitrary rotation and reflection of the coordinate system (Hinze, 1975). A consequence of isotropy is that the TKE would be distributed equally among the components ( $\overline{u^2}$ ,  $\overline{v^2}$  and  $\overline{w^2}$ ) in (1.1), (1.2) and (1.3). The OPBL is inherently anisotropic, as are all turbulent shear flows, since the mean shear imposes a preferred direction. The generation, transport and redistribution of turbulence in such mixing layers is a direct consequence of this anisotropy. The TKE distribution among  $\overline{u^2}$ ,  $\overline{v^2}$  and  $\overline{w^2}$  is anisotropic since the the shear production (G.1 and G.2) generates TKE only

in the  $\overline{u^2}$  and  $\overline{v^2}$  components (1.1 and 1.2), and the buoyancy production and damping (H) generates and damps TKE only in the vertical  $\overline{w^2}$  component (1.3). At the scales of the production terms, the TKE components associated with the shear production can be a factor of two larger than the other components (Townsend, 1976). The processes represented by the terms in (1.1 - 1.3) can be categorized with respect to the anisotropy of the TKE distribution. A source of TKE for the OPBL is the shear production due to the shear of the mean current and the surface wind stress, terms G.1 - G.2. Also included in these terms is a sink of TKE, the entrainment stress which is due to the entrainment of nonturbulent fluid at the base of the mixed layer. The damping due to the entrainment shear reduces only the horizontal TKE. The buoyancy flux, H, represents both the surface buoyancy flux, which can be a source or sink of vertical TKE and the entrainment buoyancy flux, which is a sink of vertical TKE. This production and damping by buoyancy flux increases the anisotropy because it alters only the vertical component of TKE (1.3).

The convergence of TKE (P.1 - P.3) at the interface between the turbulent OPBL and the dynamically stable pycnocline is a major determinant of the entrainment rate (Garwood, 1977). The entrainment rate is the rate at which nonturbulent water is entrained into the OPBL, and hence the rate at which the mixed layer deepens. The convergence of TKE depends on the vertical turbulent velocity, which scales with the square root of the vertical TKE. Thus, the anisotropy of the TKE distribution and the magnitude of the TKE are both important to mixed layer dynamics. Processes that affect the isotropy of the TKE distribution by transferring TKE between the horizontal and vertical components can significantly impact mixed layer dynamics even though they do not directly alter the total TKE. The terms that represent such processes are  $\Pi.1 - \Pi.3$ , and R.1 and R.2.

The interaction of planetary rotation and the Reynolds stresses is represented by (R.1 - R.4). These rotation stresses depend on latitude and wind direction. The northward ( $\Omega_y$ ) and vertical ( $f/2$ ) components of planetary rotation are:

$$\begin{aligned}\Omega_y &= \Omega \cos\theta, \\ f &= 2\Omega \sin\theta,\end{aligned}$$

where  $\theta$  is the latitude. The surface Reynolds stresses ( $\overline{uw}(0)$  and  $\overline{vw}(0)$ ) are the vertical flux of momentum due to the wind stress,

$$\vec{\tau} = -\rho(\overline{uw}(0) \mathbf{e}_x + \overline{vw}(0) \mathbf{e}_y) . \quad (1.4)$$

The rotation stress is the work done on the turbulent flow by the planetary rotation. For westerly surface winds (eastward or positive  $\tau_x$ ), the rotation stress transfers TKE from the vertical to the horizontal components. This reduces the vertical TKE and reduces the vertical transport of TKE which decreases the rate at which the mixed layer deepens. If the primary turbulence generation mechanism is wind shear production (forced convection), the anisotropy of the turbulence would be increased, since both the primary production (G.1 and G.2) and the rotation stress (R.1 and R.2) would be increasing the energy in the horizontal component. For forced convection regimes with easterly winds, the entrainment rate is enhanced and the turbulence becomes more isotropic through the rotation stress interaction.

The pressure-rate of strain ( $\Pi.1 - \Pi.3$ ) is the cross-correlation of the dynamic pressure fluctuations and the turbulent velocities. The dynamic pressure fluctuations result from local and remote variations in the mean or turbulent velocity field. Any convergence or divergence of velocity can set up an adverse gradient of fluctuating pressure. The pressure-rate of strain is a reaction of the turbulent flow to variations in the turbulence and to variations in the mean flow. The pressure-rate of strain due to the turbulence-turbulence interaction is comprised of the turbulent velocity gradient and the dynamic pressure fluctuations that result from variations in the turbulent velocity. The primary effect of this pressure-rate of strain interaction is to reduce the anisotropy of the turbulence by causing a transfer of TKE from the component in which most of the production is taking place to the other TKE components (Townsend, 1976). For forced convection regimes in which shear production (G.1 and G.2) is the primary production mechanism for the OPBL, this implies that the effect of the turbulence-turbulence pressure-rate of strain is to reduce the energy in the horizontal components and increase the energy in the vertical component. The other part of the pressure-rate of strain is the turbulence-mean flow interaction, which is comprised of the turbulent velocity gradient and the dynamic pressure fluctuations that result from variations in the mean velocity. The nature and effects of the turbulence-mean flow part of the pressure-rate of strain are dependent on the nature of the particular flow regime. However, there is evidence that it may be negligible for geophysical turbulent boundary layers (see Section 3).

The rotation stress (R.1 - R.4) and the pressure-rate of strain ( $\Pi.1 - \Pi.3$ ) act to redistribute TKE among the components without directly influencing the total TKE. This can be seen by summing (1.1), (1.2) and (1.3) to obtain an equation for twice the

total TKE,  $\bar{\epsilon} = \overline{u^2} + \overline{v^2} + \overline{w^2}$ . In the resulting equation, the terms R.1 - R.4 and  $\Pi.1 - \Pi.3$  sum to zero so the total TKE is not affected directly. Because many ocean mixed layer models use only the total TKE equation (see Zilitinkevich *et al.*, 1979 and Garwood, 1979 for reviews), the rotation stress and pressure-rate of strain terms are not included in those models. In other cases (e.g. Wyngaard, 1981),  $2\Omega_y \overline{uw}$  is neglected based on scaling the Reynolds equations rather than the TKE equations. In the Reynolds equations, the equivalent term is  $2\Omega_y w$ . This scales as

$$2\Omega_y w \sim \frac{f u_* h}{L_r},$$

where the ratio of  $w$  to  $u_*$  is derived from the continuity equation and  $u_*$  is a characteristic horizontal turbulent velocity scale based on the surface Reynolds stress (1.4)

$$u_*^2 \equiv \overline{\tau}(0)/\rho \sim 0.01 \text{ m s}^{-2}.$$

With the boundary layer approximation,  $h/L_r \ll 1$ , this term is much smaller than the other Coriolis term  $fu$ , since  $w \ll u_*$  from the continuity equation. Therefore it is negligible in the turbulent momentum equation. However,  $uw$  and  $vw$  are normally larger than  $uv$  since they are the Reynolds stresses associated with the surface wind stress (1.4). Thus, R.1 and R.2 are at least as large as R.3 and R.4 and these terms should be retained during the Reynolds averaging process. The importance of the rotation stress terms for the TKE budget can be determined by comparing the rotation stress to the pressure-rate of strain since these are the terms that causes a transfer energy among the TKE components (1.1-1.3). The ratio of the pressure-rate of strain to the rotation stress is

$$\frac{\overline{w \partial p}}{\rho \partial z} \sim \frac{u_*^3/h}{f u_*^2} = Ro_h. \quad (1.5)$$

So the rotation stress scales with a boundary layer Rossby number ( $Ro_h$ ) in the TKE equations. For  $u_* = 0.01 \text{ m s}^{-1}$ , which corresponds to a surface stress of  $0.1 \text{ N m}^{-2}$  (or wind speed of  $8 \text{ m s}^{-1}$  at 10 m), and  $h = 100 \text{ m}$ ,  $Ro_h = 1$ . Thus, the redistribution of TKE by rotation stress can not be neglected based on scaling arguments. The relative magnitude of the rotation stress increases with decreasing Rossby number. Therefore, rotation stress becomes relatively more important for mixed layer dynamics for deep mixed layers and low wind speeds.

The viscous dissipation ( $\epsilon = D.1 + D.2 + D.3$ ) is

$$\epsilon = \nu \overline{\left( \frac{\partial u_i}{\partial x_j} \right)^2} , \quad (1.6)$$

where  $i=1,2,3$  and  $j=1,2,3$ , corresponding to the  $x, y, z$  axis respectively. The dissipation is assumed to be isotropic, so that energy is removed equally from all three TKE components. Approximately 80 to 90% or more of the TKE produced by G.1, G.2 and H is dissipated locally by D.1 - D.3 (Tennekes and Lumley, 1972). The unsteady terms, T.1 - T.3, may augment or reduce the isotropy depending on the initial state of the turbulence and on the signs of the terms. However, these terms are usually negligible in geophysical planetary boundary layers except for time scales shorter than 100 seconds (deSzoek and Rhines, 1976 and Garwood and Yun, 1979 ).

## 2. A Physical Mechanism

Turbulence seems to exist as a collection of interspersed and interlinked vortices (eddies) of various sizes and shapes. Here, the term eddy means a spatially limited distribution of vorticity in a fairly simple pattern, such as a cylinder or roll cell, or a sphere (Townsend, 1976). The sizes range from the integral scale, which is the largest scale of the flow, to the Kolmogorov scale, which is the scale of the dissipation of TKE by molecular viscosity. The rotation stress will be most effective at the largest scales of the turbulent flow since the ratio of the pressure-rate of strain to the rotation stress is proportional to  $1/h$  (1.5). Thus the effect of rotation stress will be examined for a roll vortex with the rotation axis oriented north-south (along the  $y$  axis of the reference frame) and with a scale normal to the rotation axis that is comparable to the mixed layer depth, which is the integral scale for the OPBL (Figure 1.1).

Rotation stress is the work done on these eddies by the Coriolis forces. In the Reynolds stress equations, the terms which represent the northward component of the Coriolis force are:

$$\frac{\partial u}{\partial t} = 2\Omega_y w + \dots ,$$

$$\frac{\partial w}{\partial t} = -2\Omega_y u + \dots .$$

These terms represent inertial motion in the  $x-z$  plane that is completely analogous to the more familiar inertial motion in the  $x-y$  plane. For westerly winds ( $\partial u, \partial z > 0$ ), this inertial motion induces a positive, or clockwise (looking in the positive  $y$  direction or north), circulation or vorticity. Changes in vorticity are accompanied by changes in

size of the vortex (Tennekes and Lumley, 1972). The vertical scale of the roll vortex is reduced for westerly winds as the vorticity is increased. This reduces the vertical scale of mixing (Figure 1.1). For easterly winds ( $\partial u / \partial z < 0$ ), the inertial motion induces a negative circulation or vorticity. Thus, the vorticity is reduced and the vertical scale of the roll vortex, and hence the mixed layer depth, is increased. The vorticity, the distribution of TKE, the rate of mixed layer deepening and the equilibrium depth of the mixed layer may all be altered by rotation stress.

Do eddies, roll vortices or other coherent structures actually exist in the OPBL? There is evidence that regular, large-scale, coherent structures exist for many turbulent flows. Intermittent turbulent activity observed in the atmospheric boundary layer is suggestive of large-scale, vertically-coherent structures (Shaw and Businger, 1985). Various large-scale structures have been observed in laboratory flows (Cantwell, 1981). These include the Taylor-Goertler vortex which is a well-documented secondary circulation that is found in rotating laminar and turbulent flows (Johnston, 1972; Hunt and Joubert, 1979). Taylor-Goertler vortices are cross-stream roll vortices that result from the destabilizing effects of rotation on the mean flow. Langmuir circulations have been observed in the upper ocean (see review by Leibovich, 1983) and longitudinal roll vortices have been observed in the atmosphere (LeMone, 1973). It is possible that both types of Langmuir circulations are planetary boundary layer scale Taylor-Goertler vortices.

Although the existence of these large-scale, evanescent structures is becoming undeniable, it has not been demonstrated that explicitly simulating these structures improves model performance (Saffman, 1980). The models developed and used in this research belong to a class known as bulk or vertically-integrated models. Thus, the structure of the turbulence is not explicitly accounted for in these models. Models of this type take advantage of the geometric similarity of the upper ocean structure to simplify the mean momentum and the TKE equations. The similarity solution used in this study defines the upper ocean as a fully turbulent, and therefore well-mixed, layer of depth  $h$ . Thus the OPBL is homogeneous in mean velocity and density. This implies that the Reynolds stresses are constant or linear in  $z$  (see Chapter III). The layer is bounded above by a wind-wave zone of depth  $\delta_w < h$  and at the bottom by a very sharp density gradient (the entrainment zone) of depth  $\delta < h$ , (Figure 1.2). The similarity structure is essentially that of Nüiler (1975) and Garwood (1977).

### 3. The Closure Problem and Parameterizations

The equations, (1.1) - (1.3), for the TKE components in the OPBL are the equations for the second-order autocorrelations of the turbulent velocity components. These three equations contain 14 second- and third-order correlations that are unknown. These include the shearing Reynolds stresses ( $\overline{u_i u_j}$ ), the pressure-velocity correlations ( $\overline{p u_i}$ ), the vertical transports ( $\overline{w u_i^2}$  and  $\overline{w p}$ ), the buoyancy flux ( $\overline{b w}$ ) and the viscous dissipation terms (1.6). The inclusion of equations for these unknown correlations incorporates more unknown correlations of equal and higher order. This problem is inherent in the process of Reynolds decomposition and constitutes the turbulence closure problem (Tennekes and Lumley, 1972). The solution to this problem is to choose a particular set of equations and "parameterize" the unknown correlations in terms of known correlations of the same or lower order, mean variables and boundary conditions. These parameterizations are based on laboratory and field observations, dimensional analysis and physical intuition. The order of the correlations that are calculated explicitly, the number of equations that are solved and the parameterizations of the terms involving unknown correlations varies among models of planetary boundary layers (Wyngaard, 1982).

Some of the models for the OPBL will be reviewed in Chapter II. The models used in this research are bulk (vertically-integrated), second-order closure models as in Garwood (1977). The details of the particular closure method and parameterization schemes used in this dissertation will be discussed in Chapter III. However, three processes and their parameterizations that will be particularly significant for this research need to be introduced before the working hypotheses and tests of the hypotheses are discussed. These are the dissipation, pressure-rate of strain and rotation stress.

This research is concerned with the rotation stress terms (R.1 and R.2) that alter the ratio of vertical to horizontal TKE in (1.1) and (1.3). These terms affect the distribution of TKE between the east-west and vertical TKE components. The average vertical turbulent velocity is changed which affects the rate of mixed layer deepening by altering the convergence of TKE at the entrainment zone. The parameterization of these terms requires no assumptions beyond those of the similarity solution. Garwood *et al.* (1985a) derived a bulk model that included rotation stress for a non-entraining mixed layer. They showed that the equilibrium depth that is achieved for a surface wind stress,  $\overline{\tau}$  (1.4), and a positive downward surface buoyancy flux is



$$L_{\Omega} = \frac{C_1 L_0}{(1 + C_2 \Phi)} \quad (1.7)$$

where the Obukhov length scale,

$$L_0 = \frac{\bar{\tau}^{3/2}}{\rho \overline{bw}(0)} \quad (1.8)$$

is the equilibrium depth for a balance between the surface stress and surface buoyancy flux. The ratio ( $\Phi$ ) of the rotation stress to the surface buoyancy flux is

$$\Phi = \frac{\Omega_y \tau_x}{\rho \overline{bw}(0)} \quad (1.9)$$

The equilibrium depth,  $L_{\Omega}$ , reflects the vertical elongation or contraction of mixed layer vortices in the x-z plane by planetary rotation shown in Figure 1.1. Rotation stress effectively modulates the damping due to the surface buoyancy flux such that the equilibrium depth,  $L_{\Omega}$ , will be greater for easterly winds (westward surface stress) or less for westerly winds (eastward surface stress) than  $L_0$ , the Obukhov depth (Figure 1.3). We have found no physical solution for  $L_{\Omega}$  is possible for  $\Phi < -1/2$  because total buoyant damping can not exceed dissipation. As the minimum value of  $\Phi = -1/2$  is approached, more of the TKE is damped by surface buoyancy flux, and the equilibrium depth approaches the limit  $L_{\Omega} = 7L_0$ . For positive  $\Phi$ , westerly winds,  $L_{\Omega} < L_0$  due to the increased transfer of vertical to horizontal TKE by rotation stress. The increased horizontal TKE is dissipated, and the mixing is reduced. Figure 1.3 shows that  $L_{\Omega}(\Phi = 0.58)$  is half the value of  $L_{\Omega}(\Phi = 0)$ . Thus, for westerly winds rotation stress causes an enhanced dissipation of TKE and results in a reduced equilibrium depth.

Planetary rotation has previously been incorporated into a bulk model of turbulence in the OPBL through the dissipation time scale (Garwood, 1977). If the dissipation rate is governed by the rate at which energy is supplied by the large scale turbulence, then dimensional arguments yield  $\epsilon \sim \bar{\epsilon}^{3/2}/h$  (Tennekes and Lumley, 1972). This assumes that the time scale for the energy transfer is the "eddy turnover scale" ( $h/\sqrt{\bar{\epsilon}}$ ), where the mixed layer depth is an appropriate length scale for the large-scale flow. This parameterization has been shown to be inadequate for slab models of the OPBL, since it allows a too deep winter mixed layer in annual simulations (see reviews by Garwood, 1979, and Zilitinkevich *et al.*, 1979). Garwood (1977) argued that planetary rotation provides an additional time scale ( $1/f$ ) for dissipation. This becomes important for deep mixed layers for which  $1/f < h/\sqrt{\bar{\epsilon}}$ . The dissipation parameterization becomes  $\epsilon \sim \bar{\epsilon}(\sqrt{\bar{\epsilon}}h + f)$ . This enhancement to the dissipation

parameterization is a rather *ad hoc* method of incorporating planetary rotation into a mixed layer model. It is not clear what physical processes are responsible for the additional dissipation. For westerly winds, rotation stress reduces the vertical convergence of TKE into the entrainment zone. This reduces the rate of mixed layer deepening. Thus, rotation stress may reduce or eliminate the need for the planetary rotation "enhancement" to the dissipation for westerly wind regimes. Furthermore, rotation stress represents a specific physical mechanism rather than a time scale based on dimensional arguments. One aspect of this research will be to compare the effects of rotation stress in westerly wind regimes to the rotational dissipation enhancement of Garwood (1977).

The pressure-rate of strain ( $\Pi.1 - \Pi.3$ ) is the only process other than rotation stress that redistributes energy among the TKE components. These are the only terms that may directly counter or reduce the effects of rotation stress. The expression for the fluctuating pressure, which is the basis for parameterizations of the pressure-rate of strain, contains terms that are similar to the rotation stress terms (R.1 - R.4) in (1.1 - 1.3), but with opposite sign. These terms in the pressure-rate of strain parameterization may reduce the effects of the explicit rotation stress terms.

The parameterization of the pressure-rate of strain requires an understanding of both the fluctuating pressure and the gradient of the fluctuating velocity. As mentioned above, the fluctuating pressure can react to local and remote variations of the turbulent and mean flows. However, the exact effects of the various processes that contribute to the pressure fluctuations are not well documented by experiment nor are they well understood theoretically. Thus, parameterizing the pressure-rate of strain remains an active research area, although this problem has been apparent for more than 40 years. It is beyond the scope of this dissertation to address the problem of parameterizing the pressure-rate of strain in general. However, a realistic parameterization of the term is needed to complete the model. The specific parameterization of the pressure-rate of strain that is used for this research will be discussed in Chapter III.

The possibility that the pressure-rate of strain may tend to cancel the rotation stress will be addressed here. An expression for the fluctuating pressure can be obtained by taking the divergence of the fluctuating velocity equations and making use of the incompressibility assumption. This yields a Poisson equation for the pressure fluctuations (Chou, 1945):

$$\frac{\nabla^2 p}{\rho} = - \left( \overline{\frac{\partial u_i \partial u_j}{\partial x_j \partial x_i}} - \frac{\partial u_i \partial u_j}{\partial x_j \partial x_i} \right) - 2 \frac{\partial U_i \partial u_j}{\partial x_j \partial x_i} + \frac{\partial b}{\partial x_3} + 2 \varepsilon_{ijk} \Omega_j \frac{\partial u_k}{\partial x_i} .$$

The solution, given by Green's theorem, is the integral of the right hand side over the entire volume occupied by the flow and all surfaces surrounding the volume (Morse and Feshbach, 1953). Thus, the local pressure fluctuations are determined by events taking place throughout the entire flow and by distant boundary conditions. With  $\vec{r}_1$  as the current location and integrating over all  $\vec{r}_2$ , the pressure fluctuations at  $\vec{r}_1$  are

$$p(\vec{r}_1) = \frac{\rho}{4\pi} \int \left\{ \left( \overline{\frac{\partial u_i \partial u_j}{\partial x_j \partial x_i}} - \frac{\partial u_i \partial u_j}{\partial x_j \partial x_i} \right) \frac{dV(\vec{r}_2)}{|\vec{r}_1 - \vec{r}_2|} \right. \\ \left. + \frac{\rho}{4\pi} \int \left( 2 \frac{\partial u_i \partial U_j}{\partial x_j \partial x_i} + \frac{\partial b}{\partial x_3} + \varepsilon_{ijk} \Omega_j \frac{\partial u_k}{\partial x_i} \right) \frac{dV(\vec{r}_2)}{|\vec{r}_1 - \vec{r}_2|} \right. \quad (1.10)$$

+ surface integrals .

Since the integrations in (1.10) are with respect to  $\vec{r}_2$ , the pressure-rate of strain terms can be formed by multiplying (1.10) by  $\partial u(\vec{r}_1)/\partial x_i$ , which is brought into the integrals, and then ensemble-averaging the resulting terms. The surface integrals are usually neglected. The argument is that the influence of the boundaries is negligible because the distance to the boundaries is large compared to the correlation length scale for the pressure-rate of strain terms. This may be an inaccurate assumption for boundary layer flows since the correlation length for the large-scale eddies is always the same order of magnitude as their distance from the boundary. The problem can also be recast using the method of images to avoid the inclusion of the surface integrals (Launder *et al.*, 1975). However, it has not been clearly demonstrated that the contribution from the surface integrals would be significant. In this study the surface integrals will be neglected, the resulting expression is

$$\frac{p \partial u_i}{\rho \partial x_j} = \frac{1}{4\pi} \int \left\{ \left( \overline{\frac{\partial u_i \partial u_j}{\partial x_j \partial x_i}} \right) \frac{\partial u'_i}{\partial x_j} \right\} \frac{dV(\vec{r}_2)}{|\vec{r}_1 - \vec{r}_2|} \\ + \frac{1}{4\pi} \int \left\{ \left( 2 \frac{\partial U_i \partial u_j}{\partial x_j \partial x_i} \right) \frac{\partial u'_i}{\partial x_j} + \left( \frac{\partial b}{\partial x_3} \right) \frac{\partial u'_i}{\partial x_j} + \varepsilon_{ijk} \Omega_j \left( \overline{\frac{\partial u_k}{\partial x_i}} \right) \right\} \frac{dV(\vec{r}_2)}{|\vec{r}_1 - \vec{r}_2|} \quad (1.11)$$

where the primes represent the expressions evaluated at  $\vec{r}_2$  and the unprimed variables are evaluated at  $\vec{r}_1$ . The first integral on the right hand side ( $\pi^n$ ) represents the nonlinear turbulence-turbulence interactions. The remaining volume integral ( $\pi^r$ ) represents turbulence-mean flow interactions. Unfortunately, the integrals can not be solved in general. However, there exists a first-order approximation that is universally

accepted for the first integral. This nonlinear part of the pressure-rate of strain tends to reduce the anisotropy of the turbulence (Lumley, 1978). It is usually parameterized with some form of the return-to-isotropy model of Rotta (1951),

$$\pi^n \propto (\bar{\epsilon} - \overline{w^2})/\tau ,$$

where  $\tau$  is a characteristic time scale. Thus, the nonlinear portion of the pressure-rate of strain term is assumed to be proportional to the degree of anisotropy of the turbulence.

The  $\pi^f$  term represents pressure fluctuations due to buoyancy, mean shear and rotation, respectively. This "rapid" part is so named because these pressure fluctuations can respond on time scales that are independent of, and in principle much faster than, the time scales of the turbulent velocity. For example, consider an initially isotropic turbulent flow that is subjected to an intense distortion by the mean flow. One possibility is an intense velocity shear (Lumley, 1972). For some time after the distortion, the turbulence is nearly isotropic so  $\pi^n$  is small and the turbulence responds to only the mean flow for some short time. The duration of this period is determined by the intensity of the distortion, so it depends only on the mean flow. Hence, the turbulence-mean flow terms are known as the "rapid" part of the pressure-rate of strain. These terms have been neglected in most parameterizations of the pressure-rate of strain (Chapter II).

The rotation terms in  $\pi^f$  may tend to cancel the effects of the explicit rotation stress terms. For two-dimensional turbulence with the assumptions that the pressure-rate of strain correlation length scale is small compared to variations in the Coriolis force and compared to the length scale of the mean shear, it appears that these terms do cancel the rotation stress terms (Gutteling, 1981). However, for three-dimensional flows this does not appear to be the case (B. Gallagher and E. Gutteling, University of Hawaii, personal communication).

More compelling evidence comes from studies of the atmospheric planetary boundary layer. Zeman and Tennekes (1975) included a parameterization of the terms in  $\pi^f$  that involved the mean shear and the Coriolis forces in a model of the atmospheric surface (constant stress) layer. If the turbulence is only weakly inhomogeneous on scales comparable to the integral scale, the mean flow variables in  $\pi^f$  can be taken outside the integral. The resulting integral of the divergence of the two-point velocity correlations is a fourth rank tensor. However, it is commonly assumed to be proportional to the single point velocity correlations (Launder *et al.*,

1975), which are the Reynolds stresses. The rotation terms in the resulting pressure-rate of strain parameterization of Zeman and Tennekes (1975) are proportional to the explicit rotation stress terms. That is

$$\pi_{ii}^r = \gamma_1 2\varepsilon_{ijk} \Omega_j \overline{u_i u_k} .$$

Based on the results of seven different shear flow experiments (Table 1), Zeman and Tennekes (1975) concluded that  $\gamma_1$  was  $0.26 \pm 0.04$ . Results calculated from the atmospheric boundary layer experiments were the two lowest values. However, this may be the result of the difficulties in measuring an environmental flow versus a laboratory flow, rather than a systematic difference between the atmospheric boundary layer and other shear flows. These results indicate that the pressure-rate of strain rotation terms are smaller than the similar rotation stress terms that appear explicitly in (1.1 - 1.3). For the well-mixed layer, the terms are likely to be even smaller than they are in the surface layer where the fluctuating pressure is large due to the presence of the boundary. In this research,  $\pi^r$  is parameterized with terms expressed as small perturbations of the explicit terms (see Chapter III and Garwood *et al.*, 1985a and b).

TABLE 1  
NUMERICAL VALUES OF  $\gamma_1$  FROM ZEMAN AND TENNEKES (1975)

where  $\gamma_1$  is the coefficient of the rotation term  
in the rapid part of their pressure-rate of strain parameterization

Source	$\gamma_1$
Champagne <i>et al.</i> (1970); homogeneous shear flow in a wind tunnel.	0.3057
Klebanoff (1955); wind-tunnel boundary layer on a smooth surface.	0.2928
So and Mellor (1972); surface layer in wind tunnel, smooth wall.	0.2792
Hinze (1975); turbulent pipe flow.	0.2726
Comte-Bellot (1965); turbulent flow between parallel plates.	0.2644
Cramer (1967); atmospheric surface layer.	0.2235
Wyngaard <i>et al.</i> (1974); atmospheric surface layer, modified data.	0.2227

Moeng and Wyngaard (1986) used a large-eddy simulation model to simulate the pressure covariance that results from the integrals in (1.11) for a convective atmospheric surface layer. They showed that the pressure covariances due to rotation were significantly smaller than the  $\pi^n$  terms and the pressure covariances due to the buoyancy fluxes. Thus, pressure covariances induced by rotation in  $\pi^r$  are probably

small compared to the rotation stress terms and the other pressure covariances for the well-mixed layer.

As indicated above, there are several unresolved issues and active areas of research involving the pressure-rate of strain parameterization. However, it is beyond the scope of this research to advance the parameterization of the pressure-rate of strain. Therefore, a working hypothesis will be that the rotation terms in the pressure-rate of strain parameterization are not as significant as the explicit rotation stress terms. Thus, the pressure-rate of strain parameterization used for this research will depend only weakly on fluctuations due to mean quantities. There does exist the possibility that any effects of the rotation stress terms that occur in the numerical results in this research may be negated by competing terms in the pressure-rate of strain. On the other hand, if this research discovers no significant rotation effects, then pursuing the more complex problem of rotation effects in the pressure-rate of strain parameterization is pointless.

### C. HYPOTHESES

Several working hypotheses will be tested in this dissertation to establish the effects and the significance of rotation stress for mixed layer dynamics. Comparisons of the effects of rotation stress and the rotationally enhanced dissipation parameterization of Garwood (1977) on mixed layer dynamics are of interest since both terms represent the effects of rotation on the TKE budget. However, the two terms represent different physics and affect the TKE budget quite differently. Both terms alter the rate of mixed layer deepening and the equilibrium mixed layer depth. The rotation stress does so by altering the distribution of TKE between the horizontal and vertical components, and hence altering the vertical convergence of TKE to the entrainment zone. The dissipation enhancement reduces the total TKE available for mixing.

The first hypothesis is that the functional form of the entrainment rate will be significantly different for rotation stress than for rotationally enhanced dissipation. The dependence of isotropy of the TKE budget on rotation stress should also be different than it is for rotationally enhanced dissipation. Both of these effects result from the fact that rotation stress distributes TKE among the TKE components, whereas dissipation reduces the TKE isotropically. These hypotheses are tested using the nondimensional framework that was developed in Garwood (1977) and used to intercompare mixed layer models in Garwood (1979). Unlike simulations,

nondimensional comparisons are independent of any tuning of parameterization constants. They demonstrate the functional form of the models, rather than the ability to fit the models to a particular data set. However, while nondimensional representations clearly reveal the functional form of models, they do not indicate whether that functional form depicts the actual behavior of the processes being modeled or the interactions among the processes. To accomplish the latter, comparisons of model simulations and data sets are required. Therefore, the isotropy of the TKE budget and the deepening rate will also be examined using model simulations.

A second working hypothesis for this dissertation is that diurnal to synoptic scale shallowing and deepening events are altered substantially by rotation stress. Variations in wind direction may substantially change the equilibrium depth of the mixed layer, particularly in late winter and early spring when the mixed layer is deep and the surface wind stress and surface buoyant damping nearly balance. Both the frequency of occurrence and the vertical scale of these mixing events are affected by rotation stress. In Garwood *et al.* (1985a), we have shown that the equilibrium depth predicted by a model that includes rotation stress is given by (1.7). This equilibrium depth can vary substantially from the Obukhov depth for east-west surface wind stress (Figure 1.3). This should be most apparent at diurnal to synoptic time scales, which are comparable to  $\Omega_y^{-1}$ . Furthermore, it is argued here that the entrainment rate is altered by the rotation stress, which affects deepening events as well as shallowing events. While the greatest depth which could be attained during a deepening event is limited by the equilibrium depth, the actual depth that is achieved on diurnal to synoptic scales is frequently determined by the time scale of the atmospheric forcing. In those cases, the rate of deepening and the initial conditions, rather than the equilibrium depth, control the vertical scale of the mixing event.

A last hypothesis is that the change in the vertical convergence of TKE caused by rotation stress may reduce or eliminate the need for the *ad hoc* rotational enhancement to the dissipation of Garwood (1977) which is needed to prevent excessive mixed layer deepening for westerly wind regimes. If rotation stress can eliminate or significantly reduce the need for rotationally enhanced dissipation, regions of predominately easterly winds would not have a one-dimensional cyclical steady-state for mixed layer depth without a net downward heat flux, since rotation stress enhances mixing for easterly winds. However, a cyclical steady-state could also be achieved with

a three-dimensional balance of forces such as a mean horizontal advection or divergence.

The hypotheses will be tested by means of three different models of mixed layer dynamics. The purpose of this approach is to distinguish the effects of various processes rather than to obtain the best comparison with the data by the simulations. The latter would probably be better accomplished with a combined model that incorporated all the processes. However, because the interactions between the processes are nonlinear, separating the effects of various process in a combined model would be difficult at best.

The details of the three models (ZSTAR, HSTAR and RSTAR) are developed in Chapter III. The ZSTAR model is the Garwood (1977) model, which contains the rotational dissipation enhancement that enters the equations through the nondimensional variable  $Z_*$ . The HSTAR model is the model of Garwood (1977) excluding dissipation enhancement ( $Z_* = 0$ ). Thus, HSTAR contains neither the rotational enhancement to dissipation or the rotation stress. The RSTAR model is the HSTAR model with the addition of rotation stress, which will be represented in the nondimensional form by  $R_*$ .



## II. LITERATURE REVIEW

### A. BULK OCEAN MIXED LAYER MODELS

This brief review of mixed layer models will focus primarily on vertically-integrated or bulk models. The purposes are to place the ZSTAR and RSTAR models in historical perspective with respect to models of the same type and to review the development of dissipation parameterizations. Other types of models and closure schemes, as applied to the OPBL, will be mentioned only briefly, and models of the atmospheric boundary layer will not be reviewed at all. All the models being reviewed use the TKE equation or the component TKE equations and close the Reynolds equations at second order or lower. Equations for the shearing stresses are not used in these models. Although models such as the Level 3 and 4 models discussed in Mellor and Yamada (1974) do include equations for the shearing stresses, this has not improved model performance in general (Martin, 1985).

Kraus and Rooth (1961) showed that an equilibrium could be established by a balance of surface cooling (due to longwave, sensible and latent heat fluxes) and warming at depth due to the absorption of solar radiation. The equilibrium depth for this balance is the solar radiation compensation depth. Kraus and Turner (1967) incorporated the mechanical mixing due to wind stress and the damping due to a negative surface buoyancy flux (warming) and included a heat equation. The equilibrium depth for this model is the Obukhov length scale ( $L_o$ ), which is the ratio of the surface shear production of TKE to surface buoyancy flux (1.8). This scale depth was first introduced into ocean modeling by Kitaigorodsky (1960) using the atmospheric surface layer as an analogue. Geisler and Kraus (1969) included an equation for the mean momentum, in addition to the TKE and mean temperature equations, and solved the three equation model for a slab or well-mixed layer in which the mean properties were constant (Figure 1.2).

Miropolsky (1970) and Denman (1973) were the first to incorporate dissipation due to molecular viscosity as a significant part of the TKE budget. The rate of dissipation ( $\epsilon$ ) is assumed to depend on the total TKE ( $\bar{\epsilon}$ , which is twice the total TKE) at the integral scale ( $L_i$ ) such that

$$\epsilon \sim \bar{\epsilon}^{3/2} ,$$

as discussed in the introduction. Niiler (1975) added the loss of TKE from the mixed layer due to the downward radiation of internal waves. He also resolved a perceived conflict between turbulence models and the model of Pollard *et al.* (1973). The later considered entrainment due to dynamic instabilities of the mean current and used the mean kinetic energy rather than the TKE to model the energy balance and resulting mixing.

Alexander and Kim (1976) and Kim (1976) showed that an enhancement to the dissipation was required to correctly model shallow summertime mixed layers. They hypothesized a constant background dissipation, so their dissipation parameterization had the form

$$\epsilon \sim \bar{e}^3/2 + c_0 ,$$

where  $c_0$  is a constant. Gill and Turner (1976) showed that previous mixed layer models could not close the annual cycle of mixed layer depth due to excessive wintertime deepening. Elsberry *et al.* (1976) used a dissipation enhancement that increased exponentially with depth to improve simulations of the ocean's response to hurricanes.

As discussed in the introduction, Garwood (1977) included a Rossby number dependent enhancement term in the dissipation parameterization. He also demonstrated the importance of explicitly modeling the convergence of TKE into the entrainment zone. This required the calculation of  $w_{rms} = \sqrt{w^2}$ . Thus, separate TKE budgets must be calculated for the horizontal and vertical components, whereas previous bulk mixed layer models used only the total TKE budget. Processes that transfer energy among the TKE components become important in any model that includes a separation of the TKE components, as does Garwood (1977). In the introduction, the pressure-rate of strain and the rotation stress were shown to be such processes.

Garwood *et al.* (1985a) derived a bulk model that included rotation stress for a non-entraining mixed layer. We showed that the equilibrium mixed layer depth for that model is  $L_\Omega$  (1.7). In Garwood *et al.* (1985b), we computed the longitudinal variation of  $L_0$  and  $L_\Omega$  along the equator in the Pacific. The longitudinal dependence of  $L_0$  computed using climatological values for the surface heat fluxes and for the east-west surface stress is shown in Figure 2.1. The vertical bars represent the variation in  $L_0$  caused by varying the surface heat flux by  $\pm 3W m^{-2}$ . The open circles are estimates of the mixed layer depth from Lemasson and Piton (1968). The longitudinal

variation of  $L_{\Omega}$  (Figure 2.2) agrees with the estimates of mixed layer depth significantly better than does  $L_0$ . The increased depth in the western part of the basin is the result of the stronger easterly winds relative to those on the east side of the basin.

The current research extends the non-entraining, equatorial study of the climatological, equilibrium mixed layer by Garwood *et al.* (1985a, b) to the case of the time-dependent, mid latitude mixed layer. Deepening and shallowing of the mixed layer will be studied for diurnal to seasonal time scales in contrast to the previous climatological studies.

Vertically-integrated or bulk models are not the only type models used to simulate the mixed layer. A variety of models exist that use eddy viscosity techniques to close the turbulence equations using only properties of the mean field. Since these will not be reviewed here, the interested reader is referred to Businger (1982) for a general review of the equations and concepts of turbulence modeling in the atmospheric boundary layer and a discussion of eddy viscosity model theory. Another set of models do not use a similarity solution to assist in closing the equations. Rather, a set of turbulence equations is solved as functions of  $z$  using standard finite difference or finite element numerical techniques. Whereas the vertically-integrated models require values only at the surface and bottom of the mixed layer, these models require a set of depth-dependent parameterizations for the higher order moments. A set of models of this type has been developed from the work of Mellor and Yamada (1974). This model was first applied to the OPBL by Mellor and Durbin (1975). Other models in this class include Warn-Varnas and Piacsek (1979), Kundu (1980) and Klein and Coantic (1981). A general review of boundary layer modeling using eddy diffusivity closure, second-order closure and eddy resolving models is given by Wyngaard (1982).

In the next section, studies that deal with rotating turbulent flows will be reviewed. Some background on pressure-rate of strain parameterizations will be given in the last section.

## **B. STUDIES OF THE EFFECTS OF ROTATION ON TURBULENT FLOWS**

The effects of rotation have been largely neglected in geophysical boundary layer modeling. However, the study of rotation and of streamline curvature, which produces similar effects, has received considerable attention in the engineering literature. In this section, the pertinent experimental and theoretical work is reviewed. This review will show experimental evidence for the existence and influence of rotation processes,

particularly rotation stress. The streamline curvature effects in turbulent boundary layers that are equivalent to rotation will also be discussed. Finally, the similarity of engineering models to the model proposed in this dissertation will be discussed.

Two early works modified the Richardson number and mixing length to include the effects of rotation. Rotta (1967) derived a modified mixing length to account for the effects of centrifugal and Coriolis forces on TKE production. His modification was based on an analysis of the component TKE equations. He calculated the velocity distributions for a turbulent flow between a fixed cylinder and an inner concentric rotating cylinder. The calculated velocity distributions were similar to, but consistently less than, the experimental values of Taylor (1935) and Wallendorf (1935). Bradshaw (1969) extended an analogy, first proposed by Prantl (1930), between the effects of gravity and the effects of centripetal or Coriolis acceleration. Using Prantl's analogy, Bradshaw constructed Richardson numbers for rotation and curvature that are analogous to the flux and gradient Richardson numbers for buoyancy. Values for the wall shear stress and the displacement thickness and momentum thickness of the boundary layer calculated from the curvature Richardson number (centripetal acceleration) compared favorably with the results of Schubauer and Klebanoff (1951). However, the wall shear stress, the displacement thickness and momentum thickness of the boundary layer calculated with the rotation Richardson number (Coriolis acceleration) were consistently less than the experimental values of Halleen and Johnston (1967). Although these results show that a simple Richardson number model is not completely adequate, such a model does yield results for steady state cases that are consistent with observations. Garwood *et al.* (1985b) demonstrated that a length scale based on a Richardson number, which included the effects of rotation, appears to correctly predict the longitudinal variation of the climatological mixed layer depth in the equatorial Pacific (Figure 2.2). This augmented Richardson number is

$$Ri_g = \frac{h}{L_\Omega} = \frac{\overline{bw} + 2\Omega_y \overline{uw}}{\overline{uw} \partial U / \partial z}$$

where  $L_\Omega$  is the rotation length scale defined in (1.7). This Richardson number reduces to the buoyancy Richardson number for  $2\Omega_y \overline{uw} \rightarrow 0$  and to the rotation Richardson number for  $\overline{bw} \rightarrow 0$ . This Richardson number criterion is derived directly from the steady-state, second-order closure model of this dissertation for the case of zero entrainment. The rotation processes that transfers energy among the TKE components were explicit terms in the Garwood *et al.* (1985a) model. In Rotta (1967)

and Bradshaw (1969), the rotation processes were incorporated in the parameterization of shear production.

Johnston *et al.* (1972) reported the results of a series of experiments performed in a channel rotating about an axis perpendicular to the mean flow and parallel to the side walls (Figure 2.3). This configuration will produce rotation stress terms analogous to those generated in the OPBL. In the OPBL, east-west winds generate an east-west Reynolds stress in the presence of a northward rotation vector and a vertical shear in the east-west mean current ( $\partial U/\partial z$ ). In the experiments of Halleen and Johnston (1967) and Johnston *et al.* (1972), the side walls generate a cross-stream Reynolds stress and mean shear in the presence of a vertical rotation vector. A schematic of the flow (Figure 2.3) shows that there will be a stable and an unstable side to the channel, as determined by the direction of the vorticity generated by the wall shear relative to the rotational vorticity. When the vorticities are additive, the flow is stabilized by the rotation, and the wall stress is reduced. When the vorticities subtract, the flow is destabilized by the rotation, which increases the wall stress. The results of these experiments showed qualitatively three rotation-related phenomena. The first was a change in the wall-layer streak bursting rate. The wall-layer streak bursting is due to the production of turbulence at the wall by dynamic pressure fluctuations in the inner, or constant stress, layer. It is directly related to the intensity of the turbulence in the outer, or well-mixed layer. The streak bursting rate is increased on the destabilized side of the channel and decreased on the stabilized side. The second effect was the suppression of the transition to turbulence on the stabilized side of the channel. The third effect was the formation and growth of longitudinal roll cells (Taylor-Goertler vortices) on the unstable side. The results quantitatively showed that the mixing length proposed by Bradshaw (1969) provided a good fit to the data for  $0 \leq Ri \leq 0.25$ . Miles (1961) showed that laminar flows were dynamically stable for  $Ri > 0.25$ . Qualitative results from another set of experiments conducted with the same apparatus (Johnston, 1973) indicated that for small Rossby numbers (rotation-dominated flows) the transition to turbulence occurred at Reynolds numbers an order of magnitude larger than those for no rotation. Thus, a stabilizing rotation stress has been shown to significantly suppress the transition to turbulence. However, Johnston (1973) also found that the criterion for transition to turbulence given by Bradshaw (1969) was inadequate. Thus, the Richardson number model of Bradshaw does not account for all rotation-related turbulence phenomena.

The literature on streamline curvature is somewhat more extensive than for rotation, probably due to the relative ease of experimental design. Because the effects of streamline curvature and rotation are analogous mathematically (Rotta, 1967, and Bradshaw, 1969), some experimental and theoretical work on streamline curvature will be included in this review. For streamline curvature, centripetal acceleration replaces the Coriolis acceleration of the rotation case. The interaction term becomes the centripetal acceleration multiplied by the Reynolds stress.

$$\text{downstream} \quad : \quad \frac{1}{2} \frac{\partial \overline{u^2}}{\partial t} = +2\overline{uw} \frac{U}{R} + \dots$$

$$\text{normal to wall:} \quad \frac{1}{2} \frac{\partial \overline{w^2}}{\partial t} = -2\overline{uw} \frac{U}{R} + \dots$$

(see, Rotta, 1967). The sign of the radius of curvature ( $R$ ) determines the direction of transfer of TKE. For convex curvature ( $R > 0$ ), the transfer is from the component normal to the wall to the downstream component, which stabilizes the flow. Conversely, concave curvature ( $R < 0$ ) destabilizes the flow by transferring TKE to the component normal to the wall (Figure 2.4).

So and Mellor (1973) showed that values for the critical curvature Richardson number for a curved two-dimensional boundary layer ranged from 0.30 near the start of the curved test section to 0.23 well inside the test section. These values are similar to the critical buoyancy Richardson number of 0.2 measured by Businger *et al.* (1971) in the atmosphere and to the theoretical value of 0.25 (Miles, 1961). Mellor (1975), using the Mellor and Yamada (1974) level 2 model, calculated a critical flux Richardson number of 0.21 and critical gradient Richardson number of 0.22 for buoyancy stabilized flows and a critical flux Richardson number of 0.19 for the curvature case. This is in good agreement with experimental results for the density stratified case, but underestimates the importance of the curvature. Mellor (1975) hypothesizes that the lack of turbulent diffusion (transport) in the level 2 model may account for the discrepancy. The Garwood (1977) model explicitly includes turbulent transport through the vertical convergence of TKE in the entrainment zone.

Irwin and Smith (1975) used a modification of the second-order closure model of Launder *et al.* (1975) to simulate the curvature stress effects found in the experiments of Gillis *et al.* (1965), Schubauer (1951) and Meroney and Bradshaw (1975). In that model, the curvature stress was parameterized as an extra production term (the "extra

rate of strain" concept of Bradshaw, 1973). Hunt and Joubert (1979) used a second-order closure model that explicitly accounted for the "conservative reorientation" of, or the transfer of TKE between, the TKE components by the curvature stress to explain the results of their experiments with "small" streamline curvature (large R). Here, small streamline curvature implies that the curvature does not significantly affect the mean flow. Gibson *et al.* (1981) simulated the response of a flow to large curvature. They used a second-order closure model with the unsteady terms parameterized in terms of transport by the mean flow, and the pressure-rate of strain parameterization included approximations for "rapid" distortion effects (rapid distortion will be discussed in the next section). The model was able to simulate the results of Gillis and Johnston (1979) for the curved region, but not for the region of recovery to a flat boundary layer.

Muck *et al.* (1985) studied the response of a fully developed turbulent flow to a sudden convex curvature. In a companion paper, Hoffman *et al.* (1985) studied the response of a fully developed turbulent flow to a sudden concave curvature. They concluded that the turbulent responses to convex and concave curvature were fundamentally different despite the similarity of the dimensional analysis for the two cases. Their argument is based on the difference in the structure of the turbulence. For concave curvature, the centripetal acceleration destabilizes the flow and Taylor-Goertler vortices are formed, as in the rotation experiments of Johnston *et al.* (1972). For convex curvature, the centripetal acceleration stabilizes the flow and the turbulence is damped, but its structure is virtually unaffected. This is analogous to the problem of stable versus unstable buoyancy regimes. Businger *et al.* (1971) empirically determined a stability correction to the mixing length in the atmospheric surface layer. They found that the form of the stability correction as a function of nondimensional height was different for stable versus unstable surface boundary layers. The significant variations in the structure of the turbulence between stable and unstable regimes and the effects of these structural changes deserves future study. For this research, the flow structure will be assumed to be similar in both the unstable and stable regimes, whether due to rotation or buoyancy. This assumes that the flow is dominated by the shear, so that the structural differences in the turbulence associated with the unstable and stable regimes are not significant.

The rotation stress, or the equivalent streamline curvature effect, does not affect every rotating, or curved, turbulent flow. The rotation stress can be written in a generalized form as

$$\varepsilon_{ijk} 2\Omega_i \overline{u_j u_k} ,$$

where  $\varepsilon_{ijk} = 0$  if any two indices are repeated (Garwood *et al.*, 1987). Fernando (1987) mentioned several experiments for which the rotation stress is zero because the rotation axis is not orthogonal to the Reynolds stress (i.e., two indices repeated in the above expression). There must be a component of the Reynolds stress in the plane perpendicular to the axis of rotation for a nonzero rotation stress. Conversely, rotation stress is not the only mechanism by which rotation affects turbulent flows. Other mechanisms such as inertial waves and centripetal acceleration can also play significant roles.

Ibbetson and Tritton (1975) found that the decay rate of grid-stirred turbulence in a rotating tank increased with increasing rotation rate. Also, the ratio of the parallel to the perpendicular turbulence length scales relative to the rotation axis increased with increasing rotation rate. However, the ratio of turbulent intensities in the two directions remained essentially constant. In this experiment, the turbulence was generated by oscillating a grid parallel to the rotation axis. No rotation stress was produced since there was no stress perpendicular to the rotation axis. In this case, the increased decay rate is probably due to the generation of inertial waves and the change in length scales is probably the result of centripetal accelerations.

Hopfinger *et al.* (1982) used a grid oscillating parallel to the axis of rotation in a rotating tank to study the transition from three-dimensional turbulence near the grid to two-dimensional turbulence away from the grid. Again, the rotation stress is zero. Away from the grid, the scale of the turbulence increases and the turbulent intensity decreases, so that the rotation effect becomes increasingly important. For the Rossby number  $\sim 0.2$ , the flow breaks down into a two-dimensional field of vortices aligned with the rotation axis and remains in this configuration with increasing distance from the grid. This pattern is consistent with the results of Ibbetson and Tritton (1975) regarding the change in length scale with time. A similar set of experiments by Dickinson and Long (1983) gave similar results. Maxworthy (1986) used the apparatus of Hopfinger *et al.* (1982) to show that the entrainment rate across a density interface decreases with decreasing Rossby number (increasing rotation rate). Based on the entrainment model of Linden (1973), which did not consider the effects of rotation, Maxworthy tentatively concluded that the change in entrainment rate with rotation was due to the loss of TKE to inertial oscillations induced in the mixed layer. Again, no rotation stress was generated with the configuration used in this apparatus.



In summary, the experimental evidence shows significant effects due to rotation stress and to curvature stress. The attempts to simulate these processes numerically indicate that a second-order closure model that explicitly accounts for the conversion of TKE among components is necessary to model the phenomenon of rotation stress. However, the appropriate augmented Richardson number can give approximate results for the steady-state case.

### C. PRESSURE-RATE OF STRAIN PARAMETERIZATIONS

As discussed in the introduction, it is possible that rotation effects in the pressure-rate of strain parameterization may counteract the explicit rotation stress. However, the exact effects of the various processes that contribute to the pressure fluctuations are not well documented by experiment nor are they well understood theoretically. Thus, parameterizing the pressure-rate of strain is difficult and controversial. This review will focus on some aspects of the parameterization of the the rapid part of the pressure-rate of strain ( $\pi^r$ ).

Parameterizations for  $\pi^r$  can largely be divided into two categories: the first assumes a specific structure for the turbulence; the second assumes that the integral can be expressed as a series expansion about an isotropic TKE distribution (Wyngaard, 1982). The difficulty with the former is that the parameterization can only be valid for geometrically similar flows, and the geometries chosen must be fairly simple or the integral is still not solvable. The difficulty with the second is that important processes that these terms are supposed to represent (e.g., rapid distortions) are not a perturbation on an isotropic state. Both methods neglect the surface integrals in the general expression for  $p$ . Thus, they ignore wall effects that are fundamental to boundary layer flows. Some investigators (Gibson and Launder, 1978) have included boundary effects in a parameterization of the pressure-rate of strain, but the results do not seem to constitute a measurable improvement (Wyngaard, 1980).

Donaldson (1972) discussed a set of theoretical criteria for the parameterization of second and higher order terms in the Reynolds averaged equations. To satisfy these constraints, the parameterization must preserve the tensor character and symmetry properties of the original terms, be dimensionally correct, be invariant under Galilean transformations and must satisfy the conservation laws that were satisfied by the original terms. The fact that no parameterization of the pressure-rate of strain has yet been proposed that can meet all the theoretical constraints, and not be so cumbersome as to be unusable, points out the difficulties of parameterizing the pressure-rate of

strain. Schumann (1977) further noted the importance of realizability for turbulence parameterizations. Realizability requires that the parameterization to produce only values that can be realized in actual flows. That is, the model should not be able to generate negative TKE, negative TKE components, negative dissipation or covariances greater than one (Lumley, 1978). Lumley (1979) attempted to construct a model that met these requirements, but the resulting expressions were too cumbersome to be of practical use (Wyngaard, 1982).

The parameterization of the pressure-rate of strain, particularly the rapid part of the term, has remained a major problem in turbulence closure (see reviews by Reynolds, 1976, Lumley, 1979 and Zeman, 1981). Recent work has attempted to obtain more universal and fundamental expressions for the pressure-rate of strain by limiting the number and type of assumptions used in the parameterization. As discussed in Chapter I, the integral of the two-point correlations of the velocity derivatives that results from the expression for the rapid part of pressure-rate of strain (1.11) is a fourth rank tensor. Gallagher *et al.* (1981) started with a general expression for this fourth rank tensor, which is the sum of 81 terms each with a scalar coefficient, and by rigorous arguments reduced the number of unknown coefficients from 81 to 6. The six remaining coefficients required assumptions regarding the nature of the particular flow. Morris (1984) obtained a general form for the pressure-rate of strain parameterization that was similar to that of Launder *et al.* (1975) without requiring that the turbulence be homogeneous. This research is not intended to obtain a general solution to the pressure-rate of strain closure problem. However, the possible effects of the pressure-rate of strain on the TKE budget and on the rotation stress terms must be recognized.

In summary, this review has shown that most models of geophysical mixed layers have been constructed in such a way that rotation processes are neglected. Models that do allow for rotation effects have been developed for other flow applications and have improved predictive capability for rotating boundary layers with respect to models that neglect rotation. Also, there is a substantial body of evidence from the engineering literature that rotation plays an important role in turbulent boundary layers that are dynamically similar to the OPBL. Thus, there is reason to expect that including rotation stress in a model of the OPBL should improve the predictive capability of the model. Furthermore, the investigation of a more complete and sophisticated picture of the OPBL is worthwhile on its own merits.

### III. THEORY

#### A. MODEL DEVELOPMENT

The model developed in this research assumes vertical homogeneity for the mean, dynamical variables for  $-h \leq z \leq -\delta_w$ . The well-mixed profile, discussed in Chapter I (Figure 1.2), is consistent with the average state of the upper ocean. The value of  $h$  is assumed to correspond closely to the mixed layer depth, and "mixed layer" here is synonymous with turbulent boundary layer. However,  $h$  is formally the depth of the maximum vertical penetration of TKE and turbulent fluxes generated in response to the wind stress,

$$\vec{\tau} = \tau_x \hat{e}_x + \tau_y \hat{e}_y = -\rho \overline{uw}(0) \hat{e}_x - \rho \overline{vw}(0) \hat{e}_y, \quad (3.1)$$

and the surface buoyancy flux,  $bw(0)$ .

The model described in this chapter is for a time-dependent mixed layer that may deepen or retreat in response to the surface fluxes. The mixed layer deepens in response to increased TKE production by wind stress or surface cooling (positive surface buoyancy flux) when water is entrained into the fully turbulent OPBL from the pycnocline below. When the mixed layer retreats, a new shallower mixed layer forms. The portion of the water column that had been part of the mixed layer now contains water of almost homogeneous properties, but the flow is no longer actively turbulent. The following discussion parallels section 2 of Garwood *et al.* (1985a), who discussed the equilibrium or time-independent simplification of the more general theory developed in this research.

Integrating (1.1), (1.2) and (1.3) through the mixed layer yields:

$$\frac{\partial \langle \overline{u^2} \rangle}{\partial t} dz = 0 = G_x + \Pi_{xx} + \Omega_z h \langle \overline{uv} \rangle + \Omega_y h \langle \overline{uw} \rangle - D/3, \quad (3.2)$$

$$\frac{\partial \langle \overline{v^2} \rangle}{\partial t} dz = 0 = G_y + \Pi_{yy} - \Omega_z h \langle \overline{uv} \rangle - D/3, \quad (3.3)$$

$$\frac{\partial \langle \overline{w^2} \rangle}{\partial t} dz = 0 = \langle \overline{bw} \rangle + \Pi_{zz} - \Omega_y h \langle \overline{uw} \rangle - D/3, \quad (3.4)$$

where

$$\langle \quad \rangle = \int_{-h}^0 dz \quad .$$

These equations are derived assuming local isotropy at the Kolmogorov length scale, linear flux profiles, and one dimensionality for the TKE budget (a good approximation even if the density and momentum fields are not horizontally homogeneous, see Chapter I). We assume a steady-state TKE budget and set the left hand side of (3.2)-(3.4) to zero since, as discussed previously, the unsteady terms are important only on very short time scales (less than 100 seconds). The integral through the OPBL of the shear production plus the production due to breaking surface waves minus the loss due to the downward radiation of internal waves (terms G.1 - G.3 and P.4 in 1.1 - 1.3) is G. The vertically-integrated pressure-rate of strain is  $\Pi$ , ( $\Pi.1 - \Pi.3$  in 1.1 - 1.3). The viscous dissipation rate ( $\epsilon$ ) in (1.1 - 1.3) integrated through the mixed layer is D. The terms (R.1 - R.4 in 1.1 - 1.3), namely

$$- \epsilon_{ijk} \Omega_j \langle \overline{u_i u_k} \rangle h \quad ,$$

are the rotation stresses (the interaction of rotation of the earth with the Reynolds shear stresses). The sign of  $\langle \overline{uw} \rangle$  is such that rotation stress increases  $\overline{u^2}$  in (3.2) if  $\langle \overline{uw} \rangle$  is positive. The planetary rotation vector is

$$\Omega = \Omega_y \hat{e}_y + \Omega_z \hat{e}_z$$

where  $|\Omega| = 7.29 \times 10^{-5} \text{sec}^{-1}$ . For the mean horizontal momentum to be independent of depth, the vertical turbulent momentum fluxes ( $\overline{uw}$  and  $\overline{vw}$ ) in the mixed layer must be linearly dependent on z or constant. If the depth dependence is assumed to be linear, the vertically integrated momentum fluxes (the Reynolds shear stresses) are

$$\langle \overline{uw} \rangle = \frac{h}{2} (\overline{uw}(-h) - \overline{uw}(0)) \quad ,$$

$$\langle \overline{vw} \rangle = \frac{h}{2} (\overline{vw}(-h) - \overline{vw}(0)) \quad ,$$

where  $\overline{uw}(0)$  and  $\overline{vw}(0)$  are defined in (3.1). The fluxes at the base of the mixed layer are given by the "jump conditions"

$$\overline{uw}(-h) = - \frac{\Delta U dh}{dt} \quad , \quad \text{and}$$

$$\overline{vw}(-h) = - \frac{\Delta V dh}{dt} \quad ,$$

where

$$\Delta U = \langle U \rangle - U(-h-\delta)$$

and

$$\Delta V = \langle V \rangle - V(-h-\delta)$$

are the mean velocity change through the entrainment zone (see Niiler, 1975).

The focus of this study is on the exchange of energy between  $\overline{u^2}$  and  $\overline{w^2}$  by the action of the east-west wind stress ( $\tau_x = -\overline{uw}(0)$ ) in the presence of the northward component of planetary rotation ( $\Omega_y$ ). This term will reduce vertical mixing if the winds are westerly ( $\tau_x > 0$ ), and it will increase vertical mixing if the winds are easterly ( $\tau_x < 0$ ).

The total shear production plus the production of TKE by breaking surface waves minus the loss at  $z = -h$  due to the downward radiation of internal waves integrated over the mixed layer is

$$- \left[ \overline{uw} \frac{\partial U}{\partial z} + \overline{vw} \frac{\partial V}{\partial z} + \frac{\partial}{\partial z} \left( \frac{\overline{wp}}{\rho} + \frac{\overline{we}}{2} \right) \right] dz = G_x + G_y = G.$$

The parameterization for  $G$  is

$$G = m_3 \frac{|\overline{\tau}|^{3/2}}{\rho} + \frac{[(\Delta U)^2 + (\Delta V)^2] \partial h}{2 \partial t},$$

where  $m_3$  and the subsequent  $m_1$ ,  $m_2$ ,  $m_4$  and  $m_5$  are dimensionless tuning coefficients. These coefficients are assumed to be reasonably constant for the upper-ocean boundary layer under a wide variety of atmospheric forcing conditions. The production of TKE by the shear of the mean current will be neglected in this study. This may not be a good assumption when  $h$  is small or in regions of strong surface currents. Martin (1985) speculates that mixed layer simulations of the shallow summertime mixed layer might be improved by the inclusion of TKE production by the mean shear in the entrainment zone. However, deSzoeko and Rhines (1975) and Garwood and Yun (1979) demonstrate that wind shear production of TKE is the more important source of energy for deepening the mixed layer in general. Therefore, TKE production by the shear of the mean current will be neglected for this study, which is primarily concerned with late winter and early spring cases for which the mixed layer is deep. The ratio of the integral of the rotation stress associated with the mean shear through the mixed layer to that of the production of TKE by the mean shear,

$$\frac{\Omega_y h \Delta U \frac{dh}{dt}}{\frac{[(\Delta U)^2 + (\Delta V)^2] dh}{2 dt}} \sim \frac{2\Omega_y h}{\Delta U}$$

is only  $O(10^{-2})$  even for a  $1 \text{ m s}^{-1}$  shear in the mean current and a 100 m deep mixed layer. Therefore, the rotation stress associated with the mean shear will also be neglected.

For the mean buoyancy to be independent of depth, the buoyancy flux in the mixed layer must be linearly dependent on  $z$  or constant. The vertically integrated buoyancy flux is

$$\langle \overline{bw} \rangle = \frac{h}{2} (\overline{bw}(-h) - u_* b_*)$$

The effective buoyancy flux through the surface ( $u_* b_*$ ) is the net downward surface buoyancy flux due to the sensible and latent heat fluxes and longwave radiation plus the buoyancy flux due to the absorption of solar radiation ( $Q_s$ ) as a function of  $z$ :

$$u_* b_* = -\overline{bw}(0) - \frac{\alpha g}{\rho c_p} \int_{-h-\delta}^0 |Q_s| - \frac{2}{h+\delta} \int_{\frac{z}{2}}^0 Q_s d\zeta dz$$

The absorption of solar radiation with depth significantly affects mixed layer dynamics, particularly for shallow summertime mixed layers (Martin, 1985; Simpson and Dickey, 1981). The flux of buoyancy through the base of the mixed layer is due to the entrainment of the more dense, underlying water. This entrainment buoyancy flux is

$$\overline{bw}(-h) = - \frac{\Delta B h}{dt}$$

where  $\Delta B = \langle B \rangle - B(-h-\delta)$  is the mean buoyancy change through the entrainment zone.

The total dissipation,

$$\int_{-h-\delta}^0 \epsilon dz = D$$

is a function of the vertical average of the turbulent kinetic energy,

$$D = m_1 \langle \overline{u_i u_i} \rangle^{3/2}$$

where  $\overline{u_i u_i} = \overline{u^2 + v^2 + w^2}$  (i.e., the normal summation convention on repeated indices is implied). Although the large-scale turbulence is anisotropic, the production and dissipation scales are assumed to be sufficiently well separated (i.e., large Reynolds number) so that the turbulence is isotropic at the dissipation (or Kolmogorov) scale.

This implies that the dissipation should be partitioned equally among the normal Reynolds stress components. For the ZSTAR model, the dissipation parameterization is

$$D_g = m_1 (\langle \overline{u_i u_i} \rangle^{1/2} + \frac{m_5}{m_1} fh) \langle \overline{u_i u_i} \rangle \quad (3.5)$$

where the additional term is the rotational dissipation enhancement. By definition, the rotation stress is neglected in the ZSTAR model.

The extent of vertical mixing depends upon the rate of conversion of horizontal turbulent kinetic energy ( $\langle \overline{u^2 + v^2} \rangle$ ) to vertical turbulent kinetic energy ( $\langle \overline{w^2} \rangle$ ). As discussed in Chapter I, there are two processes that may accomplish this. The first process is the pressure-rate of strain given by

$$\Pi_{\alpha\alpha} = \frac{\overline{u_\alpha \partial p}}{\rho \partial x_\alpha}$$

with no summation implied on repeated indices. The second process is the rotation stress,

$$-\varepsilon_{ijk} \Omega_j \tau_k h / \rho \quad .$$

The pressure-strain rate correlation ( $\Pi_{\alpha\alpha}$ ) can generally be divided into two parts: the nonlinear self-interaction of the turbulent field ( $\Pi^N_{\alpha\alpha}$ ) and the "rapid" terms resulting from the interaction of the turbulence and the mean field ( $\Pi^R_{\alpha\alpha}$ ), as discussed in Chapter II. The  $\Pi^N_{\alpha\alpha}$  terms cause a reduction in the anisotropy of the integral scale turbulence and are conventionally parameterized using the return-to-isotropy model of Rotta (1951). A version of this parameterization, which is consistent with our assumptions, is

$$\Pi^N_{\alpha\alpha} = m_2 \langle \overline{u_i u_i} \rangle^{1/2} (\langle \overline{u_i u_i} \rangle - 3 \langle \overline{u_\alpha^2} \rangle).$$

The "rapid" terms were discussed at length in Chapters I and II. As discussed in Chapter II, this research is not intended to obtain a general solution to the pressure-rate of strain closure problem. Rather, a simple approximation for  $\Pi^R_{\alpha\alpha}$  will be used and this study will focus on the impact of the explicit rotation stress term. The approximation that will be used for  $\Pi^R_{\alpha\alpha}$  has been used effectively to model a variety of turbulent flows that do not depend strongly on "rapid" distortion effects.

Expressions for  $\Pi^R_{\alpha\alpha}$  can be defined in terms of the vertically integrated variables discussed above. A set of such parameterizations is:

$$\Pi^R_{xx} = -a_1 G_x - a_2 \Omega_z h \langle \overline{uv} \rangle + a_3 \Omega_y \langle \overline{uw} \rangle \quad ,$$

$$\Pi_{yy}^R = - a_4 G_y - a_2 \Omega_z h \langle \overline{uv} \rangle ,$$

and

$$\Pi_{zz}^R = - a_5 \langle \overline{bw} \rangle - a_3 \Omega_y \langle \overline{uw} \rangle .$$

These are consistent with the work of Zeman and Tennekes (1975), which was discussed in Chapter I. Thus, the rapid part of the pressure terms can be incorporated into the other turbulence-mean flow terms. The literature review in Chapter II indicated the uncertain state of knowledge of the magnitude and effects of these terms in general. In particular, there is a lack of experimental evidence concerning the magnitudes and effects of the  $\Pi_{\alpha\alpha}^R$  on geophysical turbulent boundary layers. In view of this situation, we will assume that the  $a_i < 1$  for all  $i$ . This is consistent with Zeman and Tennekes (1975), who estimated that these rotation terms were small ( $a_2 = 0.26 \pm 0.04$ ) for the atmospheric surface layer (See Chapter I). This is also consistent with the results of Zeman and Lumley (1976) and Moeng and Wyngaard (1986). Also, Wyngaard *et al.* (1974) evaluated the effect of the explicit Coriolis terms on the structure of the Reynolds stress profiles for a buoyancy driven atmospheric planetary boundary layer and concluded that there was no significant change in the structure of the profiles. The present study concerns the stress-driven ocean planetary boundary layer. However, the assumption that the Reynolds stress profiles are linear in  $z$  is consistent with these results of Wyngaard *et al.* (1974).

## B. NONDIMENSIONAL EQUATIONS

The TKE equations can be written in nondimensional form to intercompare various models and model terms. Normalizing the terms in (3.2 - 3.4) with the surface shear production yields the nondimensional variables given in Table 2. The RSTAR model developed in this research includes rotation stress and neglects dissipation enhancement. The nondimensional equations are shown in Table 3. The dependent variables are:  $P_*$ , the nondimensional entrainment rate;  $E_*$ , the nondimensional total TKE; and  $W_*^2$ , the vertical component of the TKE. The independent variables are the nondimensional mixed layer stability ( $H_*$ ) and the nondimensional surface rotation stress ( $R_*$ ). Equations (3.7a) - (3.7c) form a nonlinear, coupled set of equations for  $E_*$ ,  $P_*$  and  $W_*^2$  as functions of  $H_*$  and  $R_*$ .

Two other models will be used for comparison. They are the ZSTAR model (Table 4) from Garwood (1977) and the HSTAR model (Table 5). The ZSTAR model contains a dissipation enhancement term ( $Z_*$ ), which depends on rotation but does not contain rotation stress ( $R_*$ ). Garwood (1977) demonstrated that the dependence of  $P_*$



TABLE 2  
THE NONDIMENSIONAL VARIABLES

$$P_* = \frac{h\Delta B}{2m_3 u_*^3} \frac{dh}{dt}, \quad \frac{\text{entrainment buoyancy flux}}{\text{wind shear production}}; \quad (3.6a)$$

$$E_* = \left(\frac{m_1}{m_3}\right)^{2/3} \frac{\overline{e}}{u_*^2}, \quad \frac{\text{total TKE}}{\text{surface momentum flux}}; \quad (3.6b)$$

$$W_*^2 = \left(\frac{m_1}{m_3}\right)^{2/3} \frac{\overline{w^2}}{u_*^2}, \quad \frac{\text{vertical TKE}}{\text{surface momentum flux}}; \quad (3.6c)$$

$$Z_* = \frac{p_3 fh}{u_*}, \quad \frac{\text{mixed layer depth}}{\text{rotation length scale}}; \quad (3.6d)$$

$$H_* = \frac{-\overline{bw}(0)h}{2m_3 u_*^3}, \quad \frac{\text{surface buoyancy flux}}{\text{wind shear production}}; \quad (3.6e)$$

$$R_* = \frac{\Omega_y h r^x / \rho}{2m_3 u_*^3}, \quad \frac{\text{surface rotation stress}}{\text{wind shear production}}; \quad (3.6f)$$

where  $p_1 = m_4/m_1$ ,  $p_2 = m_2/m_1$ ,  $p_3 = m_5/m_1$

TABLE 3  
THE RSTAR MODEL:  $P_* = P_*(R_*, H_*)$

$$0 = 1 - \frac{2E_*^{3/2}}{3} - p_2 E_*^2 (E_* - 3W_*^2) + R_* , \quad (3.7a)$$

$$0 = -H_* - P_* - \frac{E_*^{3/2}}{3} + p_2 E_*^2 (E_* - 3W_*^2) - R_* , \quad (3.7b)$$

$$0 = -P_* + \frac{p_1 W_* E_*}{2} . \quad (3.7c)$$

TABLE 4  
THE ZSTAR MODEL:  $P_* = P_*(Z_*, H_*)$

$$0 = 1 - \frac{2E_*^{3/2}}{3} (E_* + Z_*) - p_2 E_*^2 (E_* - 3W_*^2) , \quad (3.8a)$$

$$0 = -H_* - P_* - \frac{E_*^{3/2}}{3} (E_* + Z_*) + p_2 E_*^2 (E_* - 3W_*^2) , \quad (3.8b)$$

$$0 = -P_* + \frac{p_1 W_* E_*}{2} . \quad (3.8c)$$

TABLE 5  
THE HSTAR MODEL:  $P_* = P_*(H_*)$

$$0 = 1 - \frac{2E_*^{3/2}}{3} - p_2 E_*^2 (E_* - 3W_*^2) , \quad (3.9a)$$

$$0 = -H_* - P_* - \frac{E_*^{3/2}}{3} + p_2 E_*^2 (E_* - 3W_*^2) , \quad (3.9b)$$

$$0 = -P_* + \frac{p_1 W_* E_*}{2} . \quad (3.9c)$$

on  $Z_*$  prevented excessive mixed layer deepening at the end of the winter cooling season. This allowed a cyclical steady-state solution to the model without requiring

either a negative net buoyancy flux or advection. However, the physical basis for this enhanced dissipation is unclear, and  $Z_*$  may represent physical processes that are not actually due to the dissipation. These effects may include upwelling due to large-scale horizontal divergence, loss of TKE in the mixed layer due to internal waves (Muller *et al.*, 1984), inertial oscillations and rotation stress.

The variables in (3.8a) - (3.8c) from Table 4 are the same as in (3.7a) - (3.7c), except with the addition of rotationally enhanced dissipation  $Z_*$ , defined by (3.6d), which is the inverse of a boundary layer Rossby number and the elimination of the rotation stress  $R_*$ . The dissipation in the ZSTAR model is

$$D = E_*(E_*^{1/2} + Z_*) ,$$

which is the nondimensional equivalent of the enhanced dissipation (3.5). In both the ZSTAR model and the RSTAR model, the dissipation is distributed equally among the three TKE components. The term  $E_*Z_*$  imposes an additional length scale ( $f'u_*$ ) that affects  $h$ . The equilibrium mixed layer depth is now a function of a boundary layer Richardson number and a boundary layer Rossby number. Expressed in terms of length scales, this yields  $h = G(L_o, \sqrt{u_*}/f)$ . This is similar to the equilibrium depth scale for rotation stress (1.7) that was introduced in Chapter I.

For  $Z_* = R_* = 0$ , the two models RSTAR and ZSTAR are identical. The resulting model (HSTAR) depends on  $H_*$  (i.e. surface buoyancy flux) exactly as the RSTAR and ZSTAR models do (3.9b from Table 5). However, the HSTAR model does not include rotation stress or a dissipation enhancement. Thus, comparisons of the RSTAR and ZSTAR models with the HSTAR model allow the effects of the rotation stress and the dissipation enhancement respectively to be isolated.

The terms  $R_*$  and  $Z_*$  are the inverses of two boundary layer Rossby numbers, which represent the ratio of the shear production of TKE to the vertical and horizontal rotation stresses respectively. Although the mathematical forms of  $R_*$  and  $Z_*$  are similar, the processes impact the TKE budget in *fundamentally* different ways. The energy redistribution ( $R_*$ ) represents a known physical process that results from vortex stretching by the interaction of the Reynolds stresses and planetary rotation. It is a direct integration of the original terms that involves no higher order moments and requires no parameterization. Conversely,  $Z_*$  is *part* of a parameterization of the dissipation of turbulence by molecular viscosity. As discussed in Chapter II, the parameterization of dissipation in mixed layer models has become increasingly sophisticated. However, it has usually been assumed that TKE is dissipated

isotropically. As will be shown in the following sections, this assumption may be incorrect for dissipation in geophysical planetary boundary layers.

Since the independent variables  $R_*$  and  $Z_*$  enter the equations with different powers of  $E_*$ , the effects on the mixed layer ought to be dissimilar. In RSTAR compared to ZSTAR, the equations have been simplified by eliminating one of the highest order terms in  $E_*$ , namely  $E_*^{3/2}Z_*$ . The number of constants also is reduced by one, since  $p_3$  in the definition of  $Z_*$  is eliminated. At the same time, the number of physical degrees of freedom is increased since wind direction now affects the turbulent boundary layer dynamics. Mathematically, this means that  $R_*$  less than zero is allowed whereas  $Z_*$  less than zero is not. This will be discussed in more detail in the next section.

### C. IMPLICATIONS FOR THE ENERGY BUDGET

Most integral models of the OPBL are based on the total TKE equation. The models of Kraus and Turner (1967), Niiler (1975), Elsberry and Camp (1978) and Kim (1976) are examples. For these models, the rate of mixed layer deepening is determined completely by the boundary conditions on the mixed layer. However, Garwood (1977) demonstrated the importance of the convergence of TKE at  $z=-h$  for mixed layer deepening. Thus, both the horizontal ( $\overline{u^2 + v^2}$ ) and the vertical ( $\overline{w^2}$ ) TKE components must be known. As a result, the transfer of TKE between the horizontal and vertical components becomes important, and the sources and sinks of TKE must be considered in relation to the TKE component(s) they directly affect.

The block diagram of the TKE budget (Figure 3.1) is presented in terms of depth-averaged, dimensional variables that are defined in terms of their nondimensional counterparts in Table 6. The depth-averaged variables are independent of mixed layer depth, unlike the nondimensional variables. Thus, they are better suited for comparing models when the predicted mixed layer depths do not coincide. The wind stress production also becomes an explicit term. These characteristics will be particularly useful in Chapter IV where the block diagram will be used to discuss model simulations at OWS P and OWS N.

The TKE budget for the OPBL is shown in Figure 3.1. The terms in the first two equations in Table 3, 4 or 5 are represented by the arrows in the figure. The third equation in all three tables defines  $P_*$ . Therefore, no new processes are introduced into the TKE budget by the third equation. Wind mixing ( $G$ ) is a source of horizontal TKE. Surface cooling ( $H = u_* b_* < 0$ ) is the only source of vertical TKE. The sinks of

TABLE 6  
DIMENSIONAL, DEPTH-AVERAGED VARIABLES

Total TKE:  $E = E_* \frac{m_3 u_*^3}{h}$  (3.10a)

Vertical TKE:  $W^2 = W_*^2 \frac{m_3 u_*^3}{h}$  (3.10b)

Surface Buoyancy Flux:  $H = H_* \frac{m_3 u_*^3}{h}$  (3.10c)

Entrainment Rate:  $P = P_* \frac{m_3 u_*^3}{h}$  (3.10d)

Rotation Stress:  $R = R_* \frac{m_3 u_*^3}{h}$  (3.10e)

Pressure Redistribution:  $\Pi = p_2(E - 3W^2)$  (3.10f)

Wind Stress Production:  $G = \frac{m_3 u_*^3}{h}$  , (3.10g)

Dissipation:  $D = E^{1/2}(E + Z)$  (3.10h)

with  $Z \neq 0$  only for the ZSTAR model.

TKE are dissipation, surface heating and entrainment cooling. The last two convert the TKE into potential energy, while dissipation converts the energy into heat. The TKE that is dissipated is effectively lost from the dynamical system of the ocean. However, the TKE used for entrainment continues to be available to the large-scale dynamics, because it influences the potential energy of the system.

For wind-driven regimes, the major TKE source generates horizontal TKE. Since dissipation is isotropic, the horizontal TKE is dissipated at twice the rate of the vertical TKE. Entrainment cooling and surface heating are sinks of vertical TKE only. Also entrainment occurs only to the extent that there is vertical TKE to transport TKE to the entrainment zone. Since the major sources and sinks occur in different TKE components, the transfer of energy between the horizontal and vertical components is very important to the energetics of the OPBL. The mixed layer dynamics are significantly affected since entrainment is controlled by the vertical TKE. The pressure-rate of strain terms provide a mechanism for this transfer that depends, to first

order, on the anisotropy of the turbulence. An additional mechanism is provided by the rotation stress interaction, which depends on the orientation of the planetary vorticity in relation to the relative vorticity of the large-scale turbulent fluctuations.

The pressure-rate of strain terms ( $\Pi$ ) will transfer energy from the horizontal to the vertical component for wind-dominated regimes and from vertical to horizontal for buoyancy driven cases (surface cooling). The direction of transfer for the rotation stress terms (R) depends on the wind direction and not on the anisotropy of the turbulence. As shown in Figure 3.1, the rotation stress transfers energy from the horizontal to the vertical TKE for easterly winds and from the vertical to the horizontal for westerlies. On diurnal to synoptic time scales, either wind direction is possible. However, on seasonal to annual time scales the wind direction will be more persistent. Thus, the possibility exists for variations in the ocean mixed layer response to atmospheric cyclones and anticyclones depending on location relative to the direction and position of each storm.

In the ZSTAR model, the dissipation (D) is increased by the addition of Z (see 3.10h), which is the dimensional counterpart to  $Z_*$ . Thus, Z affects the TKE budget isotropically and is always a sink of TKE. It reduces the entrainment rate by reducing the magnitude of which is the total TKE. The pressure-rate of strain ( $\Pi$ ) is the only TKE conversion mechanism in the ZSTAR model and it always reduces the anisotropy of the turbulence. In the RSTAR model, D is smaller since  $Z = 0$ . Therefore, the TKE is dissipated more slowly, which implies that more TKE is available for entrainment than in the ZSTAR model. The rotation stress (R) is a TKE conversion mechanism similar to  $\Pi$ , but it is independent of the TKE distribution. If the winds are easterlies (westward surface stress), R converts horizontal TKE to vertical TKE, which further increases the entrainment rate. For westerlies, eastward surface stress, R converts vertical TKE to horizontal TKE, which reduces the entrainment rate. For regions with westerly winds, the hypothesis is that R may reduce or eliminate the need for Z in the dissipation parameterization to prevent excessive mixed layer deepening. As is clearly demonstrated in Figure 3.1, the means of reducing the entrainment rate is very different.

#### D. COMPARISON OF RSTAR AND ZSTAR MODELS

The nondimensional entrainment rate is a function of the nondimensional surface buoyancy flux ( $H_*$ ) and the nondimensional depth ( $R_*$  in the RSTAR model or  $Z_*$  in the ZSTAR model). For  $H_* > 0$  (net surface heating), the buoyancy flux is a sink of

TKE (Figure 3.1 and, for example, equation 3.8c) and the mixed layer is in a forced convection or stable regime. In this regime, an equilibrium depth is possible for which the surface buoyancy damping of TKE balances the surface wind stress production. For  $H_* < 0$  (the free convection or unstable regime), the surface buoyancy flux is a source of TKE. Therefore, an equilibrium depth is not possible without some sink of TKE, such as dissipation or rotation stress for westerly wind regimes. The lack of such a steady-state solution was problematic with previous mixed layer models (Chapter II). The ocean mixed layer depth has a cyclical steady-state on an annual time scale. Unless an equilibrium depth is possible for  $H_* < 0$ , this cyclical steady-state solution requires an annual net surface heating or a horizontal divergence in the upper ocean to generate upwelling at the base of the mixed layer.

The  $P_* = 0$  curve is the solution for mixed layer retreat. Therefore, it gives the equilibrium depth as a function of the surface fluxes. For the RSTAR or the ZSTAR models, the  $P_* = 0$  curve crosses the  $R_*$  or  $Z_*$  axis. Therefore, a cyclical steady-state is possible in both models without a net surface heat flux or upwelling. For the ZSTAR model, no equilibrium depth is possible for  $H_* < 0$  (-0.3). For RSTAR, an equilibrium depth is theoretically possible for all  $H_*$ . Thus, the RSTAR model has the potential to maintain a cyclical steady-state for greater wintertime surface cooling rates than does the ZSTAR model.

The entrainment rate decreases with increasing depth for both models (i.e.  $\partial P_*/\partial Z_* < 0$  and  $\partial P_*/\partial R_* < 0$ ). For the same surface fluxes, deep mixed layers will deepen less rapidly than will shallow mixed layers. However, the decreasing curvature of the  $P_*$  solution (Figure 3.2a) for increasing  $Z_*$  (i.e.  $\partial^2 P_*/\partial Z_*^2 < 0$ ) implies that the asymptotic value  $P_*(Z_* \rightarrow \infty)$  is greater than zero. Thus, mixing is still theoretically possible for very deep mixed layers. Changes in  $Z_*$  also are more effective for shallow mixed layers than for deep mixed layers since the curvature is greater for shallow mixed layers. Conversely, the entrainment rate is reduced more rapidly with increasing depth by  $R_*$  (Figure 3.2b) since the curvature of the  $P_*$  solution increases with increasing  $R_*$  (i.e.  $\partial^2 P_*/\partial R_*^2 > 0$ ). This implies that changes in  $R_*$  are more effective for deep mixed layers than for shallow mixed layers. Also, as discussed previously,  $P_*$  must be zero for some value of  $R_* > 0$  for all  $H_*$ . Thus, the RSTAR model can not deepen indefinitely.

The positive curvature of the  $P_*$  solution with respect to  $R_*$  also means that  $P_*$  approaches an asymptotic value as  $R_* \rightarrow -\infty$ . This means that the entrainment rate is

bounded for easterly winds, for the RSTAR model. For easterly winds and zero or positive surface buoyancy flux, the RSTAR model predicts that the equilibrium mixed layer depth given by  $L_{\Omega}$  in (1.7) is negative. Thus in the RSTAR model, an equilibrium mixed layer depth can not be achieved in regions of easterly wind without a positive surface heat flux or a three-dimensional balance of fluxes. For the ZSTAR model, only the condition  $Z_* \geq 0$  prevents  $P_* \rightarrow \infty$  for negative  $Z_*$ .

The ratio  $W_*^2/E_*$  is a measure of the anisotropy of the integral scale TKE. As discussed previously, the large-scale turbulence can not be isotropic since all the production and loss processes are not isotropic (see Figure 3.1). Only the dissipation affects the TKE budget isotropically. If the large-scale turbulence were isotropic,  $W_*^2/E_*$  would be 1/3. For wind-driven regimes, the source of TKE is the shearing in the mean flow generated by the surface wind stress. In this case, TKE is produced only in the horizontal components and  $W_*^2/E_*$  should be less than 1/3. For buoyancy-driven regimes, the TKE production is also anisotropic since the source of TKE is limited to the vertical TKE component. Also the entrainment buoyancy flux is a sink of vertical TKE. In this case,  $W_*^2/E_*$  should be greater than 1/3.

The ratio  $W_*^2/E_*$  is greater for the ZSTAR model (Figure 3.3a) than for the RSTAR model (Figure 3.3b) for all  $Z_*$  and for  $R_*$  greater than zero. This is consistent with the larger values of  $P_*$  in the ZSTAR model. For both models,  $W_*^2/E_*$  increases with decreasing  $H_*$  as the production of TKE by surface buoyancy fluxes becomes the primary source of TKE in the mixed layer. The decrease of  $W_*^2/E_*$  with increasing  $Z_*$  (Figure 3.3a) is much slower than with increasing  $R_*$  (Figure 3.3b) and for  $H_* \sim -0.8$   $W_*^2/E_*$  is virtually independent of  $Z_*$ . The greater variation of  $W_*^2/E_*$  with  $R_*$  is because  $R_*$  directly alters the isotropy of the TKE distribution (see Table 3 or Figure 3.1) by transferring TKE between the eastward and vertical components. On the other hand,  $Z_*$  reduces the TKE by enhancing the dissipation, which is assumed to be isotropic. Thus, the effect of  $Z_*$  on  $P_*$  is more apparent than its effects on  $W_*^2/E_*$  since reducing  $E_*$  directly reduces  $P_*$  (3.8c). However, if the distribution of TKE is not initially isotropic, the isotropic dissipation will make the distribution more anisotropic with time. Thus, for  $W_*^2/E_* < 1/3$  ( $H_* > -0.8$ )  $Z_* > 0$  tends to further reduce  $W_*^2/E_*$ . The trend increases with increasing  $Z_*$ . Thus rate of decrease of  $W_*^2/E_*$  increases with increasing  $Z_*$  and the rate of decrease of  $W_*^2/E_*$  increases as  $W_*^2/E_*$  approaches zero.



These analyses of the nondimensional equations for the TKE models show that the functional form of the entrainment rate ( $P_*$ ) as a function of the rotational dissipation enhancement ( $Z_*$ ) is very different than as a function of rotation stress ( $R_*$ ). The entrainment rate decreases to zero with increasing rotation stress in the RSTAR model. Rotation stress is most effective in altering the entrainment rate for deep mixed layers having large rotation stress since  $\partial^2 P_*/\partial R_*^2 > 0$ . Conversely, the entrainment rate in the ZSTAR model approaches a constant with increasing rotational dissipation enhancement. Also, the dissipation enhancement more effectively alters  $P_*$  for shallow mixed layers with small rotational dissipation enhancement since  $\partial^2 P_*/\partial Z_*^2 < 0$ .

The ratio of the vertical to the total TKE ( $W_*^2/E$ ) is a measure of the isotropy of the TKE distribution among the components. The isotropy of the TKE is affected directly by rotation stress through the transfer of TKE between the east-west and vertical TKE components. However, the dissipation alters the TKE distribution only to the extent that the degree of isotropy of the dissipation rate and the TKE distribution do not match. If the dissipation removes TKE isotropically from the components and if the TKE is not isotropically distributed, the TKE distribution will become more anisotropic with time. Thus, the ratio  $W_*^2/E$  was found to vary more as a function of rotation stress than as a function of rotational dissipation enhancement.

#### IV. SIMULATIONS

The models developed in Chapter III are solved numerically for  $E_*$ ,  $W_*^2$  and  $P_*$  given the surface fluxes of momentum and buoyancy, and for the RSTAR model the wind direction at hourly time intervals. During entrainment, the model density profile is mixed to a depth  $h$  at which the potential energy gained by entraining denser, nonturbulent water from below the OPBL equals the vertical convergence of TKE from the OPBL to the entrainment zone. This depth need not correspond to a level  $n\Delta z$  of the model, where  $n$  is an integer. Thus, these are layer rather than level models. For retreat, the mixed layer depth is set to an equilibrium depth based on the surface fluxes. Then the profile between that depth and the previous depth is adjusted at each intervening level to conserve heat, buoyancy and potential energy. Thus, the density profile in the model consists of a well-mixed layer of depth  $h$  below which the density can vary as a function of  $z$  at intervals of  $\Delta z = 1$  m. The maximum depth for the profile is 200 m.

The long time series of OWS observations, up to thirty years at some locations, allow multiple annual simulations. Shorter case studies also can be repeated in various seasons and years for intercomparison. The disadvantage is that the data are relatively coarsely sampled and crudely measured when compared with the best measurements that can be taken today. Because these higher quality data sets result from intense field experiments that last only weeks to months, important events can be missed and there is no information on seasonal variability. For these reasons and due to its accessibility, the OWS data were chosen for this research because it provides the greatest number and largest variety of events for study.

Both the weather stations used for these studies are at midlatitudes, although equatorial locations would have been preferable. The only time series at an equatorial location that was available for this study is from Gan Island ( $1^\circ\text{S}$ ,  $73^\circ\text{E}$ ) in the Indian ocean. The data set is only 29 months long and contains several data gaps. The island is located in the climatological path of the westward flowing North Equatorial Current in the winter and the eastward flowing Summer Monsoon Current in the summer (Tchernia, 1980). There may be significant three-dimensional effects with large seasonal variability in the data. In fact, in the Gan Island time series there is a strong

2 cycle per year variation in the zonal wind field which drives a zonal jet in the upper ocean as indicated by the 2 cycle per year variation in the upper ocean currents which is in phase with the wind variations (McPhadden, 1982).

Bulk formulas are used to calculate the surface fluxes from the meteorological observations. The values of the coefficients in these formulas are known to vary with latitude and the variations are not as well documented at low latitudes as at midlatitudes (Reed, 1985). The meteorological observations were taken from a weather station on the island and the BT casts were taken several miles alternately north or south of the island at weekly or less frequent intervals (McPhadden, 1982). Thus, the meteorology may suffer from topographical effects due to the island and the BT casts were not collocated with the meteorological observations. For these reasons, the Gan Island data set was rejected for this study.

OWS P ( $50^{\circ}\text{N}$ ,  $145^{\circ}\text{W}$ ) and OWS N ( $30^{\circ}\text{N}$ ,  $140^{\circ}\text{W}$ ) provide time series of data needed for mixed layer simulations on annual time scales. The time series selected for OWS P is fifteen years long and for OWS N eighteen months. For the simulations in this study, the surface fluxes of heat and momentum are calculated from three hourly OWS observations and interpolated to hourly intervals. Since evaporation and precipitation are not measured at ocean weather stations, the surface salinity flux will be neglected. Thus, the surface buoyancy flux is calculated from the net surface heat flux. The density as a function of depth for the upper 200 m of the ocean is needed to initialize and verify the simulations. The OWS observations include BT casts, which provide ocean thermal structure at 5 m intervals throughout the upper ocean at twice daily, or more frequent, intervals. These can be used to calculate density profiles for model initialization and verification if the salinity is known. The initial profiles for the annual simulations are composed of a temperature profile representative of the average thermal conditions for early January for each year and a climatological salinity profile. For OWS P, the salinity profile contains a halocline between the mixed layer and 150 m. The profile above the mixed layer depth (based on the temperature profile) has a constant salinity of  $34^{\circ}/\text{‰}$ , and the salinity below 150 m is constant at  $35^{\circ}/\text{‰}$ . For OWS N, the entire profile is isohaline with a salinity of  $35^{\circ}/\text{‰}$ . Because verification profiles are calculated from BT casts only the temperature portion of the density profile is verified.

Recall that ZSTAR is the Garwood (1977) model, which includes the rotational dissipation enhancement ( $Z_*$ ). RSTAR is the rotation stress ( $R_*$ ) model with no

dissipation enhancement, i.e.  $Z_* = 0$ . HSTAR is the model with no planetary rotation processes, that is  $R_* = Z_* = 0$ . A set of annual simulations will be made using the same empirical tuning constants in all three models (RSTAR, ZSTAR AND HSTAR). In this way, the relative responses of the models to realistic combinations of surface forcing and ocean thermal structure can be compared. Differences in the responses of the models can be attributed directly to the differences in the modeled physics.

Several periods of approximately seven days in duration are selected for further study from these annual simulations. The hypothesis that  $R_*$  can cause significant variations in diurnal to synoptic scale shallowing and deepening events will be tested by comparing the mixed layer depths predicted by the RSTAR, ZSTAR and HSTAR models for these periods. The hypothesis that the isotropy of the TKE distribution for the RSTAR model is different from that of the ZSTAR model will also be tested using these synoptic periods. For this test, the terms in the TKE budget, as detailed in Figure 3.1, will be computed. Another working hypothesis is that the rotation stress,  $R_*$ , in the RSTAR model may reduce or eliminate the need for  $Z_*$ , the rotational dissipation in the ZSTAR model. This hypothesis will be tested by tuning separately the model constants to optimize simulations of the annual cycle of mixed layer depth and temperature for the RSTAR model and the ZSTAR model. Finally, monthly statistics and annual plots of mixed layer depth and temperature will be used to compare the seasonal to annual time scale differences between the RSTAR and ZSTAR models.

#### A. SURFACE FLUX CALCULATIONS

The surface forcing for these studies was calculated using the formulas and constants discussed in Martin (1985). Some of the surface forcing was obtained in flux form from Mr. Paul Martin. The use of the same bulk formulas for the rest of the forcing provided a consistent data set for the simulations. This will also allow further comparison with Martin's results in the future.

The wind stress was calculated using the drag coefficient of Garratt (1977) with the wind speed corrected to a 10-m height using a logarithmic profile of turbulent fluxes in the atmospheric surface layer after the method of Large and Pond (1981). The clear sky insolation was calculated using the Milankovitch formula (List, 1984) with the Reed (1977) cloud cover correction for OWS N and the Tabata (1964) correction for OWS P. The use of two different cloud cover formulas accounted for the variation in the average cloud type and height between OWS P and OWS N (Paul

Martin, personal communication). Net longwave radiation was calculated using the Berliand formula (Wyrski, 1965). Latent and sensible heat fluxes were calculated with bulk formulas using the exchange coefficients of 0.00122 at OWS N and 0.00149 at OWS P as was done by Martin (1985). Solar radiation absorption was calculated using the parameterization of Garwood (1976) in which 50% of the irradiance is absorbed in the first meter, and the remainder is absorbed exponentially with depth. The extinction depth was 22 m for OWS N (corresponding to type I water, Jerlov, 1976), and 12.5 m for OWS P (Jerlov's type II water).

The bulk formulas and the values of the exchange coefficients chosen for the surface heat and momentum flux calculations affect the performance of the mixed layer models. The choice of particular formulas and coefficients for computing the boundary conditions is, in essence, part of the tuning process for the models. In this study, the tuning involved constants that are associated with the parameterizations in the ocean models, rather than by adjusting the atmospheric forcing formulas. This allows the tuning to be done with respect to the physical processes that are parameterized in the models. The models can then be compared using the same surface fluxes and the differences in model simulations can be ascribed to differences in model physics.

Martin (1985) performed sensitivity studies of the bulk formulas and exchange coefficients for OWS P and OWS N. Gallacher *et al.* (1983) performed sensitivity studies for the solar radiation absorption formulation. Gallacher *et al.* (1983) also compared this parameterization with several others, including the arctangent model of Zaneveld and Spinrad (1980) and the multiple wavelength model of Kondo (1979), and concluded that these more involved parameterizations did not significantly alter the depth-dependent ocean heating due to shortwave radiation. The choices of formulas and coefficients for this study were based on those results. The choices provide a model-independent set of surface fluxes with the minimum annual bias in net surface heating that is consistent with direct observations of surface fluxes.

## **B. DESCRIPTION OF OCEAN WEATHER STATION DATA**

Annual simulations were conducted for OWS P (50°N, 145°W) and OWS N (30°N, 140°W). At OWS P, the years 1961, 1965, 1966 and 1967 were chosen because these years each had more than 2000 BT casts that could be used for model verification. In 1965, 1966 and 1967, the observations were distributed rather uniformly throughout the year (Figures 4.1b-4.1d). In 1961 (Figure 4.1a), the BT observations were clustered around several intensive observation periods for the

Internal Wave EXperiment (IWEX). Furthermore, 1961 was the year used by Martin (1985) for an intercomparison of the ZSTAR model, the Niiler (1975) model and the Mellor and Yamada (1974) level 2 and 2 1/2 models, at OWS P and OWS N. The ZSTAR model predicted the seasonal cycle better than did the Mellor models or the Niiler model. The ZSTAR model provided a good simulation at OWS N but tended to shallow too much in late summer and/or deepen too rapidly in the fall at OWS P, depending on the model constants. Thus, the ZSTAR model provides a good comparison model since it is as good or better than other state of the art vertically-integrated models. The observations for 1961 at OWS N are distributed uniformly throughout the year (Figure 4.1e). However, there are only 1650 observations compared to an average of 2350 for the years at OWS P.

OWS P is in a region of predominately westerly winds. OWS N is in a region of predominately easterly winds during the spring, summer and fall. The wind direction at OWS N is more variable during the winter when the subtropical high pressure center moves south to approximately  $30^{\circ}\text{N}$ ,  $140^{\circ}\text{W}$  from its summertime position of approximately  $40^{\circ}\text{N}$ ,  $150^{\circ}\text{W}$  (Tchernia, 1980). For 1961, the wind direction at OWS N is southerly to southwesterly in January and early February then predominately easterly for the rest of the year. These stations are separated by  $20^{\circ}$  latitude. Thus, it might seem they provide an appropriate test for the wind direction and latitude dependence of rotation stress. However, the conditions at OWS P and OWS N differ in more than these aspects (Elsberry and Camp, 1978). The magnitude of the wind forcing and surface heating varies considerably from OWS P to OWS N as shown in Table 7. The values in Table 7 suggest that the heat budget for 1961 at OWS N may be more one-dimensional than at OWS P, since the magnitude of the annual net surface heating ( $17 \text{ W m}^{-2}$ ) at OWS N is less than the magnitude of the annual net surface cooling ( $25 \text{ W m}^{-2}$ ) at OWS P for the same year. There is no evidence at either location of a climatological heating or cooling trend. Therefore, any net heating or cooling from the atmosphere must be balanced by a horizontal or vertical heat flux in the ocean.

The climatological oceanographic conditions indicate that OWS P is located in a region more likely to be dominated by the local atmospheric forcing than is OWS N. Because OWS N is located within the region of influence of the subtropical front, horizontal advection, convergence and divergence are expected to be more significant (Tchernia, 1980). Indeed, there are indications in the temperature time series at OWS

N that the subtropical front oscillates across the station. Climatologically, the ocean surface currents at OWS N are from the north and northeast. This current, which is part of the California Current system, transports colder water into the region of OWS N. Thus, a net cooling due to horizontal transport is possible. At OWS P, the climatological currents, which form the northern edge of the subtropical gyre, are from the west. The currents are weaker on average than at OWS N and the transport is along the isotherms rather than nearly normal to the isotherms as at OWS N. Therefore, the net heat transport is expected to be smaller at OWS P than at OWS N on average. Thus, the wind direction and latitude are only two of many differences between these ocean weather stations. Differences between the simulations and observations will reflect all the variations in atmospheric forcing and oceanic conditions. However, by choosing periods of diurnal to synoptic time scales, during late winter to early spring the effects of planetary rotation are likely to be most apparent.

Martin (1985) observed that the ZSTAR model predicted a mixed layer depth at OWS P that was slightly deeper than observed during the summer and early fall, whereas the mixed layer depth was well predicted at OWS N. The equilibrium mixed layer depth for the RSTAR model is given by

$$L_{\Omega} = \frac{C_1 L_0}{(1 + C_2 \Phi)} \quad (1.7)$$

and for the ZSTAR model by

$$L_0 = \frac{\tau^{3/2}}{bw(0)} \quad (1.8)$$

The ratio of rotation stress to surface buoyancy flux is given by (1.9)

$$\Phi = \frac{\Omega_y \tau_x}{\rho bw(0)} = \frac{R_{*}}{H_{*}} \quad (1.9)$$

In Garwood *et al.* (1985a), we showed that typical summertime values are  $\Phi = 0.19$  at OWS P and  $\Phi = 0.08$  at OWS N. These values have the correct magnitude and sign to improve the mixed layer depth prediction at both OWS P and OWS N because the resulting equilibrium depth for the RSTAR model relative to that for the ZSTAR model is smaller at OWS P than at OWS N. The value of  $R_{*}$  (3.6f) relative to the surface buoyancy flux  $H_{*}$  (3.6e), rather than the absolute magnitude of  $R_{*}$ , determines the efficacy of  $R_{*}$  for altering the equilibrium depth.

TABLE 7  
ANNUAL AVERAGE SURFACE FLUXES AT OWS P AND N

	$\tau_x$	$\tau_y$	$Q_s$	$Q_b$	$Q_e$	$Q_h$	$Q_n$
	(N m <sup>-2</sup> )		(W m <sup>-2</sup> )				
OWS P							
1961	0.102	0.013	216.	94.	86.	11.	-25.
1965	0.099	0.013	221.	98.	103.	19.	-1.
1966	0.080	-0.005	216.	95.	99.	19.	-3.
1967	0.100	0.012	223.	99.	108.	17.	1.
OS N							
1961	-0.030	-0.006	349.	111.	227.	28.	17.

$\tau_x$  is the east-west component of surface wind stress  
 $\tau_y$  is the north-south component of surface wind stress  
 $Q_s$  is the solar radiation (positive downward)  
 $Q_b$  is the longwave radiation (positive upward)  
 $Q_e$  is the evaporative heat flux (positive upward)  
 $Q_h$  is the sensible heat flux (positive upward)  
 $Q_n$  is the net heat flux ( $Q_b + Q_e + Q_h - Q_s$ )

### C. SYNOPTIC-SCALE INTERCOMPARISONS OF MODELS

Several synoptic-scale periods are chosen from annual simulations of 1965 and 1967 at OWS P and from the annual simulations of 1961 at OWS N to demonstrate the latitudinal and seasonal variations among the RSTAR, ZSTAR and HSTAR models and the time scales of these variations. As discussed in the introduction,  $R_*$  decreases with increasing latitude. Conversely,  $Z_*$  increases with increasing latitude. The time scale of variations in the rotation stress ranges from the inertial scale of the planetary rotation to synoptic scale of the variations in wind direction.

Both  $Z_*$  and  $R_*$  are proportional to  $h$ . Because the mixed layer is at or near a deep equilibrium state during late winter, diurnal to synoptic scale events that occur during late winter or during the spring transition are most likely to be affected by  $R_*$  and  $Z_*$ . The spring transition is that period when the mixed layer changes from the deep equilibrium state to the shallow summertime regime. This change can occur quite abruptly due to the modulation of the mixed layer depth by the diurnal cycle of surface heating. The transition occurs on a day when the wind stress production of TKE is not sufficient to return the mixed layer to the deep equilibrium depth from which the diurnal retreat began. The date of this transition is significantly correlated at OWS P with the accumulation of heat above the seasonal thermocline (Elsberry and Garwood,



1978). Rotation stress may affect this transition by augmenting (easterly wind regimes) or reducing (westerly wind regimes) the entrainment rate. The frequency of diurnal and synoptic-scale cycles of shallowing and deepening in the RSTAR simulations are quite different from those for the ZSTAR model during the late winter to early spring for all five years of this study (Figures 4.10a through 4.14a).

In the summer, the winds are light, the surface heating is large and the insolation is near the annual maximum. Consequently, the layer is probably too shallow for  $R_*$  or  $Z_*$  to significantly affect the TKE budget. During the fall deepening period, wind mixing and surface cooling dominate the TKE budget and the entrainment rate is primarily determined by the net TKE production and the density gradient below the mixed layer. The direct effects of  $R_*$  are expected to be dominated by the TKE production due to wind stress and surface cooling, and the TKE loss due to entrainment cooling and dissipation. Although variations in the density profile of the seasonal pycnocline caused by rotation stress during the spring transition could later affect the fall deepening, demonstrating such seasonal teleconnections would be very difficult. For these reasons, the winter-spring period was examined for examples of the influences of rotation stress. Synoptic periods characteristic of the summer and fall conditions, as discussed above, were also chosen to demonstrate the seasonal variability.

For these simulations, the values of the tuning constants are a compromise among the values that were determined for the RSTAR and ZSTAR models by optimizing the simulations of the annual cycle at OWS P for 1965, and the values determined from theoretical estimates and from independent experimental results (see the next section for details concerning the tuning and the optimal values for each model). The value for  $p_1$ , which is a measure of entrainment efficiency, is 0.3. It controls the size of the entrainment cooling relative to the dissipation (Figure 3.1). The strength of the pressure redistribution term relative to the dissipation is  $p_2$ , which is equal to 0.5 for these simulations. The relative efficiency of TKE production due to wind and breaking surface waves is  $m_3$  ( $m_3 = 7.5$ ). The rotation stress term does not contain a tuning constant, as can be seen in Table 2. The coefficient for  $Z_*$  is  $p_3$ . It is a measure of the dissipation enhancement due to rotation (Table 2). For these simulations,  $p_3$  is set equal to 1.0. The depth-averaged, dimensional variables defined in equations (3.10a)-(3.10f) of Table 2 will be used for the comparisons in this section. These variables differ from the nondimensional variables in that they are independent

of mixed layer depth and the wind stress production becomes an explicit term, ( $G = m_3 u_*^3$ ).

An example of the winter through spring transition period is the seven days taken from the annual simulations of 1967 at OWS P (Figure 4.2). A most striking feature of this period is that the RSTAR and HSTAR models deepen much more rapidly than the ZSTAR model (Figure 4.2a). After 100 days of simulations, all three models predict similar mixed layer depths. Then the ZSTAR model deepens to 90 m on day 103.5 while the HSTAR and RSTAR models deepen through the permanent pycnocline, to a depth of 175 m in the same time span. This divergence of the entrainment rates ( $P$ ) is not due to variations in the simulated density profiles below the mixed layer, as will be demonstrated below. It results from the reduced dissipation ( $D$ ) in the HSTAR and RSTAR models relative to that in the ZSTAR model (Figure 4.2b). The TKE that is made available by this reduction in  $D$  is used to increase  $P$  (Figure 4.2c). The result is that the mixed layer in the ZSTAR model deepens more rapidly, while the TKE remains approximately the same for all three models (Figure 4.2g).

An alternative hypothesis is that the structure of the seasonal pycnocline immediately below the mixed layer in the HSTAR and RSTAR simulations is different from that of the ZSTAR simulation due to variations in mixed layer depth and density during the preceding 100 days of the simulations. If that is the case, the rates of mixed layer deepening and the ultimate equilibrium depths are different due to the differences in the pycnocline structure into which the mixed layer is entraining rather than to variations in the mixed layer TKE budget. To test this hypothesis, the RSTAR and HSTAR simulations were recalculated starting on day 101 with the profile for that day and time generated by the ZSTAR model. The results (not shown) are similar to Figure 4.2. The HSTAR and RSTAR models deepened more than the ZSTAR model and achieved a final equilibrium depth of approximately 150 m. This is shallower than the 175 m equilibrium depth in Figure 4.2a. However, the variations in deepening rate, dissipation rate, vertical and total TKE are sufficiently similar to those in Figure 4.2 to conclude that they are primarily the result of the variations in the TKE budget, rather than variations in the underlying thermocline.

The crosses in Figure 4.2a (and in the subsequent mixed layer depth plots) are the mixed layer depths calculated from the OWS data. For the data, the mixed layer depth is defined as the greatest depth with a temperature less than  $0.1^\circ\text{C}$  colder than the sea-surface temperature. The trend of the mixed layer depth predicted by the

ZSTAR model agrees with the data better than does that predicted by the HSTAR and RSTAR models (Figure 4.2a). However, the most interesting times for comparisons among the RSTAR, ZSTAR and HSTAR models are the diurnal retreat-deepening events (Figure 4.2a) around days 104, 105, 106 and 107. During these events, the mixed layer is quite deep compared to typical values for the summer or fall (Figures 4.5 and 4.6) even at the shallowest point of these retreat events (approximately 100 m for the RSTAR and HSTAR models). Thus, the rotation stress and the rotationally enhanced dissipation will have maximum effect on the dynamics of the mixed layer. The diurnal events predicted by all three models are not clearly represented in the data. There does appear to be some diurnal period variations in the data, particularly around days 105 and 106, which have a larger amplitude than that predicted by the ZSTAR model. The amplitude of the variations, roughly 50 to 100m, appears to agree better with the amplitude of the events predicted by the HSTAR and RSTAR models than with that predicted by the ZSTAR model. The ZSTAR model appears to fit the long-term trend in the data. However, the RSTAR model may better predict the diurnal events that appear in the data, although the average mixed layer depth in the RSTAR model is clearly too deep.

There is a large diurnal to synoptic time scale signal in  $W^2/E$  (Figure 4.2h) since  $W^2=0$  whenever the mixed layer retreats. In the RSTAR and HSTAR models, this ratio is two to six larger than in the ZSTAR model. However, this increase is not accompanied by an increase in the total transfer rate,  $\Pi-R$ , (Figure 4.2i) as might be expected from Figure 3.1. In fact, the total transfer rate for the RSTAR and HSTAR models is less than for the ZSTAR model. Thus, the increase in  $W^2/E$  is not the result of increased transfer of TKE from the horizontal to the vertical component. It is a direct result of the decreased dissipation (see below).

Since the dissipation is specified to be isotropic, dissipation of the vertical TKE accounts for 1/3 of the total TKE dissipated (Figure 3.1). The vertical TKE is approximately 5% of the total TKE in the HSTAR and RSTAR models and only 1% in the ZSTAR model (Figure 4.2h). Therefore, removing a third of the total dissipated TKE from the vertical component may account for the difference between the estimates from the experimental results and the model results. If this is the case, the TKE distribution may be less isotropic in the simulations, particularly in the ZSTAR simulation, than it is in nature. This tentative conclusion can not be verified with the data being used in this study. Thus it must be left as a hypothesis to be tested in future work.

The diurnal mixing events can be explained in terms of the TKE budget shown in Figure 3.1. The mixed layer depth is well correlated with  $H$ , the dimensional, depth-averaged surface buoyancy flux (3.10c). The shallowing corresponds to the increasingly positive  $H$  that results from the diurnal increase in insolation. The maximum  $H$  occurs at the minimum depth of the cycle, which corresponds to  $W^2/E = 0$ , and  $H$  acts as a sink of vertical TKE. Although the existence and vertical range of the events do depend on  $G$  (3.10g), the depth of the mixed layer is poorly correlated with  $G$  and  $D$  throughout the events. The average value of  $G$  is approximately  $2.0 \times 10^{-3} \text{ cm}^2 \text{ s}^{-3}$ . This is the major source of TKE during most of the events. With the primary source of TKE in the horizontal component and the major sink in the vertical, the total TKE transfer ( $\Pi - R$ ) achieves a local maximum value of  $1.0\text{-}2.0 \times 10^{-3} \text{ cm}^2 \text{ s}^{-3}$  during each event. In all cases,  $P = 0$  until the minimum depth is achieved and then  $P$  increases to a maximum value of approximately  $1.5 \times 10^{-4} \text{ cm}^2 \text{ s}^{-3}$  at the point of maximum depth. The behavior of  $P$  mimics that of  $W^2/E$ , as expected. The maximum value of  $W^2/E$  is about 0.1 to 0.2. For the ratio of rotation stress to surface buoyancy flux ( $\Phi > 0$ ) the RSTAR model should retreat to a shallower depth than the HSTAR model, for which  $R = 0$ . This is confirmed in Figure 4.2a, since the mixed layer depth for the RSTAR model is always shallower than for HSTAR.

When variations in  $G$  and  $R$  are in phase, the wind direction must be easterly. This is generally the case in the events discussed here. At the start of the event on day 104,  $R$  (Figure 4.2e) and  $G$  (Figure 4.2d) are no larger than in other events. However, the event corresponds to a local maximum for  $R$  and local minimum for  $G$ . This implies that the wind speed is reduced and the direction shifted such that the winds were blowing from the east. All the other events are local minimums for both  $R$  and  $G$ . This extra conversion of vertical to horizontal TKE due to the increasing  $R$  during day 104 is coupled with a reduction of TKE due to decreased  $G$  throughout the period. Consequently, the RSTAR model retreats 30 m whereas the mixed layer depth in the HSTAR model does not change. Conversely, both models retreat equally for the event of day 107 because  $R$  is approximately zero throughout the period (Figure 4.2e). The smaller rate of deepening of the RSTAR model compared to the HSTAR model for days 101 through 103 is a direct result of the reduced total transfer,  $\Pi - R$ , (Figure 4.2i) due to the positive  $R$  (Figure 4.2e). This difference in the rate of deepening also appeared in the test for which the RSTAR and HSTAR models were restarted at day 101. Therefore, it is not a consequence of any differences in the pycnocline structure below the mixed layer.

Another case during the winter through spring transition is from OWS P during days 72-80 of 1965 (Figure 4.3). The most significant difference between this case and the previous one (Figure 4.2) is that  $R$  is negative throughout most of the period because the winds are easterly. As a result, the mixed layer depth (Figure 4.3a) from the RSTAR simulation is deeper than that from HSTAR by approximately 10%. The ZSTAR model is shallower than either the HSTAR or RSTAR model and the mixed layer depths calculated from the BT casts are generally closer to the ZSTAR solution. However, there still appears to be more diurnal to synoptic scale variability in the data than in the ZSTAR model predicted depths. For ZSTAR, the average  $W^2/E$  (Figure 4.3h) is small, about 0.01, as in the previous case. For HSTAR,  $W^2/E$  is about twice the previous value. For the RSTAR model,  $W^2/E$  is 20% larger than for the HSTAR model. This results from the enhanced transfer of TKE from the horizontal to the vertical component. In this case,  $R_*$  acts to increase the isotropy of the TKE budget. During the synoptic period from day 74 through day 77, the mixed layer from the RSTAR simulation becomes increasingly deeper than the mixed layer depth from HSTAR (Figure 4.3a) since the winds are easterly throughout the period. As the mixed layer deepens and the entrainment rate shows the average  $W^2/E$  (Figure 4.3h) decreases.

A final example during the winter-spring transition is from OWS N during days 77-84 of 1961 (Figure 4.4). For this case,  $R$  oscillates between positive and negative values with a two to three day period (Figure 4.4e). The positive peaks in  $R$  correspond to peaks in  $G$  (Figure 4.4d); whereas  $R < 0$  events corresponds to low wind speeds. For this case, the mixed layer depths (Figure 4.4a) predicted by all three models are similar, due to the relatively large production of TKE by the surface buoyancy flux. In this example,  $H$  (Figure 4.4f) is more negative by approximately a factor of two than for the 1967 OWS P case (Figure 4.2f). The mixed layer depths calculated from the BT casts do not show the diurnal cycles predicted by all three models. No model fits the data appreciably better than the other two. The mixed layer from the RSTAR simulation is shallower than from the HSTAR simulation when  $R$  is positive on day 78 and deeper on day 79 when  $R$  is negative. The ratio  $W^2/E$  (Figure 4.4h) is greater than 0.33 for all the deepening events which indicates that the events are buoyancy-driven. For the deepening event on day 79,  $W^2/E$  from the RSTAR model is larger than for the HSTAR or ZSTAR model. This is a direct result of the enhanced transfer of TKE from the horizontal to the vertical component due to

the negative R. The isotropy of both the RSTAR and HSTAR models are greater than for the ZSTAR model due to the reduced dissipation in those models. At the start of day 79, the dissipation (Figure 4.4b) in the ZSTAR model is roughly 50% larger than in the RSTAR and HSTAR models.

It was hypothesized that the effects of R and Z would be the greatest during the winter through the spring transition period discussed above. The effects of planetary rotation should be smaller during summer since the mixed layer is relatively shallow and the winds are light. A synoptic period from days 210 to 217 at OWS P during 1967 will be used to verify this hypothesis. For this period (Figure 4.5), the three models give virtually identical results. The average for R during this period is almost zero and the maximum value of  $3.0 \times 10^{-5} \text{cm}^2 \text{s}^{-3}$  (Figure 4.5e) is more than a factor of 10 smaller than the maximum value for the winter case (Figure 4.2e). The mixed layer depth,  $O(3 \text{ m})$  (Figure 4.5a), and the average ratio of vertical to total TKE of 0.07 (Figure 4.5h) are virtually identical for all three models.

In the fall (Figure 4.6), R and Z are more effective than in the summer. However, the mixed layer deepening is accelerating mainly in response to increasingly large wind stress and positive surface buoyancy flux. For the period in Figure 4.6, days 250 to 257 from OWS P for 1967, the average wind stress production is  $G = 1.0 \times 10^{-2} \text{cm}^2 \text{s}^{-3}$  (Figure 4.6g) and the surface buoyancy flux (Figure 4.6f) is  $-6.0 \times 10^{-4} \text{cm}^2 \text{s}^{-3} \leq H \leq 4.0 \times 10^{-4} \text{cm}^2 \text{s}^{-3}$ , with negative values indicating production of TKE. By contrast, the average R is only  $5.0 \times 10^{-5} \text{cm}^2 \text{s}^{-3}$ . During this period, all three models are deepening at similar rates. The rate of mixed layer deepening is limited not only by the rate of production of TKE by the surface fluxes but also by the strength of the pycnocline. For example, the fairly substantial storm on day 255 (maximum  $G = 3.0 \times 10^{-2} \text{cm}^2 \text{s}^{-3}$  and a maximum  $H = -4.5 \times 10^{-4} \text{cm}^2 \text{s}^{-3}$ ) only deepened the mixed layer 5m. The mixed layer depth from the ZSTAR model is approximately 25% shallower than that of the HSTAR or RSTAR models throughout the period and  $W^2 E$  is smaller because of the enhanced dissipation in the ZSTAR model. However, the rate of deepening  $O(1 \text{ m day})$  is approximately the same for all three models and the difference between the RSTAR and HSTAR models is negligible even for the large negative R ( $-4.0 \times 10^{-4} \text{cm}^2 \text{s}^{-3}$ ) on day 254.5. This indicates that the rate of transfer of TKE between the horizontal and vertical components is not a significant part of the TKE budget during this period. These synoptic periods are typical of the seasons represented.

To summarize the results of the cases discussed above, both  $R_*$  and  $Z_*$  were shown to be relatively ineffectual during the summer and fall. During the winter through the spring transition,  $R_*$  and  $Z_*$  substantially alter the diurnal to synoptic scale mixing events and the long term trend in mixed layer depth. Variations in the dynamics of the upper ocean can be described in terms of the TKE budget of the OPBL (Figure 3.1). The isotropy of the TKE distribution for the OPBL changes substantially on diurnal to synoptic time scales. The turbulence is likely to be most anisotropic for retreat events ( $W_*^2 \rightarrow 0$ ). The isotropy of the TKE budget predicted by the RSTAR model is considerably different than that predicted by the ZSTAR model, as is the entrainment rate. For the RSTAR model, the isotropy (e.g., Figure 4.2h) is larger than for the ZSTAR model by as much as a factor of 10 and the entrainment rate (e.g., Figure 4.2c) is 2 to 2.5 times greater than for the ZSTAR model. These results from the synoptic scale studies appear to contradict the nondimensional results. The latter predicted greater variation in the isotropy (Figure 3.3b) and reduced entrainment rate (Figure 3.2b) as a function of  $R_*$ , particularly for deep mixed layers. This apparent contradiction is due to the smallness of  $Z_*$  and, particularly,  $R_*$  in the synoptic studies. For the winter-spring transition cases most values were in the range  $0 \leq Z_* \leq 0.5$  and  $0 \leq R_* \leq 0.1$ . In the nondimensional plots the values are  $0 \leq Z_*, R_* \leq 2.0$  for  $P_*$  and  $0 \leq Z_* \leq 1.0$ ,  $-0.5 \leq R_* \leq 0.5$  for  $W_*^2/E$ . The maximum values used in the nondimensional plots are well within the range of reasonable values at OWS P and OWS N but these larger values do not occur for the near equilibrium situations shown in the synoptic scale figures.

At least for the parameter values used in the synoptic studies,  $R_*$  did not provide sufficient damping of  $P_*$  to prevent excessive mixed layer deepening for the winter cases. However, the ZSTAR model predicts a significantly less isotropic TKE balance in the OPBL. The isotropy of shear-forced mixing layers can be estimated from various laboratory studies that have been reported in the literature (Table 8). There are no field measurements in the upper ocean, from which estimates of the isotropy of the integral scale turbulence can be made. Based on the estimates in Table 8, the average value of  $W_*^2/E \sim 0.05$  for the RSTAR and HSTAR models probably is an underestimate and the value of  $W_*^2/E \sim 0.01$  for the ZSTAR model very likely is an underestimate (Figure 4.2h). However, the laboratory measurements are for wall-bounded, pure shear flows. The OPBL is bounded by a free surface and there can be significant production and damping of the TKE by buoyancy fluxes. For the case of

buoyant damping, the isotropy of the OPBL should be less than the estimates from the laboratory measurements, which are for neutrally buoyant flows.

TABLE 8  
ESTIMATES OF THE ISOTROPY OF WALL-BOUNDED SHEAR LAYERS

Source	Type of Flow	$W_*^2 E_*$
Smits et al. (1979)	Convex curvature	0.16
Muck et al. (1985)	Convex curvature	0.22
Townsend (1976)	Flat plate	0.25
Hunt and Joubert (1979)	Convex curvature	0.25
So and Mellor (1973)	Convex curvature	0.29

The temporal and spatial resolution and the precision of the OWS data sets used in this study was not sufficient to verify the increased frequency and magnitude of diurnal to synoptic scale shallowing-deepening events predicted by the RSTAR model. Further simulations are recommended using data from experiments such as the Storm Transfer and Response EXperiment (STREX) and the Mixed Layer Dynamics EXperiment (MILDEX) to verify the effects of rotation stress. These experiments were intense synoptic period observations of the upper ocean and the surface fluxes at higher temporal resolution and with greater accuracy and precision than the OWS data. However, these data sets may not contain events with the east-west wind stress, which is needed to test the variations among the models. A set of experiments aimed specifically at verifying the rotation stress effects may be required. Measurement of surface stress to  $\pm 1.0 \times 10^{-2} \text{ N m}^{-2}$  and surface heat fluxes to  $\pm 10 \text{ W m}^{-2}$  are now possible (Large *et al.*, 1986). These should produce sufficiently accurate surface fluxes to test the models introduced in this research. The capability now exists to measure temperature profiles to millidegree precision. This would allow the differences in simulated mixed layer temperature and depth among the models to be tested along with the assumption of a "well-mixed" similarity profile.

The magnitude of the processes that affect the TKE budget (e.g.  $R$ ,  $D$ , and  $\Pi$ ) calculated for the synoptic scale studies vary from  $10^{-5} \text{ cm}^2 \text{ s}^{-3}$  to  $10^{-2} \text{ cm}^2 \text{ s}^{-3}$ , and the magnitude of the TKE is  $O(10^{-2} \text{ cm}^2 \text{ s}^{-2})$ . The difference between the values of  $W_*^2 E_*$  predicted by the RSTAR and ZSTAR models implies a difference in vertical TKE averaged over the mixed layer of  $2 \times 10^{-3} \text{ cm}^2 \text{ s}^{-2}$ . Differences in the magnitudes of  $R$ ,  $D$ ,



$\Pi$  and the other processes shown in Figure 3.1 range from  $10^{-5}\text{cm}^2\text{s}^{-3}$  to  $10^{-3}\text{cm}^2\text{s}^{-3}$  between the RSTAR and ZSTAR models. The lower limit for measurements of the rate of dissipation of TKE in the ocean is  $2.0 \times 10^{-6}\text{cm}^2\text{s}^{-3}$  (Osborn and Lueck, 1984) due to instrument noise. Thus, the differences in the TKE budgets calculated in this work may be measurable with current technology. These dissipation measurements resulted from microstructure measurements of turbulent velocity shear, absolute values of turbulent velocity may not be measurable to the same precision. Also horizontal transects through the mixed layer would be required to collect time series of sufficient duration to obtain stable correlations of the turbulent velocity components. Such transects are difficult even using a relatively stable underwater platform such as a submarine (Rolf Lueck, personal communication).

These studies of synoptic periods selected from annual simulations with the RSTAR, ZSTAR and HSTAR models demonstrated that for the same values of the tuning constants the models predicted quite different responses to the same forcing. Rotation stress changes the frequency and magnitude of diurnal to synoptic scale shallowing and deepening events predicted for deep mixed layers. During these events, the depth changes calculated by the RSTAR model were 10% to 30% greater than those calculated by the HSTAR model. Simulations from both these models were substantially different from simulations with the ZSTAR model during the winter, during spring transition and during the fall deepening. All three model calculated similar summertime mixed layers. The TKE distributions predicted by the RSTAR and HSTAR models were 10% to 40% larger and more isotropic than that predicted by the ZSTAR model. This was the result of the larger dissipation associated with the inclusion of the rotational dissipation enhancement in the ZSTAR model. The dissipation is assumed to be isotropic in all three models, whereas  $W_*^2 E_*$  was usually less than 0.1 in the simulations. Laboratory measurement indicate that the values for  $W_*^2 E_*$  are probably too small.

#### D. TUNING USING ANNUAL SIMULATIONS

For the simulations discussed in the previous section, the values of the tuning constants were based primarily on theoretical estimates and experimental results. As discussed, the ZSTAR model simulations best fit the trends in the data. In general, any of the models could be tuned to estimate the trend in the data for synoptic-scale periods. This is due partly to the relatively narrow range of surface fluxes and mixed layer variations that occur over such short periods. However, annual periods include a

sufficiently broad range of physical processes that tuning alone is not sufficient if the model physics is inadequate or incomplete. As discussed in Chapter II, the need for a mechanism to prevent excessive wintertime mixing in bulk models is well known. The purpose of this and the following section is to demonstrate the requirement for such a mechanism and to determine the extent to which rotation stress may provide this mechanism for regions of westerly wind. The results of Garwood *et al.* (1985b) suggest the possibility that rotation stress may eliminate the need for rotationally enhanced dissipation on seasonal to annual time scales. The hypothesis for this section is that, for the proper values of the tuning parameters, the RSTAR model can simulate the annual cycle of the OPBL for westerly wind regimes without excessive winter deepening or a generally poor fit to the annual cycle.

The RSTAR and ZSTAR mixed layer models are optimally tuned for this part of the study. That is, the model constants are adjusted in an attempt to obtain a best fit to the observed mixed layer depth and temperature. A more complete discussion of the definition of best fit between the models and observations is given below. The rotation stress term does not contain a tuning constant. However, altering the constants in the other terms implicitly alters the effects of  $R_*$ . Because the models are nonlinear the effects of the physical processes are not independent and all the constants must be adjusted if the models are to be optimally tuned for a given set of physical processes.

The parameters that will be tuned and the processes they affect are shown in Figure 3.1. For the models discussed in this work, the efficiency of TKE production due to wind and breaking surface waves and the convergence of TKE within the mixed layer is  $m_3$ . The entrainment efficiency is  $p_1$ . The strength of the pressure redistribution term is determined by  $p_2$ . In the ZSTAR model, the  $p_3$  coefficient for  $Z_*$  is a measure of the strength of the dissipation enhancement. The coefficients  $p_1$ ,  $p_2$  and  $p_3$  are all defined relative to the lowest order parameterization of dissipation,  $E_*^{3/2}$ . The RSTAR model contains three tuning parameters whereas the ZSTAR model contains four.

The 1965 data at OWS P were chosen for these tuning experiments because of the large number of evenly distributed observations (Figure 4.1c). Furthermore, the one-dimensional mixed layer model assumptions are met since the net annual heating was relatively small during that year (Table 7). The models were tuned by choosing a set of statistical measures to be minimized on an annual time scale. The statistical parameters chosen were the bias,

$$X_{\text{bias}} = (\sum x_m - \sum x_d) / N$$

and the root mean square error (RMSE),

$$X_{\text{rmse}} = \left\{ \sum [(x_m - x_d)^2 / N] \right\}^{1/2}$$

of the mixed layer temperature (T) and depth (h). In the above definitions, the  $x_m$ 's are the simulated values and the  $x_d$ 's are the observations. The summations are over all BT casts for the year and the concurrent model value is specified at the hour nearest the time of the BT cast. The bias measures the fit of the phase and amplitude of the low frequency (seasonal to annual time scale) variability between the observations and the simulations. Matching the timing and peak values of the summertime maximum temperature and minimum depth and the wintertime minimum temperature and maximum depth between the observations and the simulations will minimize the bias. The RMSE is minimized by matching the phase and amplitude of the high frequency (synoptic to diurnal period) variability in the model and the observations.

For a specified value of  $p_2$ , the bias in the RSTAR model can be minimized for the locus of  $(m_3, p_1)$  points defining the zero contour lines on Figures 4.7a and 4.8a for the depth and temperature, respectively. If  $p_2$  is increased, the zero contour is shifted toward smaller  $(m_3, p_1)$ , but the curvature remains roughly the same. Thus, the zero bias for temperature or depth forms a surface in  $(m_3, p_1, p_2)$  space that decreases with increasing  $p_2$  and has concave curvature in the  $(m_3, p_1)$  plane. If  $p_2$  is increased, the transfer of TKE from the horizontal to the vertical increases. Thus, the same mixed layer depth and temperature could be achieved with less TKE production ( $m_3$ ) and less effective mixing ( $p_1$ ). For fixed  $p_2$ , increasing the TKE production ( $m_3$ ) implies that less efficient mixing (reduced  $p_1$ ) is needed to achieve the same mixed layer depth (MLD) and mixed layer temperature (MLT).

Although the temperature (Figure 4.8b) and depth (Figure 4.7b) RMSE's have a pattern similar to that of the biases, they do not overlay the zero bias contours. Rather the RMSE minima correspond to biases for which the model is warmer (Figure 4.8a) and shallower (Figure 4.7a) than indicated by the observations. A shallower OPBL will tend to have more high frequency variability due to the reduced thermal inertia. The rather large RMSE's indicate that the model variations lack some of the high frequency variability that exists in the BT data. The high frequency variations in the BT data may be due to such factors as noise, motion of the ship on station, horizontal advection of the temperature patchiness that has been observed in the upper ocean (R. W. Garwood, personal communication), or it may be due to the differences

in definition of MLD and MLT for the model and the data. Some bias in model versus data comparisons can be expected from the difference between the observational definition of MLD and MLT given above and the model MLD and MLT. In particular, the large minimum RMSE and the displacement of the RMSE minimum relative to the zero bias is consistent with this difference in definition. This study is concerned more with comparing the physical processes parameterized in the RSTAR and ZSTAR models than with achieving the optimal model versus data comparison. Therefore, no attempt will be made to correct for any possible biases that may be associated with the different definitions of MLD and MLT.

As discussed above, the minima of the temperature and depth biases and RMSE's for the RSTAR model form surfaces in  $(m_3, p_1, p_2)$  space. There is no indication that the minimum values become smaller anywhere in parameter space or that the surfaces converge. Thus, the fit between the RSTAR model and the data, at least based on these statistics, will not improve significantly for some set of parameter values different from the values of the tuning constants used in the previous section. The conclusion is either that  $R_*$  can not eliminate  $Z_*$  at midlatitudes on annual time scales or that these annual statistics are insufficient to allow quantitative tuning of the model.

The statistical estimates that were chosen are not perfect since the values can be minimized for the wrong reasons. For example, the values of the biases can be minimized by a model annual cycle that is too warm in the summer and too cold in the winter such that the average of the biases is small. The RMSE can be minimized if the dominant time scale of the model is the same as the dominant time scale of the data and they are in phase even if the amplitudes are significantly different. Thus, it is possible to achieve a "good" fit with respect to these statistics for a model that is significantly different from the data. These statistics do not appear sufficient to form an explicit, quantitative method of model tuning. Since it is apparent that  $R_*$  is not sufficient to eliminate  $Z_*$ , no attempt will be made to determine an improved set of model tuning statistics for this study. However, such a study will be necessary for future work involving real time upper ocean predictability.

Estimates for some parameters can be made from independent experiments and from theory. The dimensional equilibrium, or retreat, depth can be computed for the RSTAR model by setting  $P_* = W_*^2 = 0$  in Table 3 and substituting for the nondimensional variables from Table 2 to obtain a dimensional retreat depth. The resulting retreat depth is

$$h_r = \frac{m_3(p_2 - 1/3)L_0}{(p_2 + 2/3 + 2\Phi)}$$

which is the same as (2.8) in Garwood *et al.* (1985a). This indicates that  $p_2 \geq 1.3$  is required for  $h_r \geq 0$ . This establishes a lower bound on  $p_2$ , at least for the RSTAR model. Zeman and Tennekes (1975) summarized laboratory and atmospheric observations that indicate that  $p_2$  should be approximately 1/2. Garwood *et al.* (1985a) estimated  $m_3$  to be approximately seven based on measurements by Oakey and Elliott (1982). Values for  $p_3$  and  $p_1$  are less quantifiable. However,  $p_1$  must be less than one and  $p_3$  should be of order one. If  $p_3$  is significantly different from one, it most likely represents the effects of physical processes other than dissipation, and these processes should be modeled explicitly. The model does not seem to be very sensitive to variations of  $p_3$ . Preliminary tuning simulations indicated that varying  $p_3$  by  $\pm 0.1$  altered the annual average depth bias approximately  $\pm 2.5$  m about an annual average bias of approximately 0 m and varied the annual average temperature bias roughly  $\pm 0.05^\circ\text{C}$  about an annual average average bias of  $1.3^\circ\text{C}$ . A more complete study of the sensitivity of the ZSTAR model to variations of  $p_3$  might indicate what physical processes are being parameterized with  $Z_*$  and how the parameterization could be improved.

The models were tuned by changing  $m_3$  in the neighborhood of seven and allowing  $p_1$  to range between 0.1 and 0.5 until no extreme values of the monthly depth biases and RMSE's were obtained for any months of 1965 at OWS P. The resulting values for the model constants are summarized in Table 9.

TABLE 9  
MODEL CONSTANTS FOR OWS SIMULATIONS

	ZSTAR	RSTAR
$m_3$	10.0	5.0
$p_1$	0.3	0.3
$p_2$	0.5	0.5
$p_3$	1.0	*

## E. SEASONAL AND ANNUAL SCALE INTERCOMPARISONS OF MODELS

The problem of excessive wintertime deepening in early bulk models of the OPBL was discussed in Chapter II. Several solutions to this problem were reviewed. In particular, the rotationally enhanced dissipation parameterization of Garwood (1977) has been discussed in some detail and is a major component of the ZSTAR model being used in this study. To demonstrate the effectiveness of this dissipation parameterization, simulations of 1965 at OWS P with the HSTAR and ZSTAR models are compared using the final tuning constant values chosen for the ZSTAR model (Table 9). The ZSTAR and HSTAR simulations are similar in the summer (Figure 4.9). However, the HSTAR simulation is significantly deeper than the ZSTAR simulation or the observed mixed layer for days 0-130. Also the fall (days 275 to 325) deepening rate in the HSTAR simulation is too large. This results in a wintertime mixed layer depth that is approximately 75 m deeper than the observations after day 325. Only the existence of the halocline between the initial mixed layer depth and 150 m prevents the mixed layer from being even deeper (Figure 4.9). These simulations clearly demonstrate the need for some additional process or processes to reduce the efficiency of mixed layer deepening in the HSTAR model and allow a cyclic steady state for the OPBL depth.

The seasonal to annual time-scales effects of rotation stress and rotationally enhanced dissipation are investigated using annual simulations for 1961, 1965, 1966 and 1967 at OWS P and 1961 at OWS N. The RSTAR and ZSTAR models use the values of the tuning constants given in Table 9. The biases and RMSE's are calculated every 30 days and annually for all the simulations. The annual cycles of predicted 3-hourly MLD (Figures 4.10a - 4.14a) and MLT (Figures 4.10b - 4.14b) for each model are similar in gross features and comparable to the observed values. The monthly biases and RMSE's for the MLD and MLT (Table 10 - 14) also have some common characteristics on annual time scales. Both models tend to be too warm and shallow in the summer compared to the observations.

Spring transition, which is the usually abrupt transition from a deep wintertime regime to a shallow summertime regime, occurred around day 90 for OWS P, 1961, 1966 and 1967, about day 70 for OWS P, 1965 and OWS N, 1961, and near day 60 for OWS P, 1966. The models tend to be deeper and colder than the observations prior to the start of the spring transition. This may be due in part to the lack of surface salinity flux in the boundary conditions. The annual evaporation and precipitation may play a significant role in limiting the wintertime deepening at OWS P both late in

the year and prior to spring transition (Garzon, 1987). Also, the lack of accurate temperature and salinity profiles for initialization is important to model performance prior to spring transition. Before the construction of this seasonal thermocline, the model MLD is extremely sensitive to the strength of the pycnocline immediately below the mixed layer. Thus, the initial pycnocline is critical to the model performance during this period. After the spring transition, the model begins to build a seasonal thermocline.

Tables 10 through 14 give the monthly and the annually averaged temperature and depth biases for the ZSTAR and RSTAR models. For OWS P during 1967, the annual average surface heat flux of  $+0.8 \text{ W m}^{-2}$  (cooling) is the smallest of the five years. For both models (Table 10), the annual temperature biases and RMSE's are smaller than for any other year at OWS P. Both models have annual average temperature biases of less than  $1.0^\circ\text{C}$ . The ZSTAR bias was  $0.4^\circ\text{C}$  (positive bias means the model was warmer than the observations), and the RMSE was  $0.6^\circ\text{C}$ . For RSTAR, the bias was  $0.9^\circ\text{C}$  and the RMSE was  $1.0^\circ\text{C}$ . The values for RSTAR are about twice the ZSTAR values. However, the annual-average depth bias is significantly smaller for RSTAR and the annual-average depth RMSE's are comparable. The depth bias was  $-2.3 \text{ m}$  and the RMSE was  $33 \text{ m}$  for RSTAR; for ZSTAR, the bias was  $-15 \text{ m}$ , the RMSE was  $40 \text{ m}$ . A negative bias means the model was shallower than the observations. The ZSTAR model is warmer and shallower than the observations every month except October and November, which accounts for the larger depth bias. The RSTAR model achieves a better annual average bias by having a monthly average temperature that is too cold in the winter and fall and too warm in the summer. The maximum monthly temperature bias in the RSTAR model of  $3.0^\circ\text{C}$  in August is three times that of the ZSTAR model. Similarly, the RSTAR model mixed layer is too deep in the winter (maximum bias =  $32 \text{ m}$ ) and too shallow in the summer (maximum bias =  $-6 \text{ m}$ ).

The RMSE's for the RSTAR and ZSTAR models are comparable for all months except January, February and December 1967 (Table 10). In those three months, the ZSTAR model has significantly more diurnal and synoptic scale variability than either the data or the RSTAR model (Figure 4.13a). The diurnal to synoptic variability is similar for both models for days 120 to 240. For days 60 to 120 and 240 to 330, the RSTAR model has less diurnal to synoptic variability than the observations, whereas the ZSTAR model has more. Thus, the "comparable" RMSE values for the two

models are achieved quite differently. For RSTAR, the variability is less and for ZSTAR it is greater than in the observations.

The net annual surface heat flux is approximately zero in all three years, 1965-1967 at OWS P. The annual temperature bias and RMSE for the RSTAR model are similar for all three years. For the ZSTAR model, the annual temperature bias and RMSE is larger for 1965 and 1966 than for 1967. In 1965, the increase is due mainly to larger values early in the year, whereas in 1966 the increase is the result of larger differences between the model and the observations late in the year. Thus, it is possible to obtain similar values for the annual biases and RMSE's with quite different monthly results.

For 1961 at both ocean weather stations, the annual average surface heat flux is larger, by an order of magnitude, than in the other three years. At OWS P, there was an annual average surface warming of  $25 \text{ W m}^{-2}$ . At OWS N, there is an annual average surface cooling of  $17 \text{ W m}^{-2}$ . The annual average temperature and depth biases for both the RSTAR and ZSTAR simulations are two to three times larger at OWS P for 1961 than they were for the other three years. Both models are shallower and warmer than the observations. For ZSTAR, the annual average temperature bias is  $1.8^\circ\text{C}$ , which is three times the values for 1965 through 1967. The depth bias is  $-9.4 \text{ m}$ , which is similar to the other years. Both the annual average temperature bias for RSTAR of  $3.2^\circ\text{C}$  and the depth bias of  $-7.5 \text{ m}$  are larger than the values from other years. These results are consistent with the large annual average surface warming for 1961 at OWS P.

The biases and RMSE's for OWS N are almost identical for both models and are smaller than at OWS P for 1961 and comparable to OWS P for 1965-1967. The annual average temperature bias is  $-0.5^\circ\text{C}$  for both models and the model depth is  $5 \text{ m}$  shallower than the observations for ZSTAR and  $4.3 \text{ m}$  shallower for RSTAR. The annual average surface stress at OWS N was approximately  $0.03 \text{ N m}^{-2}$ , compared with an average of about  $0.1 \text{ N m}^{-2}$  for the four years at OWS P (Table 7). At OWS N, the annual average north-south stress is a factor of five smaller than the east-west stress. Thus, there is a relatively large annual average surface cooling with light easterly winds at OWS N compared to an approximately zero net surface heating and moderate to strong westerlies at OWS P. This implies that  $R_*$  and  $Z_*$  will be smaller at OWS N due to the small surface stress and due to the relatively shallow mixed layer. The winter maximum mixed layer is  $O(120 \text{ m})$  at OWS N compared to  $(150 \text{ m})$  at OWS P. Also



$H_*$  will be relatively large and negative at OWS N. Thus, the relative effects of  $Z_*$  and  $R_*$  at OWS N will be small and mixed layer deepening will mainly be driven by the surface buoyancy flux. The similar results for the two models indicates that the annual simulations are not very sensitive to  $Z_*$  and  $R_*$  at OWS N for 1961.

The result that the simulated depths are too shallow on average may indicate that mixing due to surface buoyancy flux is underestimated in the models. The same result could be due to tuning the dissipation to be too large to compensate for too much mixing by the surface stress. The simulations are colder than the data due to the large surface cooling being distributed over a too shallow layer. The effects due to latitudinal variations in  $R_*$  are obscured by the variations caused by the significantly different surface buoyancy and momentum fluxes at the two ocean weather stations.

The RSTAR model is generally warmer and shallower in the summer and colder and deeper in the winter compared to the ZSTAR model and the observations at OWS P. This is characteristic of an incomplete parameterization of dissipation (Gaspar, 1986). At the same time, the ZSTAR model has more diurnal to synoptic scale variability than the RSTAR model or the observations (for these values of the tuning constants, Table 9). This can be the result of too much dissipation such that the mixed layer retreats too much for slight variations in wind speed. In general, the ZSTAR model simulated the data better than the RSTAR model. However, the ZSTAR model rarely achieved a good fit to the data for all seasons of the year. Thus, a better annual fit had to be achieved at the expense of one or more seasonal periods.

Based on the results of the synoptic studies, the results from tuning the parameters, and the results discussed above, the conclusion is that a reduction of mixing efficiency is needed, at least for midlatitude mixed layers. The rotation stress is not sufficient to prevent excessive mixed layer deepening in regions of westerly wind at midlatitudes. However, the results of Garwood *et al.* (1985b) indicate that  $R_*$  may be sufficient to prevent excessive deepening in equatorial regions where  $R_*$  approaches a maximum and  $Z_*$  approaches zero. However, over much of the tropics the winds are easterly and  $R_*$  would enhance mixing. The synoptic studies discussed above indicate that for westerly wind regions  $R_*$  can reduce the wintertime mixed layer depth 10% to 15%. Thus, a smaller value of  $Z_*$  may be required in a model which includes both the rotation stress and the rotationally enhanced dissipation. A smaller value of  $Z_*$  may reduce some of the problems in the ZSTAR simulations that were discussed above. An alternative solution is find a process that prevents excessive mixing without increasing the anisotropy of the TKE budget.

TABLE 10  
COMPARISON OF MODELS AT OWS P, 1967

	ZSTAR				RSTAR			
	T <sub>bias</sub>	T <sub>rmse</sub>	h <sub>bias</sub>	h <sub>rmse</sub>	T <sub>bias</sub>	T <sub>rmse</sub>	h <sub>bias</sub>	h <sub>rmse</sub>
Jan	0.1	0.2	-24.4	47.8	0.0	0.2	31.6	38.4
Feb	0.1	0.2	-61.8	70.1	0.0	0.2	7.6	34.7
Mar	-0.1	0.3	-43.6	74.0	-0.1	0.3	-4.3	74.5
Apr	-0.0	0.3	-40.2	61.3	-0.1	0.3	-31.8	60.5
May	0.1	0.3	-3.1	11.9	0.1	0.2	-4.6	12.4
Jun	0.3	0.5	-2.3	6.0	0.9	1.0	-4.6	7.0
Jul	0.2	0.5	-1.9	7.0	1.4	1.5	-5.0	8.2
Aug	1.0	1.2	-0.7	5.7	2.9	3.0	-2.7	5.9
Sep	0.5	0.7	-3.3	13.9	1.8	1.9	-6.4	13.8
Oct	0.4	0.6	4.4	15.9	1.2	1.3	1.2	13.6
Nov	0.8	1.0	9.9	27.3	1.0	1.2	13.0	26.7
Dec	1.1	1.2	-41.9	53.6	1.0	1.0	-7.3	22.9
Avg	0.4	0.6	-15.2	39.6	0.9	1.3	-2.3	33.2

TABLE 11  
COMPARISON OF MODELS AT OWS P. 1965

	ZSTAR				RSTAR			
	T <sub>bias</sub>	T <sub>rmse</sub>	h <sub>bias</sub>	h <sub>rmse</sub>	T <sub>bias</sub>	T <sub>rmse</sub>	h <sub>bias</sub>	h <sub>rmse</sub>
Jan	1.3	1.3	-29.3	56.3	1.1	1.1	32.9	65.3
Feb	1.3	1.3	-17.3	57.3	1.2	1.2	42.9	66.3
Mar	0.6	0.8	-8.5	27.3	0.4	0.6	-3.9	37.3
Apr	0.5	0.6	-14.0	32.0	0.2	0.4	-3.9	38.9
May	0.6	0.6	-7.2	20.4	0.5	0.4	-6.1	29.9
Jun	0.9	0.8	-4.3	10.4	1.0	1.1	-4.1	11.9
Jul	1.2	1.3	-1.8	7.8	1.9	2.0	-4.1	6.9
Aug	1.1	1.2	-4.3	9.9	2.0	2.0	-6.6	10.9
Sep	0.8	0.9	-1.2	7.8	1.9	1.9	-6.6	10.9
Oct	0.3	0.5	-0.9	14.9	1.0	1.1	-4.1	11.9
Nov	-0.2	0.4	-1.2	23.1	-0.3	0.5	-4.1	20.9
Dec	0.2	0.4	-7.6	25.4	-0.2	0.4	-4.1	20.9
Avg	0.7	0.9	-7.2	27.4	0.9	1.3	-4.6	33.6

TABLE 12  
COMPARISON OF MODELS AT OWS P. 1966

	ZSTAR				RSTAR			
	T <sub>bias</sub>	T <sub>rmse</sub>	h <sub>bias</sub>	h <sub>rmse</sub>	T <sub>bias</sub>	T <sub>rmse</sub>	h <sub>bias</sub>	h <sub>rmse</sub>
Jan	0.2	0.2	-43.9	59.8	0.1	0.1	10.9	63.8
Feb	0.5	0.5	-0.9	53.9	0.1	0.1	4.9	63.8
Mar	0.5	0.5	-35.3	61.1	0.1	0.1	4.9	63.8
Apr	-0.5	0.3	-19.3	33.8	-0.3	0.4	-10.9	37.8
May	-0.2	0.3	-13.5	21.8	-0.2	0.4	-13.9	26.8
Jun	0.6	0.8	-3.9	8.9	1.0	1.1	-4.9	10.8
Jul	1.3	1.4	-4.0	6.9	2.0	2.0	-4.9	10.8
Aug	1.5	1.8	-4.0	9.9	3.0	3.0	-4.9	10.8
Sep	1.6	1.6	-2.3	10.8	3.0	3.0	-4.9	10.8
Oct	1.2	1.5	0.0	19.4	2.1	2.1	-4.9	11.8
Nov	1.1	1.5	-23.1	21.1	1.4	1.4	-4.9	20.8
Dec	0.4	0.5	-23.5	21.0	1.2	1.2	-4.9	20.8
Avg	0.7	1.0	-14.4	35.9	1.1	1.8	-4.4	31.8

TABLE 13  
COMPARISON MODELS AT OWS P, 1961

	ZSTAR				RSTAR			
	T <sub>bias</sub>	T <sub>rmse</sub>	h <sub>bias</sub>	h <sub>rmse</sub>	T <sub>bias</sub>	T <sub>rmse</sub>	h <sub>bias</sub>	h <sub>rmse</sub>
Jan	0.7	0.8	6.5	56.1	0.6	0.7	46.6	82.4
Feb	1.0	1.0	-20.9	58.0	0.9	0.9	30.9	65.7
Mar	0.8	0.9	-88.4	107.9	0.8	0.8	-51.6	91.9
Apr	0.6	0.7	-14.9	35.0	0.5	0.6	-8.3	32.7
May	0.8	0.8	-17.7	29.8	0.7	0.7	-17.4	28.9
Jun	1.1	1.2	-9.6	17.6	1.5	1.6	-11.8	18.2
Jul	2.0	2.0	-4.1	7.8	3.5	3.5	-5.3	8.4
Aug	2.4	2.4	-5.3	9.2	4.8	4.8	-8.4	11.2
Sep	2.1	2.1	-7.5	14.0	4.7	4.7	-11.9	16.0
Oct	1.1	1.2	-2.3	21.2	2.5	2.6	-9.3	20.3
Nov	0.8	1.0	-0.7	23.9	1.3	1.4	-5.0	18.4
Dec	1.5	1.5	-4.9	32.4	1.4	1.5	14.1	30.7
Avg	1.8	1.9	-9.4	28.6	3.2	3.7	-7.5	29.0

TABLE 14  
COMPARISON OF MODELS AT OWS N, 1961

	ZSTAR				RSTAR			
	T <sub>bias</sub>	T <sub>rmse</sub>	h <sub>bias</sub>	h <sub>rmse</sub>	T <sub>bias</sub>	T <sub>rmse</sub>	h <sub>bias</sub>	h <sub>rmse</sub>
Jan	-0.0	0.6	-0.7	59.7	-0.0	0.6	3.9	62.0
Feb	-0.2	0.4	-3.9	45.2	-0.2	0.4	-0.7	46.4
Mar	-0.3	0.5	-4.3	42.1	-0.3	0.5	-2.8	47.5
Apr	-0.6	0.8	-29.3	53.2	-0.6	0.8	-30.2	53.4
May	-0.7	0.9	-19.4	33.2	-0.7	0.8	-20.3	33.7
Jun	-0.4	0.6	-1.7	9.8	-0.3	0.9	-0.1	9.7
Jul	-0.8	0.9	-2.3	12.8	-0.7	0.9	-4.1	13.6
Aug	-0.1	0.5	-5.3	13.4	-0.0	0.5	-6.5	14.0
Sep	-1.2	1.4	4.4	21.5	-1.2	1.4	3.1	21.4
Oct	-0.5	0.8	-14.2	29.0	-0.2	0.7	-13.6	29.3
Nov	-0.8	0.9	-11.0	35.6	-0.8	0.9	-9.7	35.2
Dec	-0.6	0.6	24.1	56.7	-0.7	0.7	32.5	60.3
Avg	-0.5	0.8	-5.0	36.1	-0.5	0.8	-4.3	37.5

## V. SUMMARY AND RECOMMENDATIONS

This work introduced rotation stress, a mechanism by which planetary rotation and wind direction affect geophysical turbulent boundary layers. Rotation stress is the interaction of the northward component of planetary rotation and the east-west Reynolds stress. This interaction causes a redistribution of turbulent kinetic energy (TKE) from the east-west to the vertical component for easterly winds, or from the vertical to the east-west component for westerly winds. This exchange of TKE between the components results from inertial motions of the turbulence in the x-z plane.

The effects of rotation stress were compared with those that result from the rotational enhancement to the TKE dissipation that was proposed by Garwood (1977). There are two major results. First, the TKE distribution is more isotropic and in better agreement with laboratory results when rotation stress is included in a TKE model than for the model that includes rotationally enhanced dissipation or for the model with no planetary rotation effects. Secondly, rotation stress alters the frequency and magnitude of diurnal to synoptic scale mixing events during late winter through early spring at mid latitudes.

The ratio of the vertical to the total TKE is a measure of the isotropy of the TKE distribution between the vertical and the horizontal components. The ratio would be 0.33 if the TKE distribution was isotropic. Laboratory measurements of wall-bounded, neutrally stratified shear flows indicate that the ratio is 0.16 to 0.3. For stably stratified shear flows such as the upper ocean mixed layer, the ratio would be smaller. For late winter to early spring at OWS P, which is predominately forced by surface shear stress, typical values of the ratio of vertical to total TKE are less than 0.03 for the rotationally enhanced dissipation model compared to an average of 0.1 for the rotation stress model. The nondimensional studies show that this ratio can be more variable as a function of rotation stress than as a function of rotationally enhanced dissipation since rotation stress can cause a transfer of energy between the horizontal and vertical TKE components.

Both the equilibrium depth and the entrainment rate are functions of rotation stress. With rotation stress, diurnal shallowing events occur more frequently for

westerly wind regimes and the equilibrium depth is 10 to 40% shallower than for the model which neglects planetary rotation. On synoptic time scales, the mixed layer simulated with the rotation stress model typically deepens 10% more for easterly winds or about 10% to 15% less for westerly winds than it is for the model that neglects planetary rotation.

For late winter to early spring, typical values of the entrainment rate from the simulations with rotation stress were twice as large at OWS N and four times as large at OWS P as for the simulations with the rotationally enhanced dissipation. As a result, annual simulations using the rotationally enhanced dissipation had shallower average winter mixed layer depths than those for rotation stress. These shallower winter mixed layer depths better fit the seasonal trend of the OWS observations. However, the functional form of the entrainment rate as a function of rotation stress is consistent with the need for decreased mixing efficiency for deep mixed layers and large values of the surface stress. This is not the case for the rotational enhanced dissipation rate. The entrainment rate decreases to zero with increasing rotation stress, whereas it approaches an asymptotic value greater than zero as the rotationally enhancement to the dissipation increases. Therefore, the rotation stress could prevent mixed layer deepening for sufficiently large values of westerly wind or deep mixed layers. Conversely, the entrainment rate never goes to zero for the rotationally enhanced dissipation case.

At midlatitudes, the rotation stress does not consistently prevent excessively deep wintertime mixed layers. Some additional mechanism is needed to reduce mixing efficiency for deep mixed layers and/or large surface stresses at mid latitudes. Enhanced dissipation does prevent excessively deep wintertime mixed layer depths; however, the TKE distribution then becomes very anisotropic. The degree of anisotropy appears to be excessive based on laboratory measurements, but there are no oceanic measurements to confirm this.

The temporal and spatial resolution and the precision of the OWS data sets used in this study were not sufficient to confirm the increased frequency and magnitude of diurnal to synoptic scale shallowing and deepening events predicted by the rotation stress model. Data from experiments such as the Storm Transfer and Response Experiment (STREX) and the Mixed Layer Dynamics Experiment (MILDEX) may be sufficiently accurate with enough temporal resolution to test the effects of rotation stress. However, these data sets may not contain the contrasting east-west wind stress

events, which is a requirement to test the rotation stress effects. It was hoped that the OWS station data sets would contain sufficient events to confirm the effects of rotation stress. Also the OWS data provided the opportunity to study the seasonal variability of the effects of planetary rotation on the upper ocean. The study does indicate that the planetary rotation has the greatest effects for winter and early spring mixed layers. The impact of planetary rotation is the smallest for summer mixed layers.

The greatest differences among the simulations in this study appear in the TKE budgets calculated by the models. The variations in the mixed layer temperature are relatively small due to the large heat capacity of water. Hence, the differences among the predicted and observed temperatures are small. The differences in the mixed layer depths predicted by the models are more obvious. However, the models can be tuned to predict similar mixed layer depths even though the TKE budgets of the models are quite different. Also the differences between the turbulent boundary layer depth predicted by the models and the depth of the "well-mixed" layer defined by the temperature observations obscure the comparison between the simulations and the observations. The turbulent boundary layer depth and the depth of the isothermal layer in the upper ocean do not always coincide, and the OWS data are not always sufficient to define the isothermal layer accurately or consistently.

This study has shown that substantial variations exist in the isotropy of the TKE distribution predicted by different TKE models of the upper ocean. The results of this study suggest that parameterizations of various processes are not complete. In particular, the parameterizations for dissipation, shear stress and the pressure-rate of strain require further theoretical and observational work. The importance of rotation stress has been indicated by this study, but the data were insufficient to verify completely the effects of rotation stress.

The results of this research focus attention on specific observational requirements that need to be met in order to properly evaluate and improve turbulence models for applications to the oceanic environment. Direct measurements of TKE budget in the upper ocean are required to test the current hypotheses of ocean planetary boundary layer dynamics. A field experiment that focuses on the upper ocean turbulence from the sea surface to the transient thermocline is necessary to provide this data. The first phase of such an idealized program should concentrate on vertical exchanges and budgets in an open ocean area with relatively small but well-observed horizontal variability. Measurements must include the surface heat, salt and vector momentum

fluxes. Estimates from bulk formulas would probably not be sufficiently accurate. The mean temperature, salinity and velocity profiles from the surface through the transient thermocline must also be measured simultaneously. The vertical and temporal variations and the vertical shear of the normal Reynolds stresses (TKE components) are the turbulence quantities to be measured in the first phase. The vertical shear of the horizontal and vertical turbulent velocities have previously been measured to estimate dissipation. The second phase would extend the first phase measurements to include the vertical and temporal variations of the shearing Reynolds stresses and the vertical buoyancy flux through the mixed layer and the entrainment zone. The third phases would begin to incorporate three-dimensional effects and the interactions between the turbulence and aspects of the mean flow such as upwelling and internal waves.

Practical forecasts of mixed layer temperature and depth can not be improved until the turbulence in the OPBL is better understood and better parameterized in the models of the OPBL. This impacts both short-term forecasts of the upper ocean that are important for improved acoustical forecasts and weather forecasts required for naval operations and climate forecasts of the ocean-atmosphere system.



APPENDIX  
FIGURES

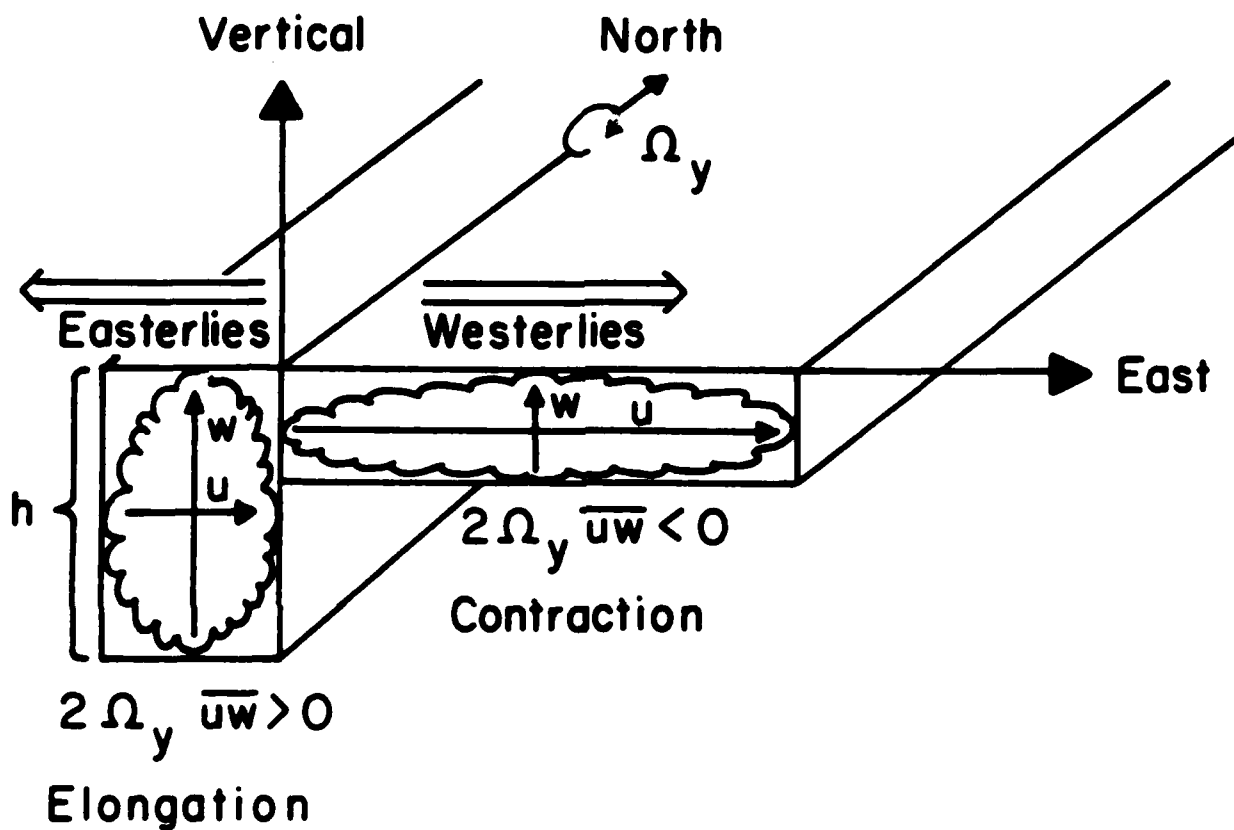


Figure 1.1. The vertical elongation or contraction of turbulent eddies in the eastward-vertical plane by the northward component of planetary vorticity.

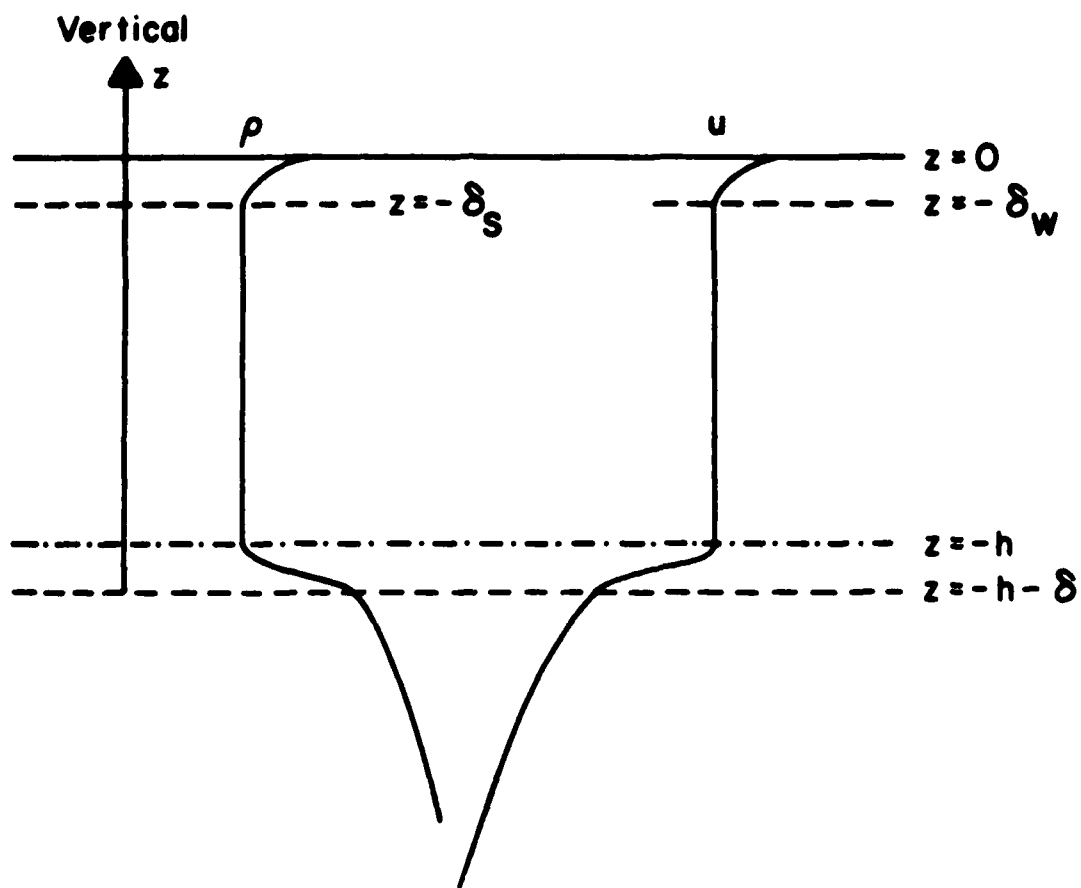


Figure 1.2. Schematic of mean density and velocity profiles in the upper ocean,  $\delta$  is the thickness of the entrainment zone,  $\delta_w$  is the depth of the wind-wave zone, and  $\delta_s$  is the solar radiation compensation depth.

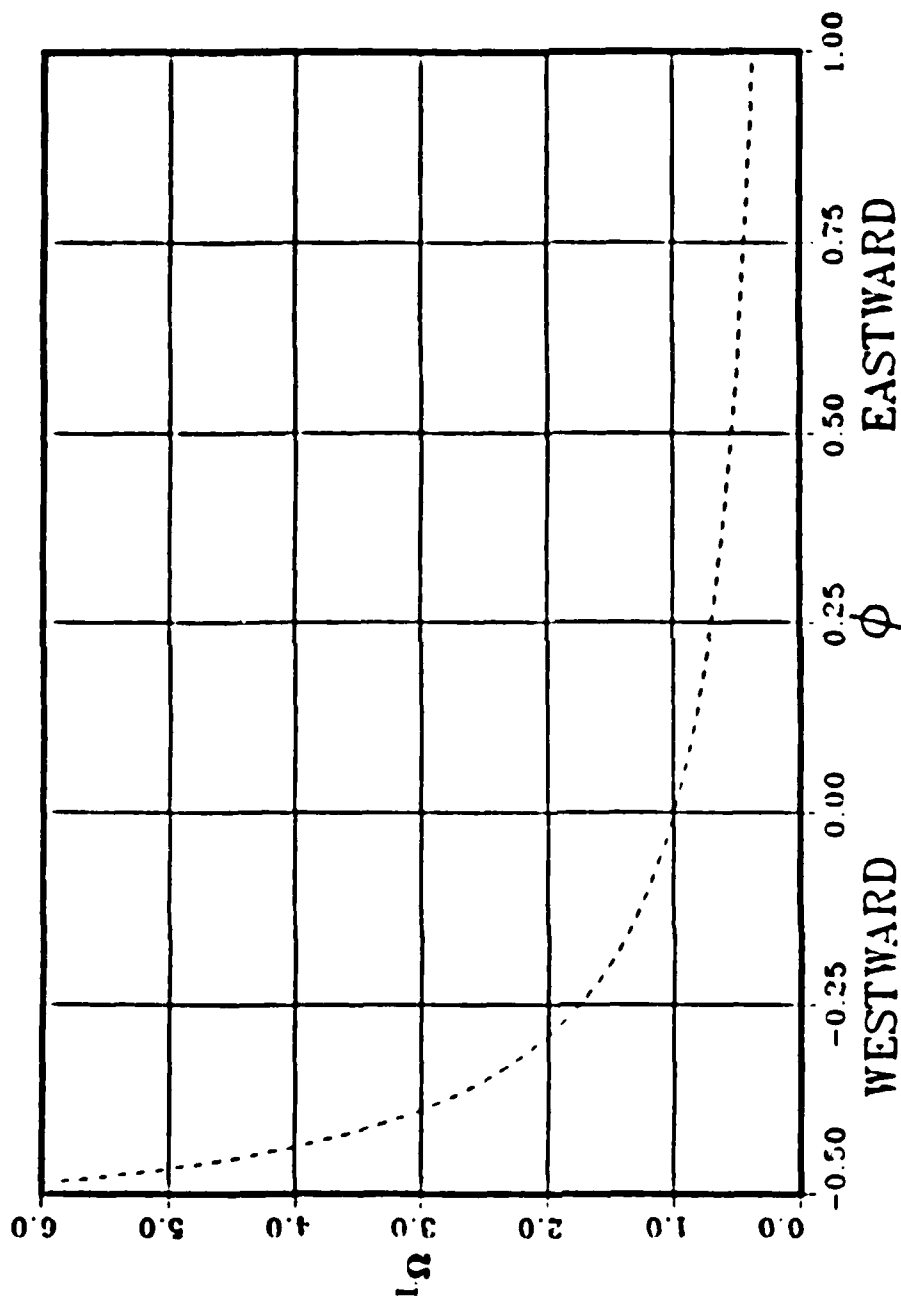


Figure 1.3. The dependence of  $I\Omega$ , the nondimensional equilibrium depth, on the ratio of rotation stress to surface buoyancy flux ( $\Phi$ ), after Garwood *et al.* (1985a).

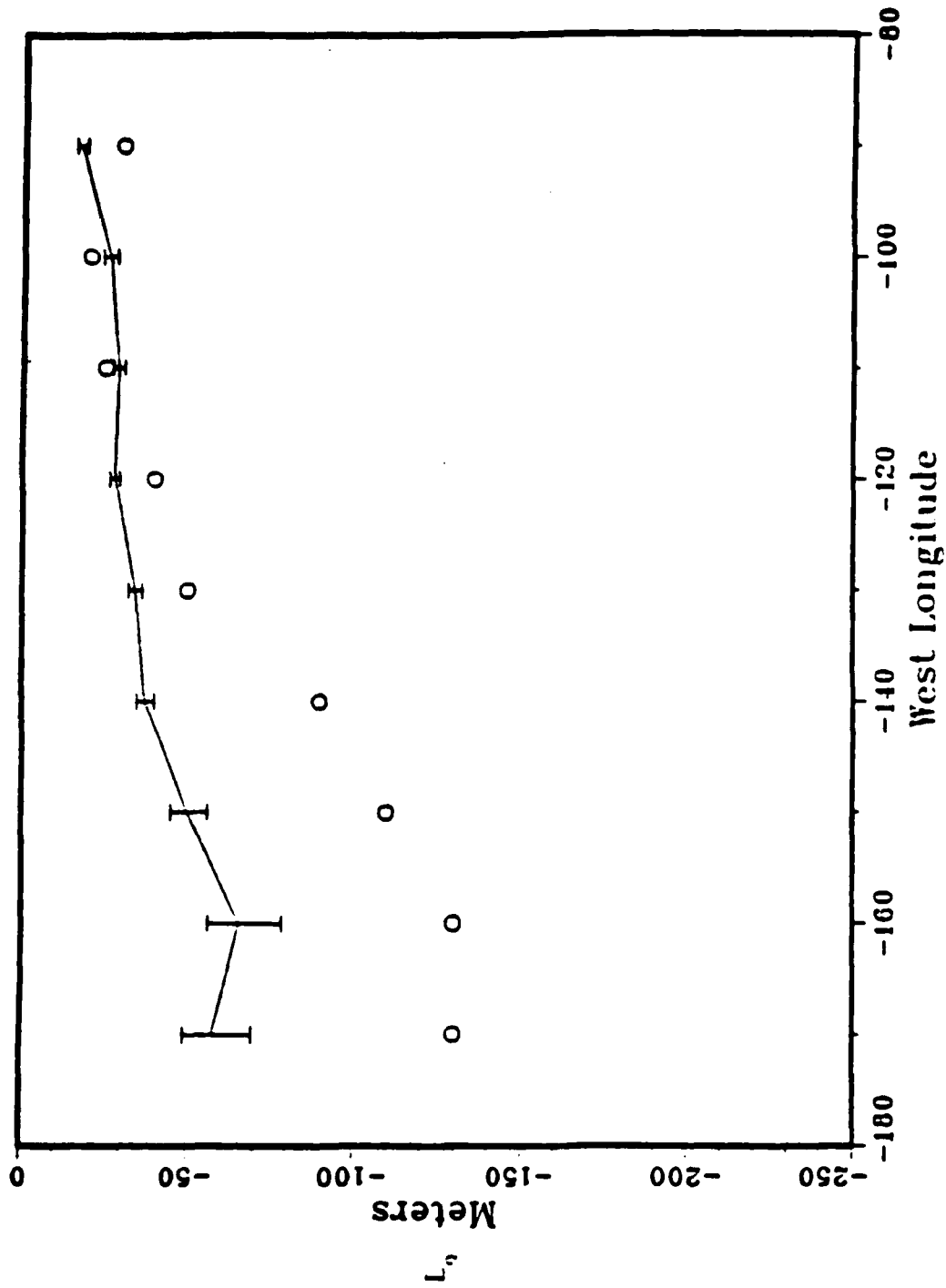


Figure 2.1. The dependence of the Obukhov depth ( $L_o$ ) on longitude at the equator. Circles approximate the climatological mixed layer depth. The vertical bars are for the variations in  $h$  due to fluctuations of  $\pm 3 \text{ W m}^{-2}$  in the surface heat flux, from Garwood *et al.* (1985b).

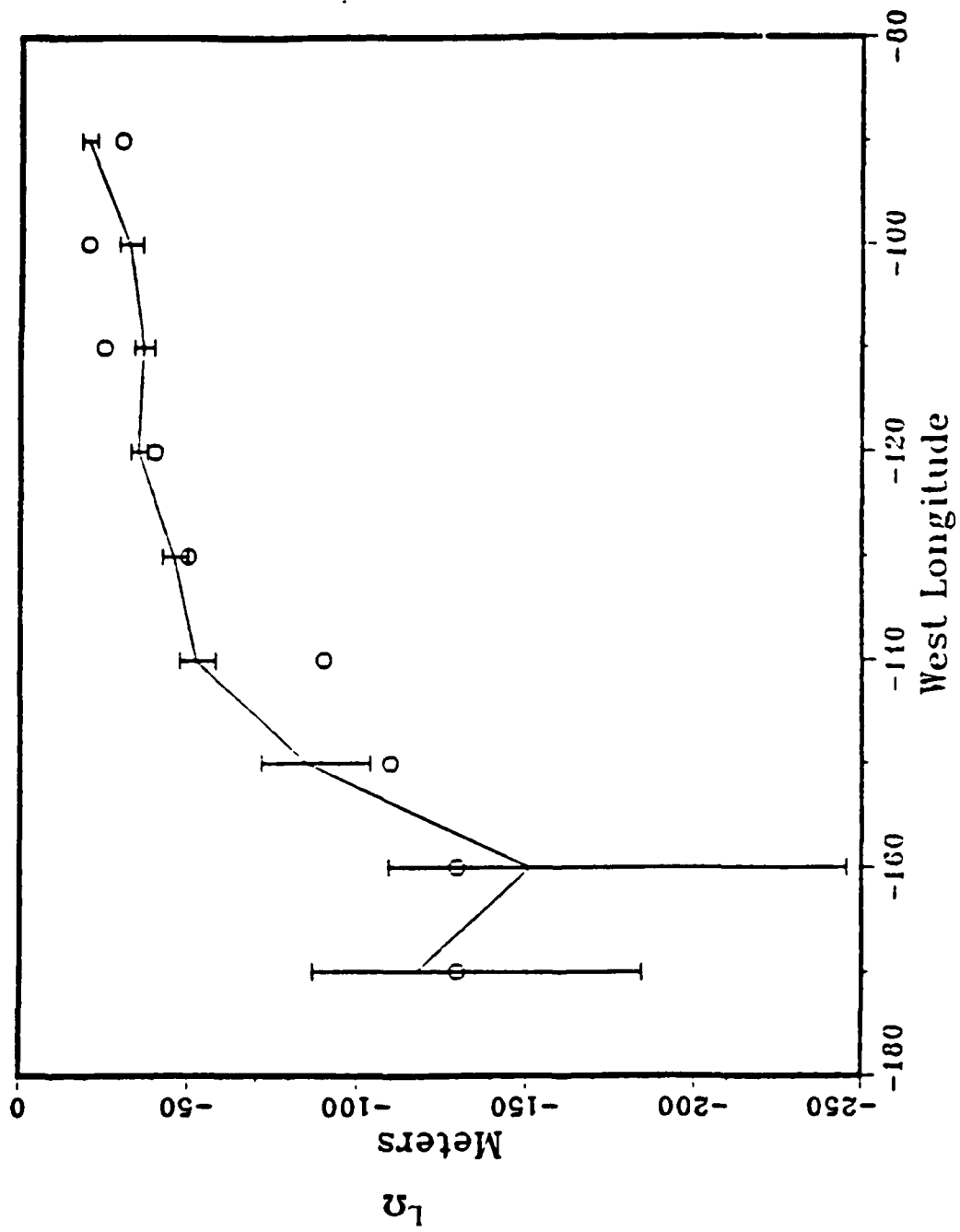


Figure 2.2. As in Figure 2.1, except the equilibrium depth is  $L_2$ , after Garwood *et al.* (1985a).

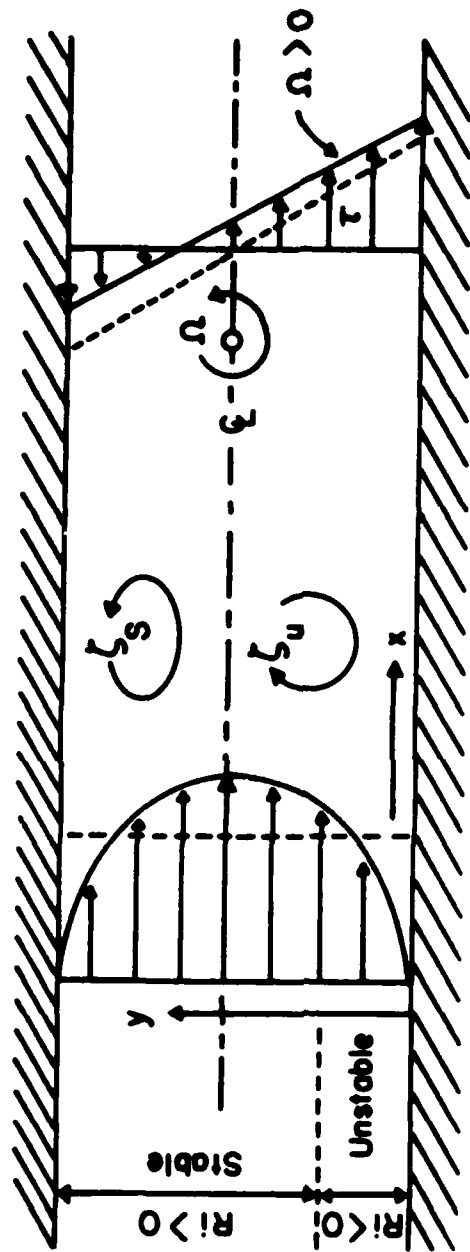


Figure 2.3. Schematic of the rotating channel of Johnston *et al.* (1972) showing the mean velocity and total shear stress profiles for a fully developed two-dimensional flow in a rotating channel.

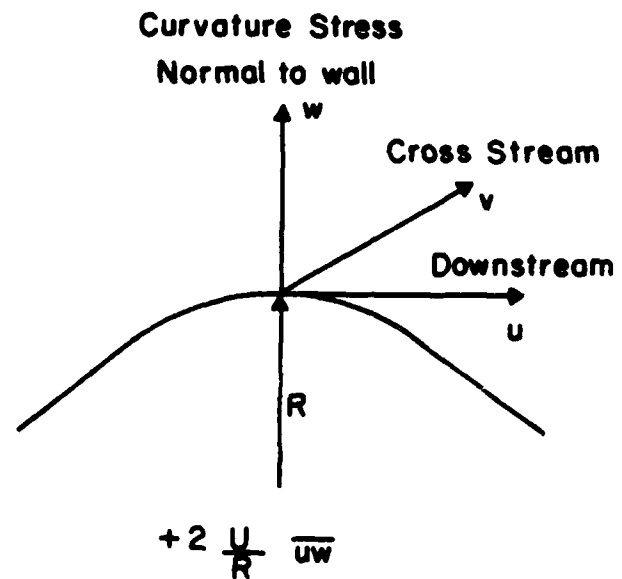
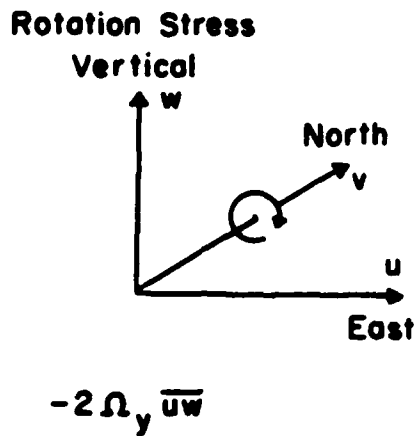


Figure 2.4. Rotation stress reduces the vertical TKE for  $-uw > 0$  (westerlies). Similarly, curvature stress reduces the TKE normal to the wall for convex curvature ( $R > 0$ , as shown).

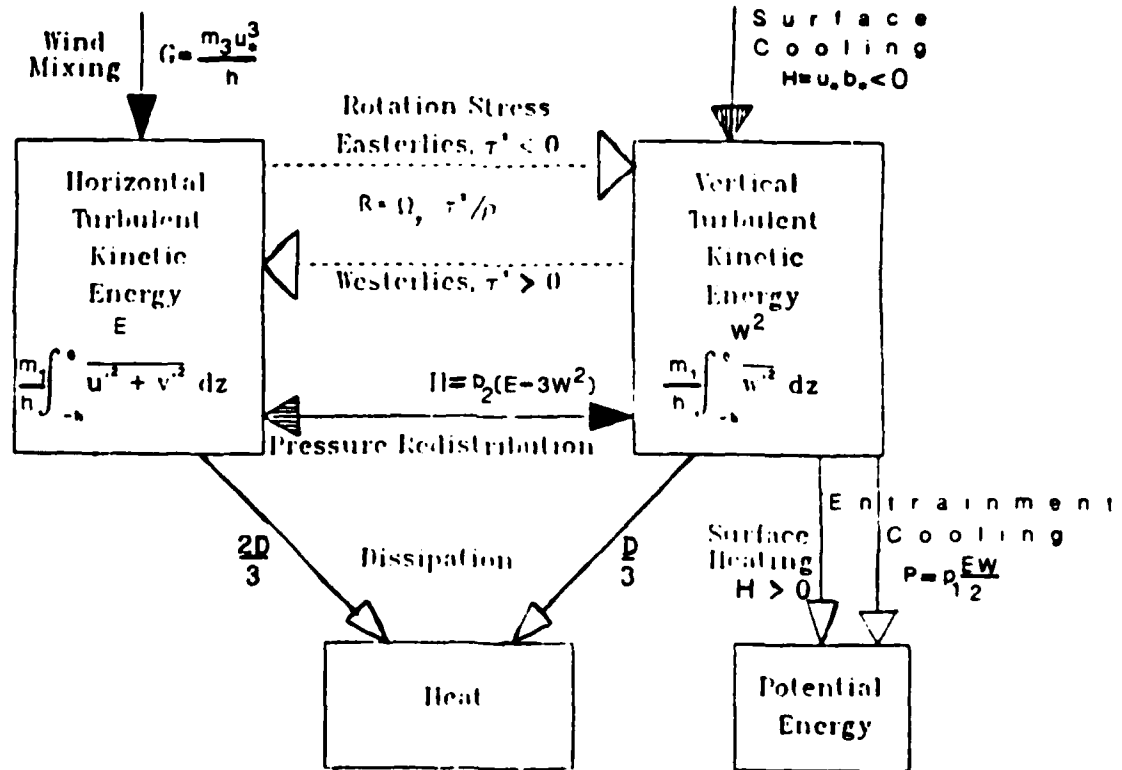


Figure 3.1. Schematic of TKE budget including entrainment.



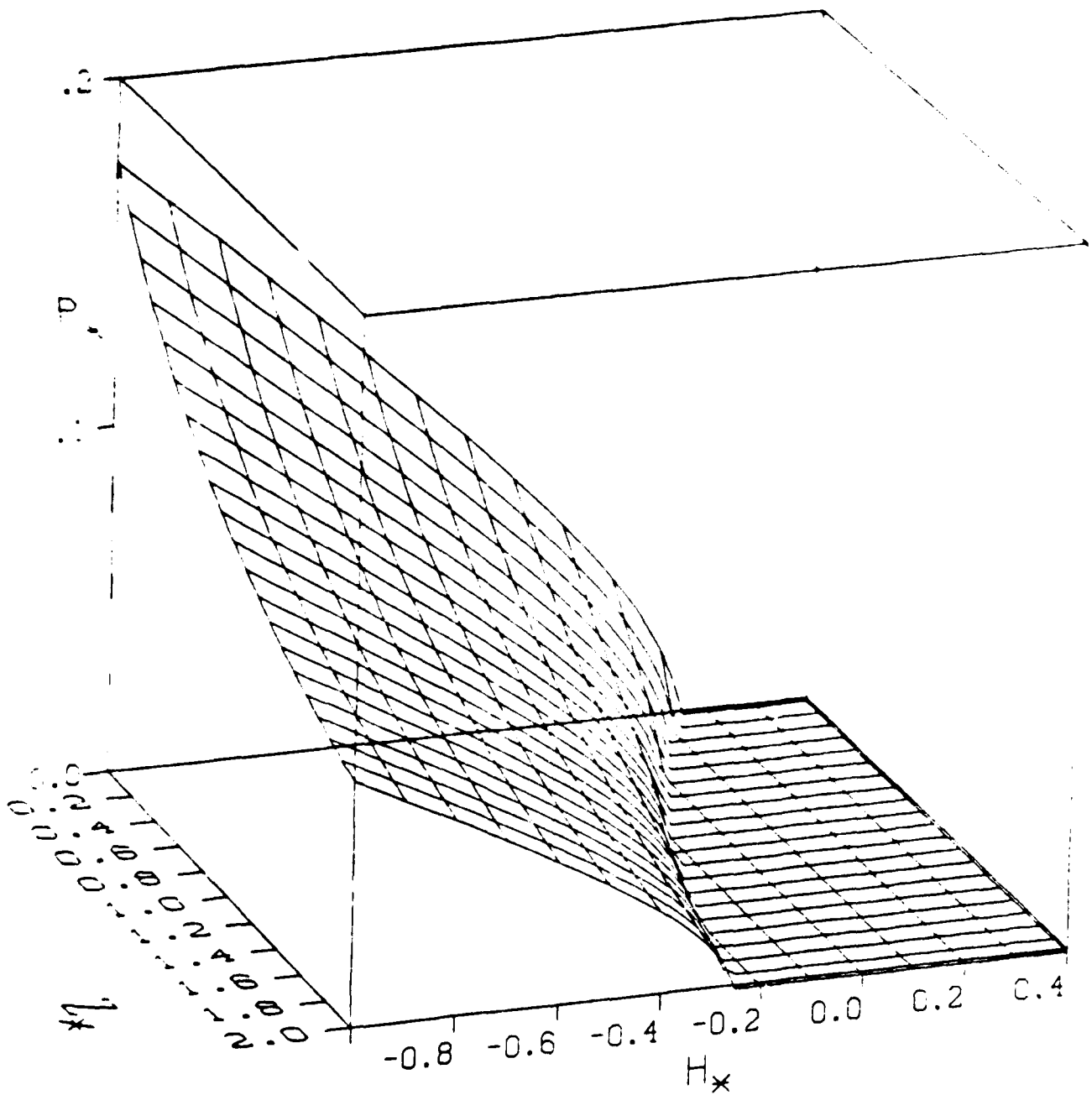


Figure 3.2a.  $P(H_*, Z_*)$ , nondimensional entrainment rate for the ZSTAR model.

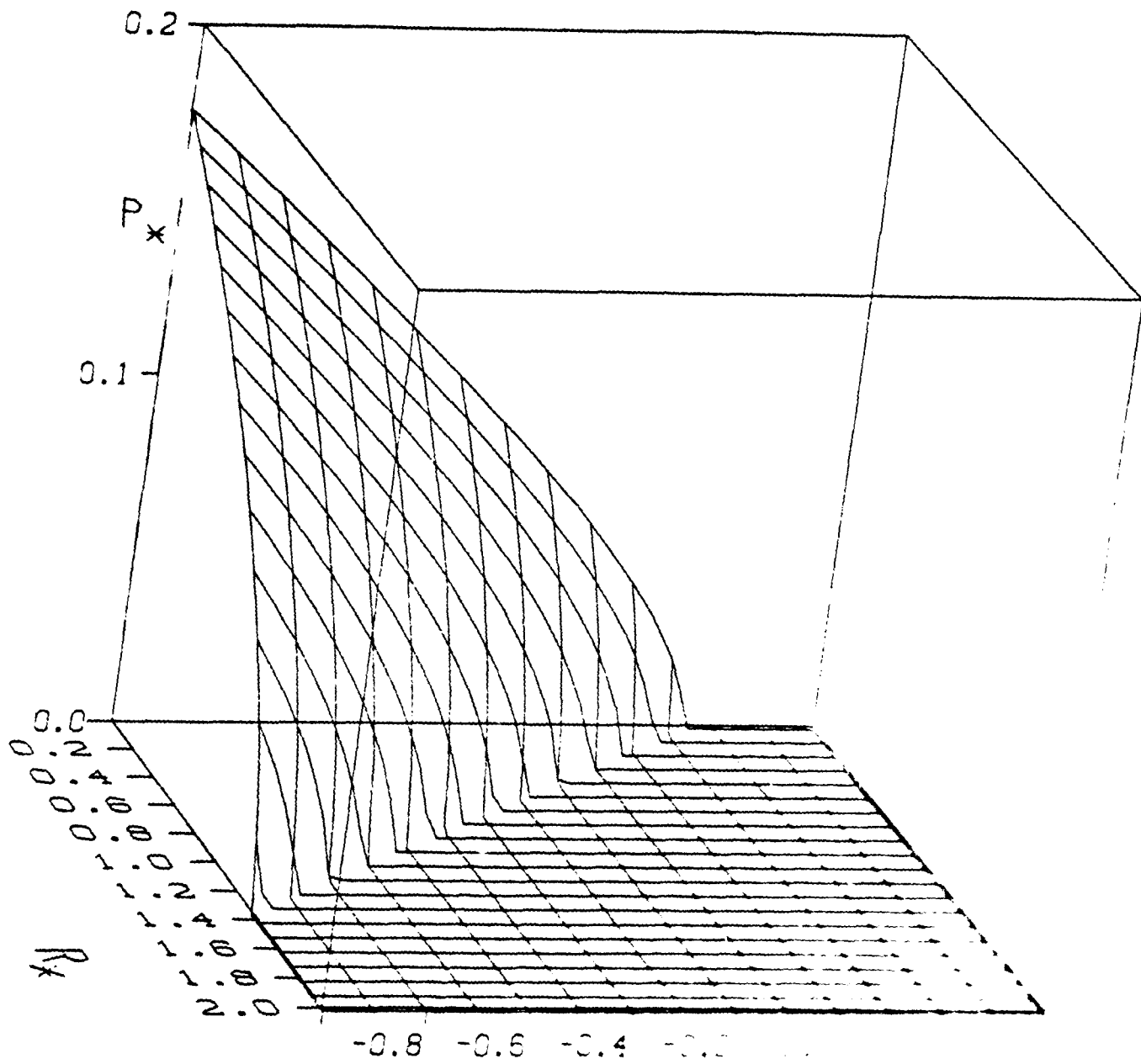


Figure 3.2b.  $P_x(H_x, R_x)$ , nondimensional entrainment  
 Positive  $R_x$  is for westerly winds

AD-A181 991

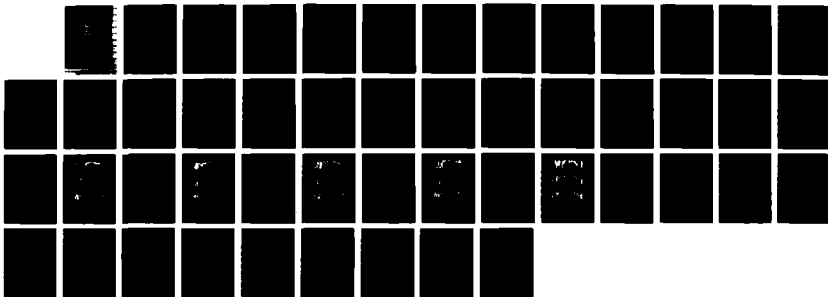
IMPORTANCE OF ROTATION SHEAR STRESS FOR ENTRAINMENT IN  
THE OCEAN MIXED LAYER(U) NAVAL POSTGRADUATE SCHOOL  
MONTEREY CA P C GALLACHER JUN 87

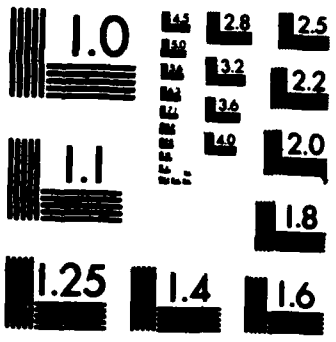
2/2

UNCLASSIFIED

F/G 8/3

NL





MICROCOPY RESOLUTION TEST CHART  
NATIONAL BUREAU OF STANDARDS-1963-A

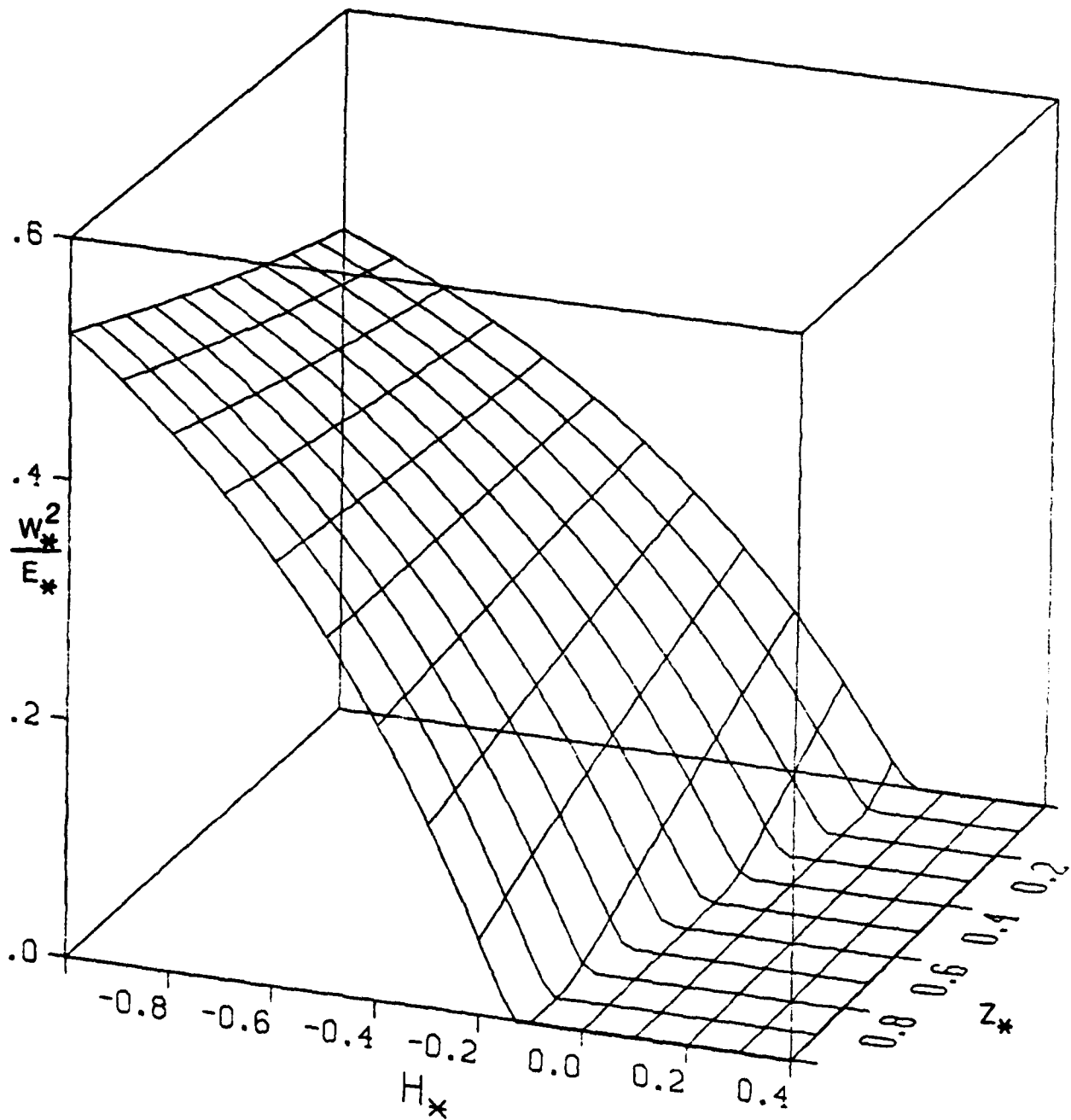


Figure 3.3a  $W_*^2/E_*(H_*, Z_*)$  for ZSTAR.

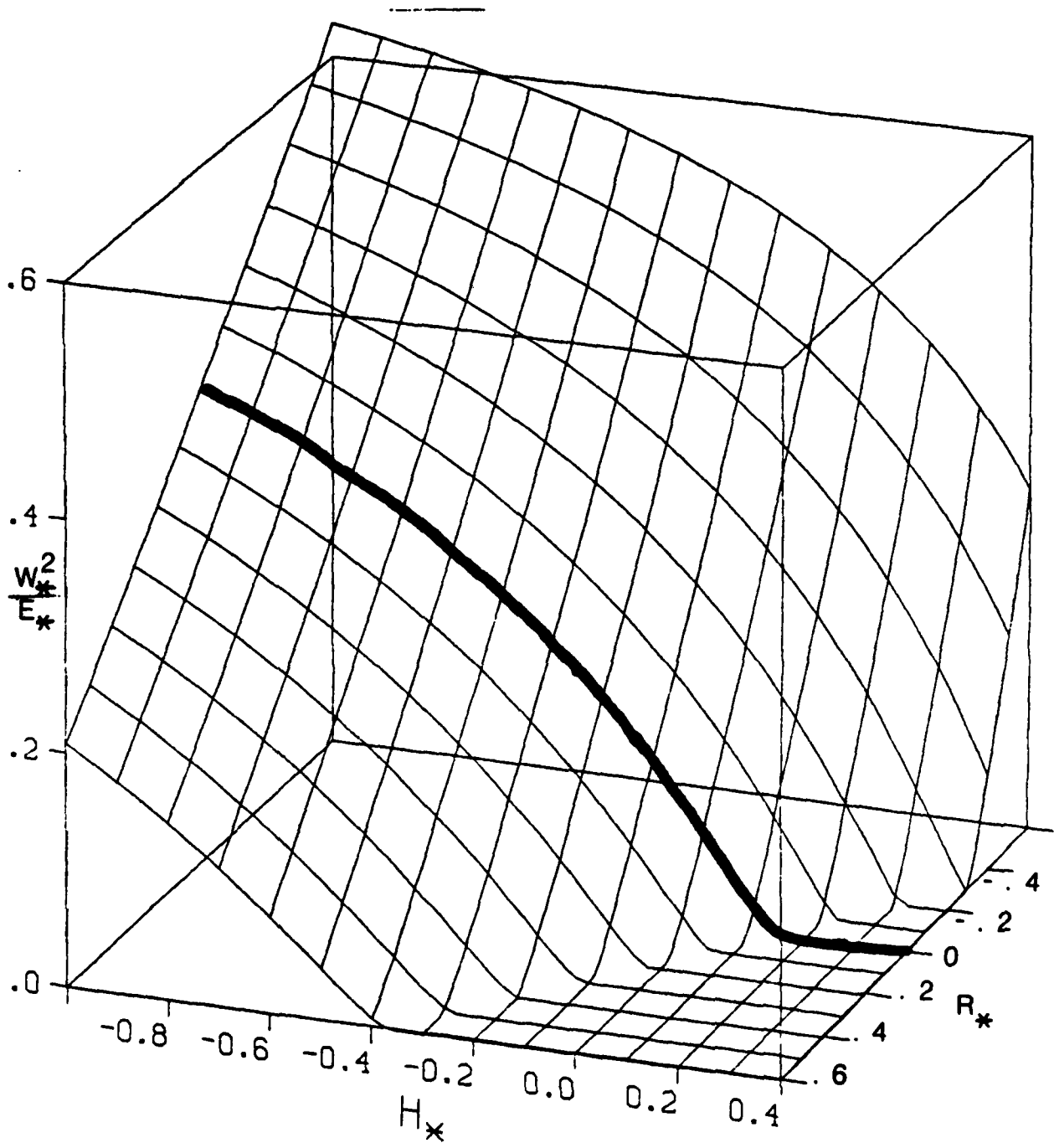


Figure 3.3b.  $W_*^2/E_*$ , ratio of vertical to total nondimensional TKE for the RSTAR model. Positive  $R_*$  is for westerly winds.

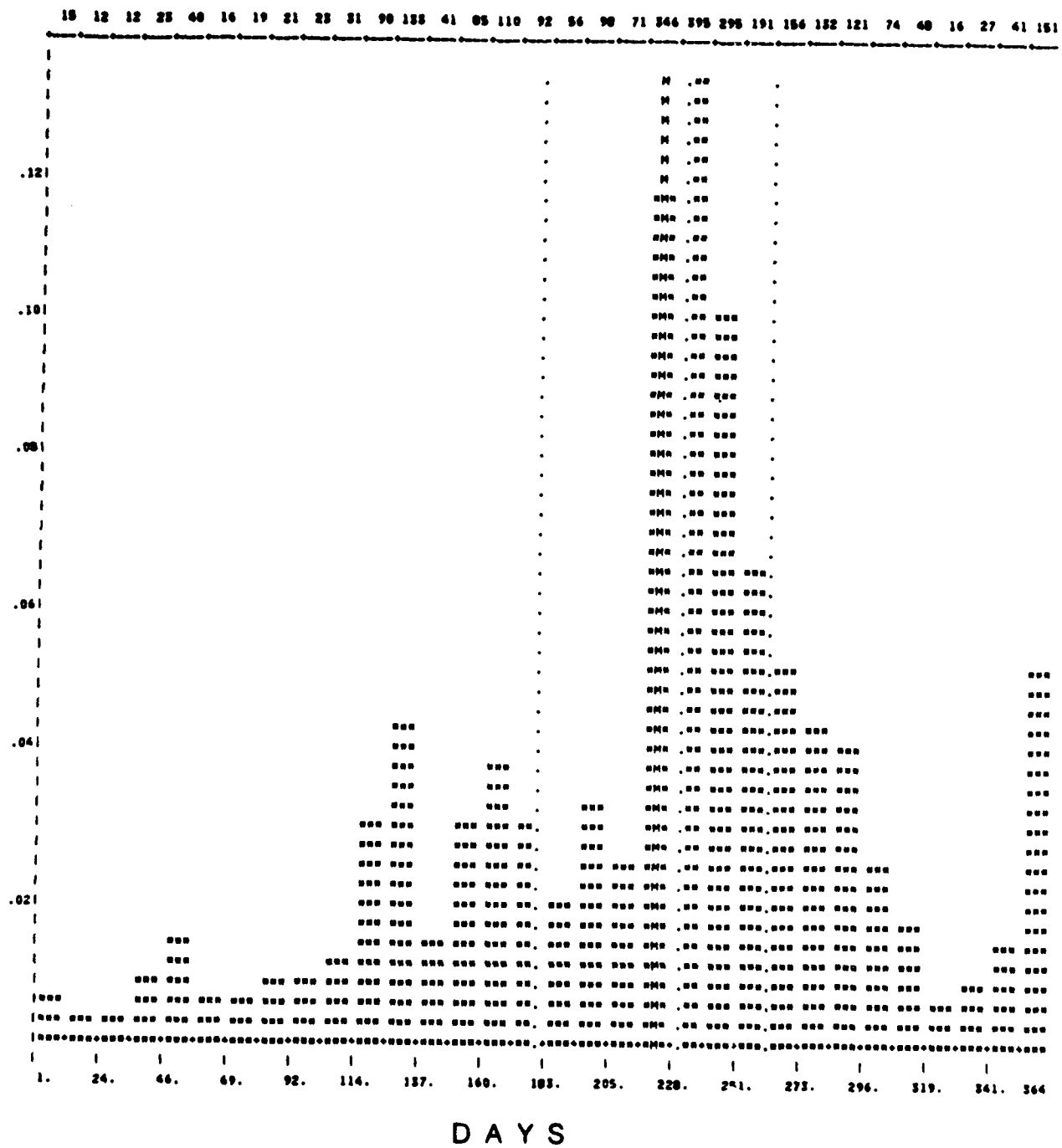


Figure 4.1a. The distribution of XBT casts at OWS P for 1961. The class interval is 22.8 days.

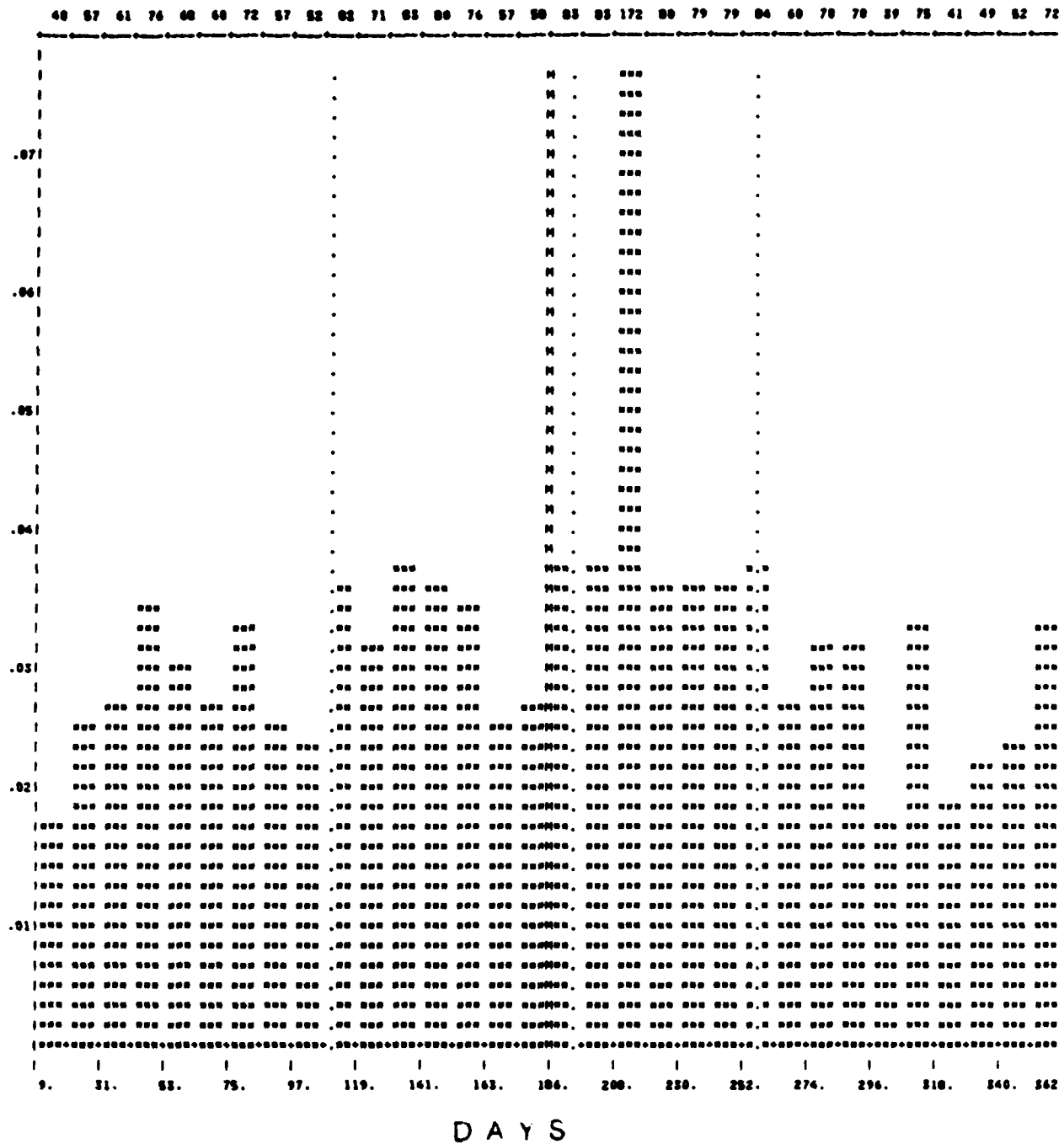


Figure 4.1b. The distribution of XBT casts at OWS P for 1965. The class interval is 22.8 days.



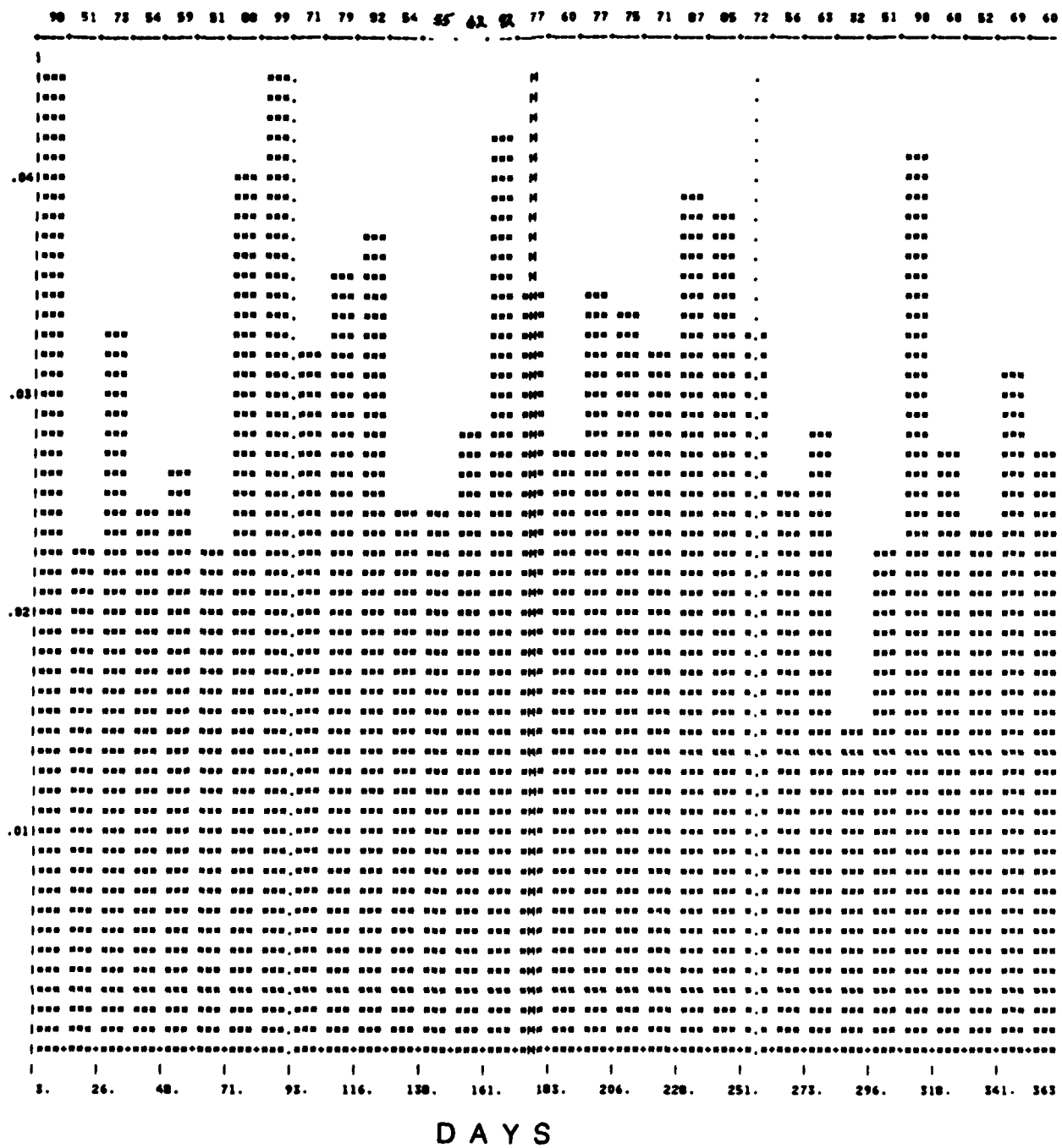


Figure 4.1c. The distribution of XBT casts at OWS P for 1966. The class interval is 22.8 days.

20 24 77 65 64 90 85 80 47 79 79 94 52 84 91 64 81 96 88 65 58 29 45 62 78 61 52 87 59 18 41 74

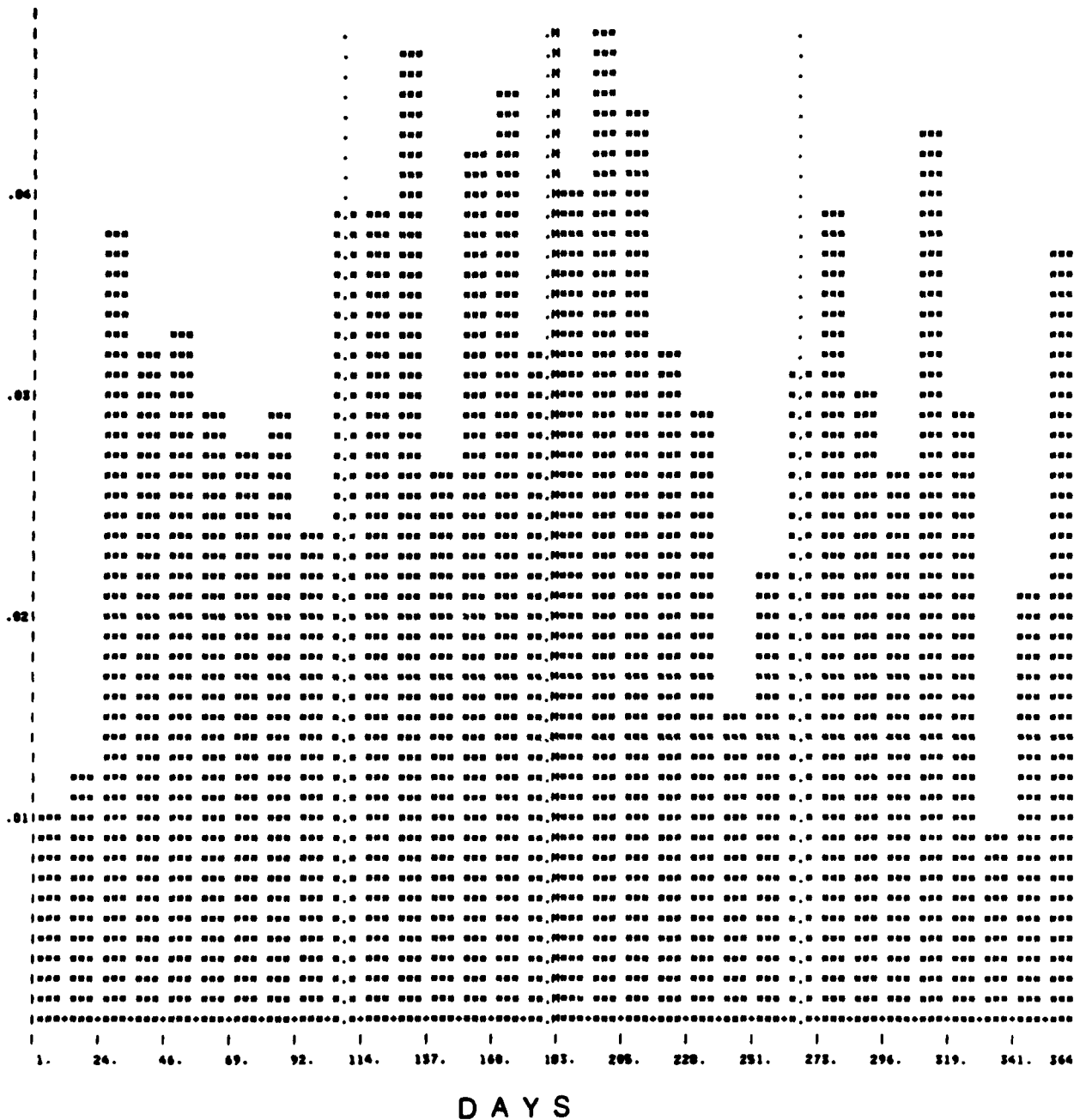


Figure 4.1d. The distribution of XBT casts at OWS P for 1967. The class interval is 22.8 days.

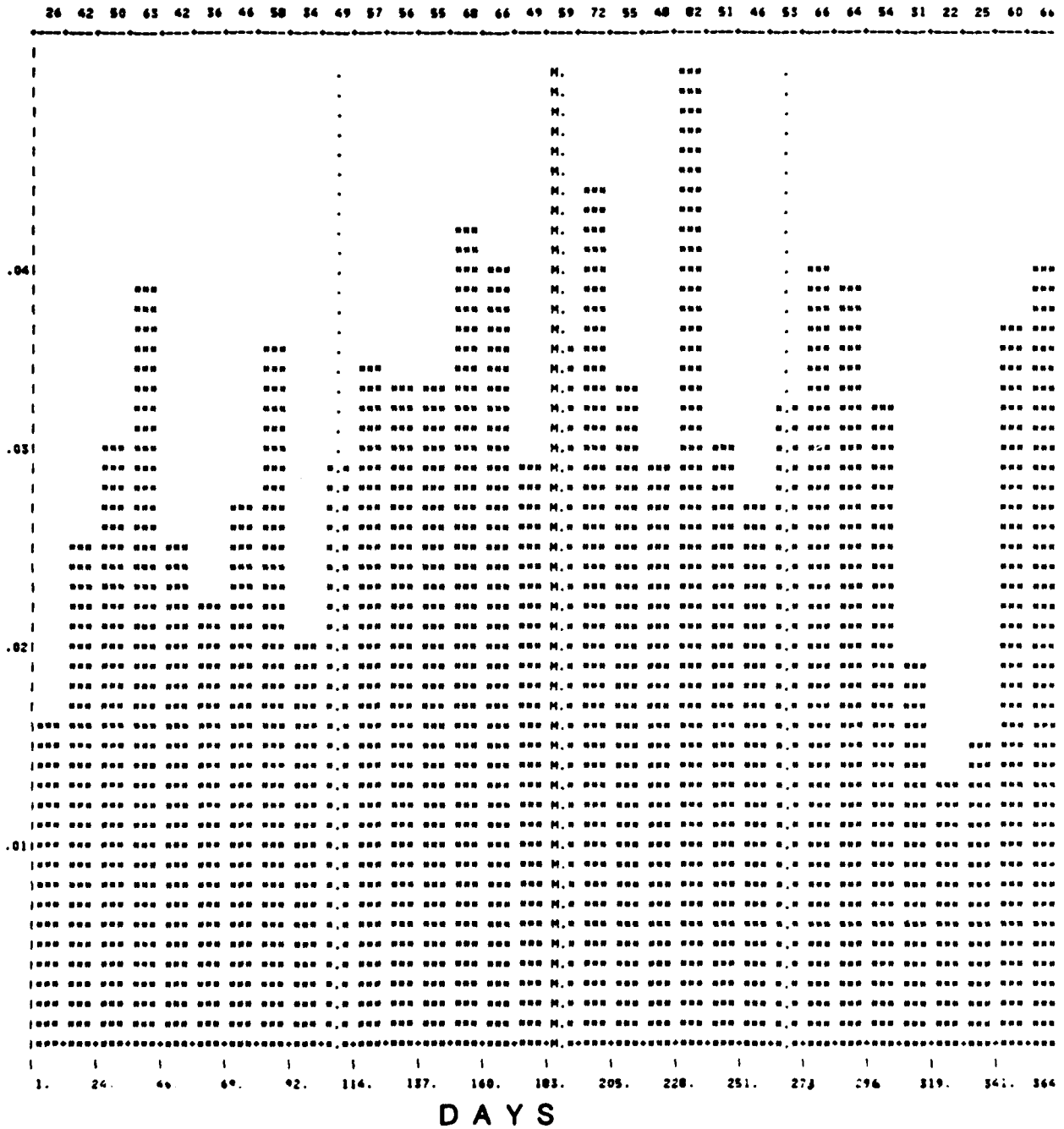


Figure 4.1e. The distribution of XBT casts at OWS N for 1961. The class interval is 22.8 days.

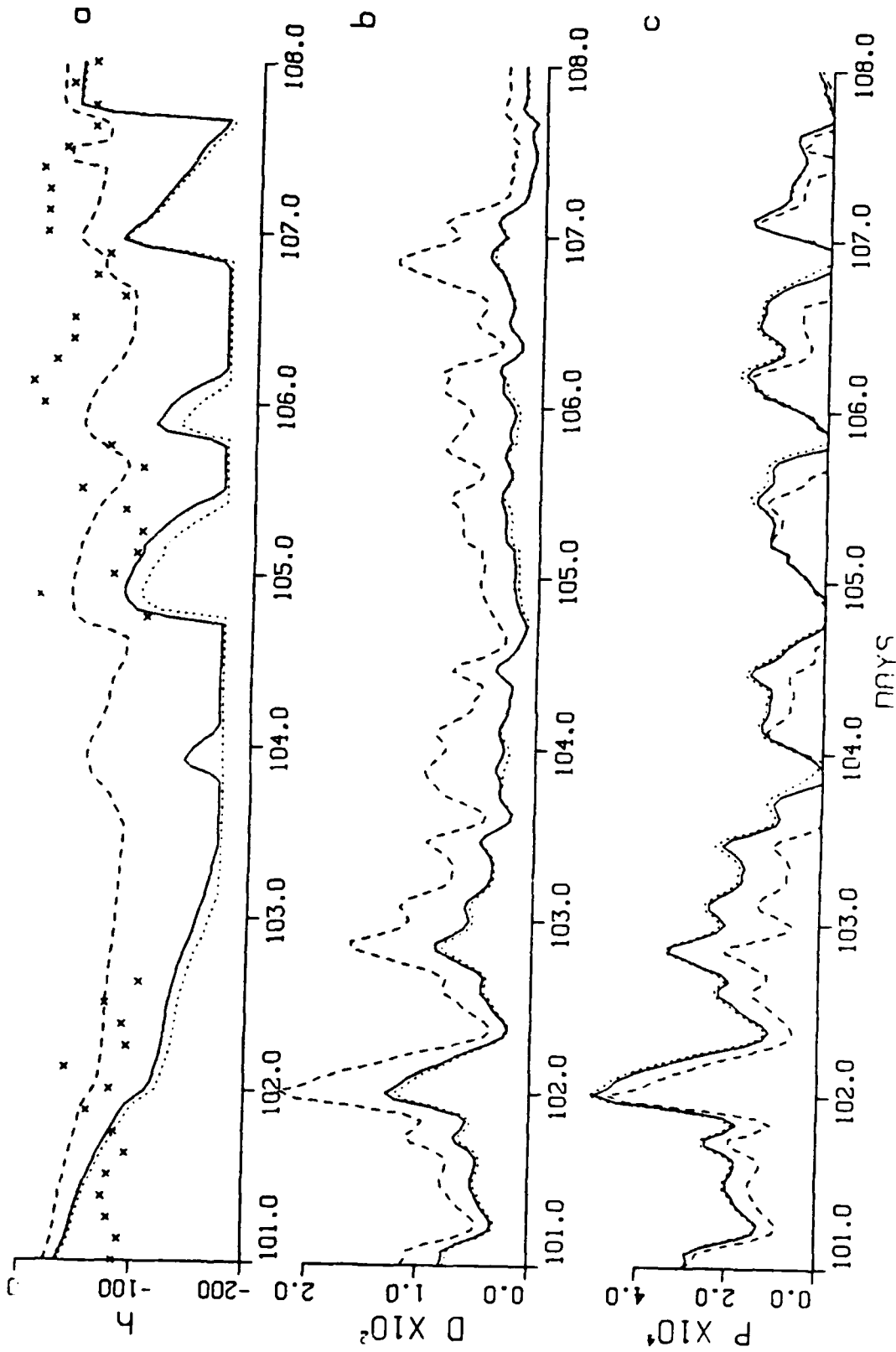


Figure 4.2. 1967 Days 101-108, OW&P. a) mixed layer depth (m), b) dissipation rate (cm<sup>2</sup>s<sup>-3</sup>) and c) entrainment rate (cm<sup>2</sup>s<sup>-3</sup>) for the RSTAR (solid), IJSTAR (dotted) and ZSTAR (dashed) models. The X's are the mixed layer depths calculated from the BT's.

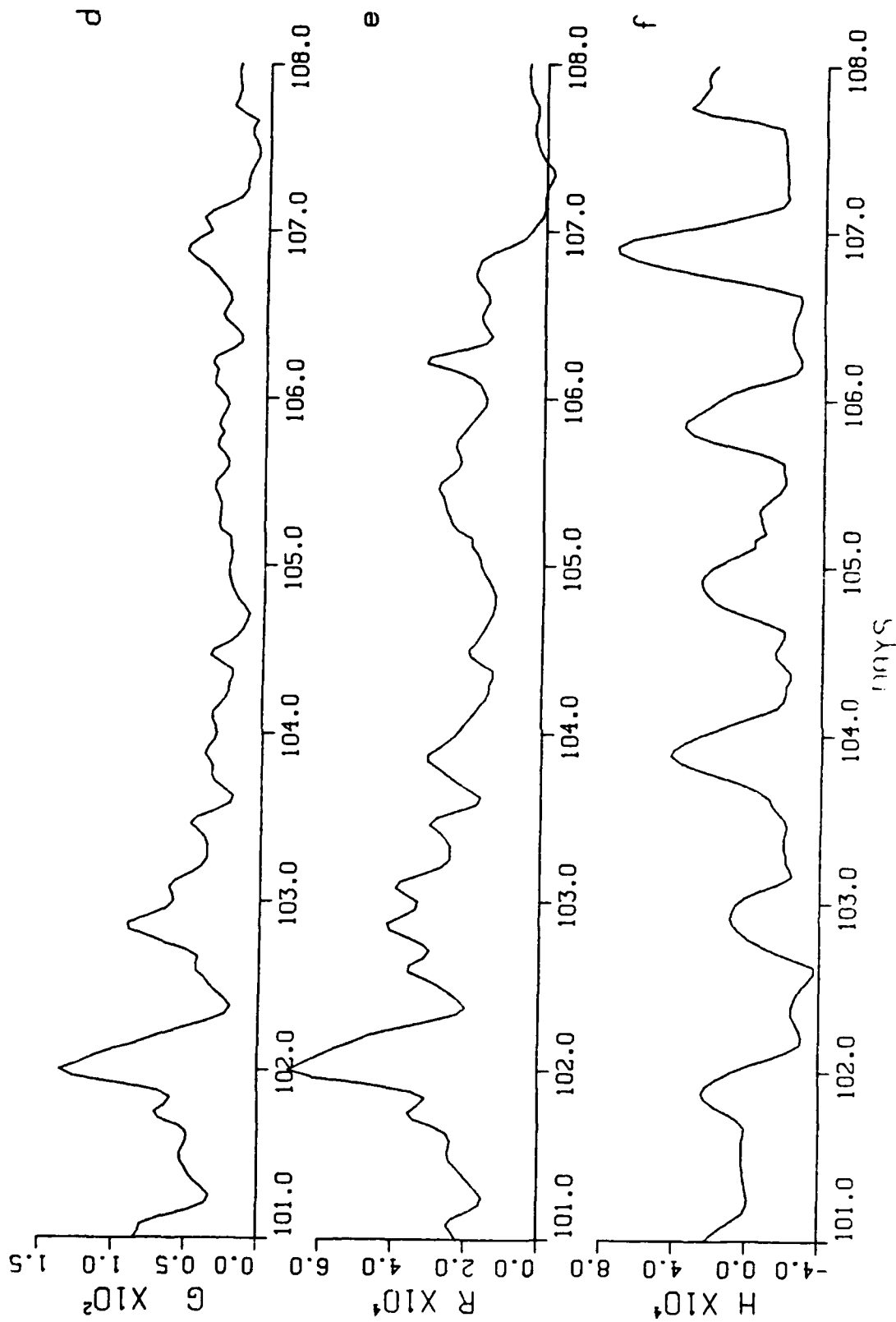


Figure 4.2. cont. d) wind-stress shear production, e) rotation stress, and f) surface buoyancy flux ( $\text{cm}^2\text{s}^{-3}$ ).

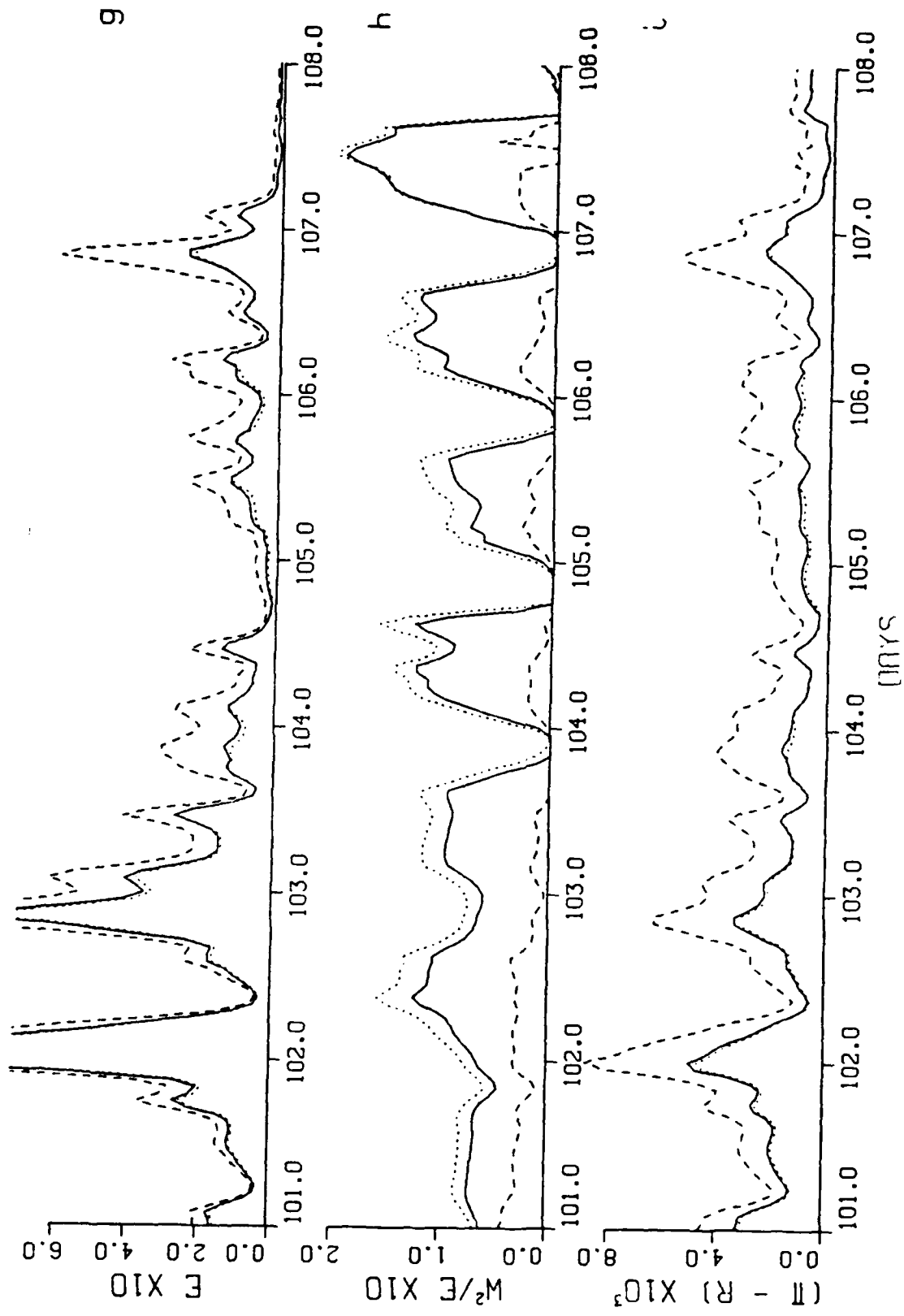


Figure 4.2. cont. g) total TKE ( $\text{cm}^2\text{s}^{-2}$ ), h) ratio of vertical to total TKE, and i) TKE transfer rate due to the pressure-rate of strain minus rotation stress ( $\text{cm}^2\text{s}^{-3}$ ).

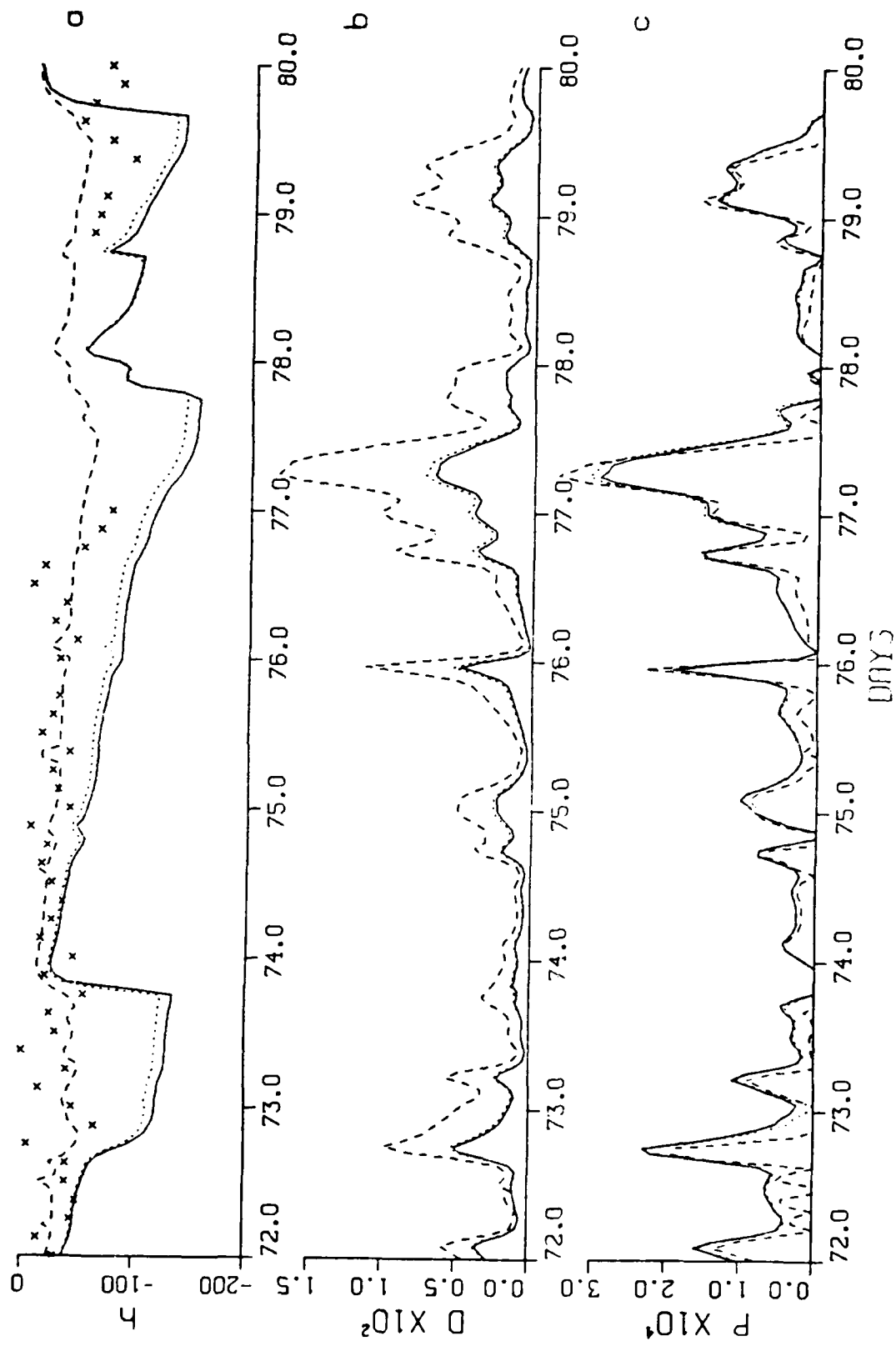


Figure 4.3. 1965 Days 72-80, OWS P<sub>3</sub> a) mixed layer depth (m), b) dissipation rate ( $\text{cm}^2 \text{s}^{-3}$ ) and c) entrainment rate, ( $\text{cm}^2 \text{s}^{-3}$ ) for the RSTAR (solid), ISTAR (dotted) and ZSTAR (dashed) models. The X's are the mixed layer depths calculated from the BJCS.

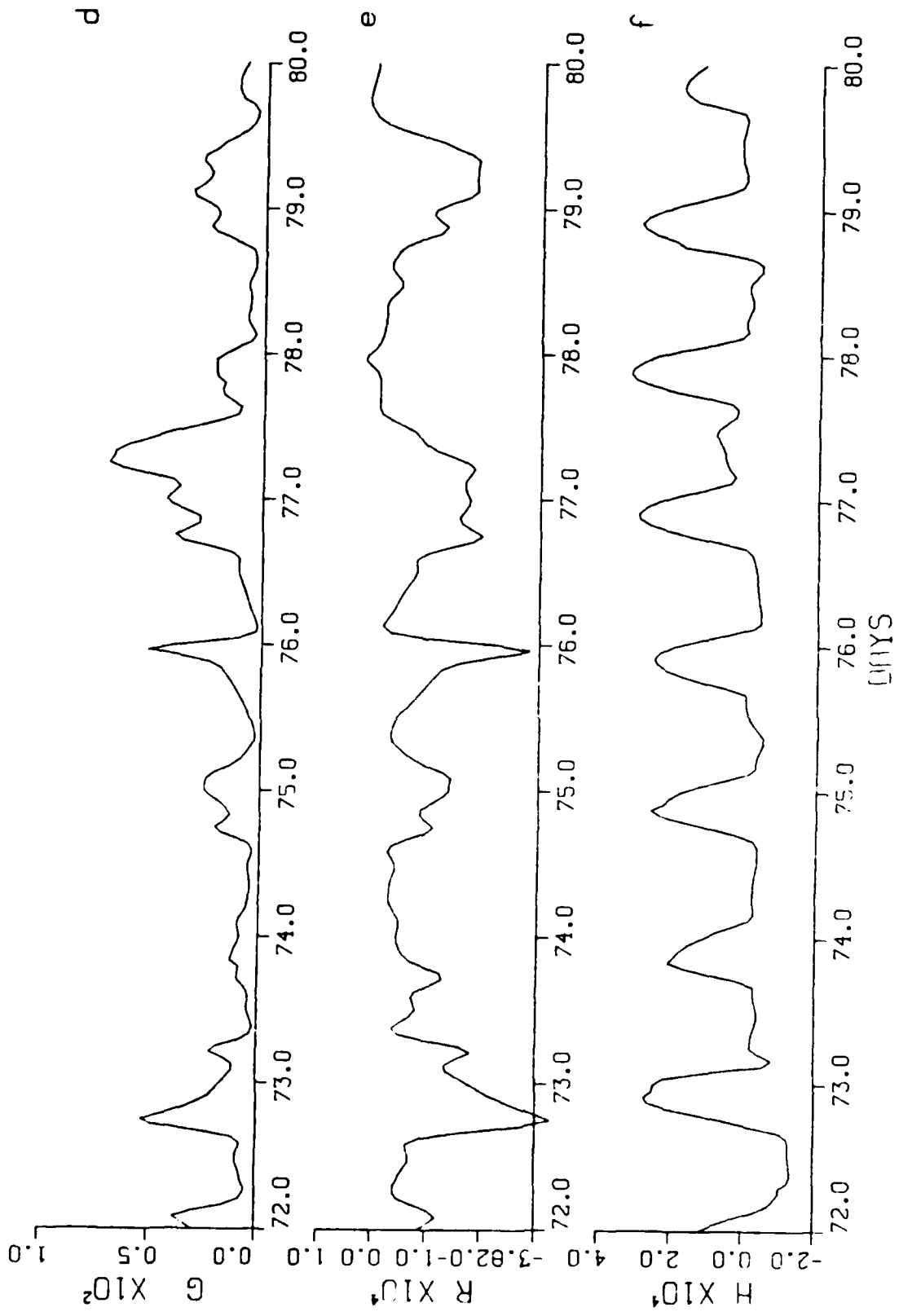


Figure 4.3. cont. d) wind-stress shear production, e) rotation stress, and f) surface buoyancy flux ( $\text{cm}^2 \text{s}^{-1}$ ).



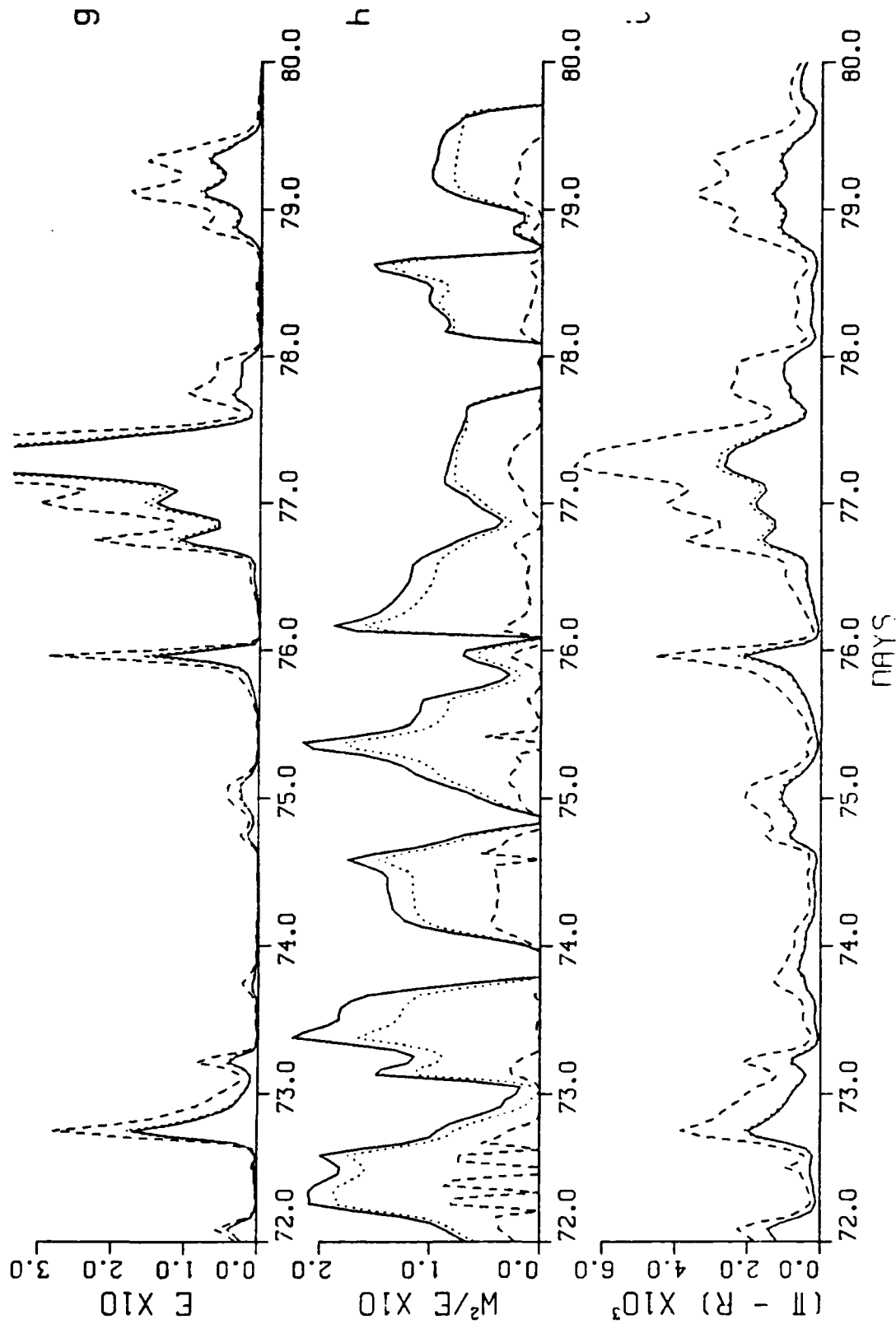


Figure 4.3. cont. g) total TKE ( $\text{cm}^2 \text{s}^{-2}$ ), h) ratio of vertical to total TKE and i) TKE transfer rate due to the pressure-rate of strain minus rotation stress ( $\text{cm}^2 \text{s}^{-3}$ ).

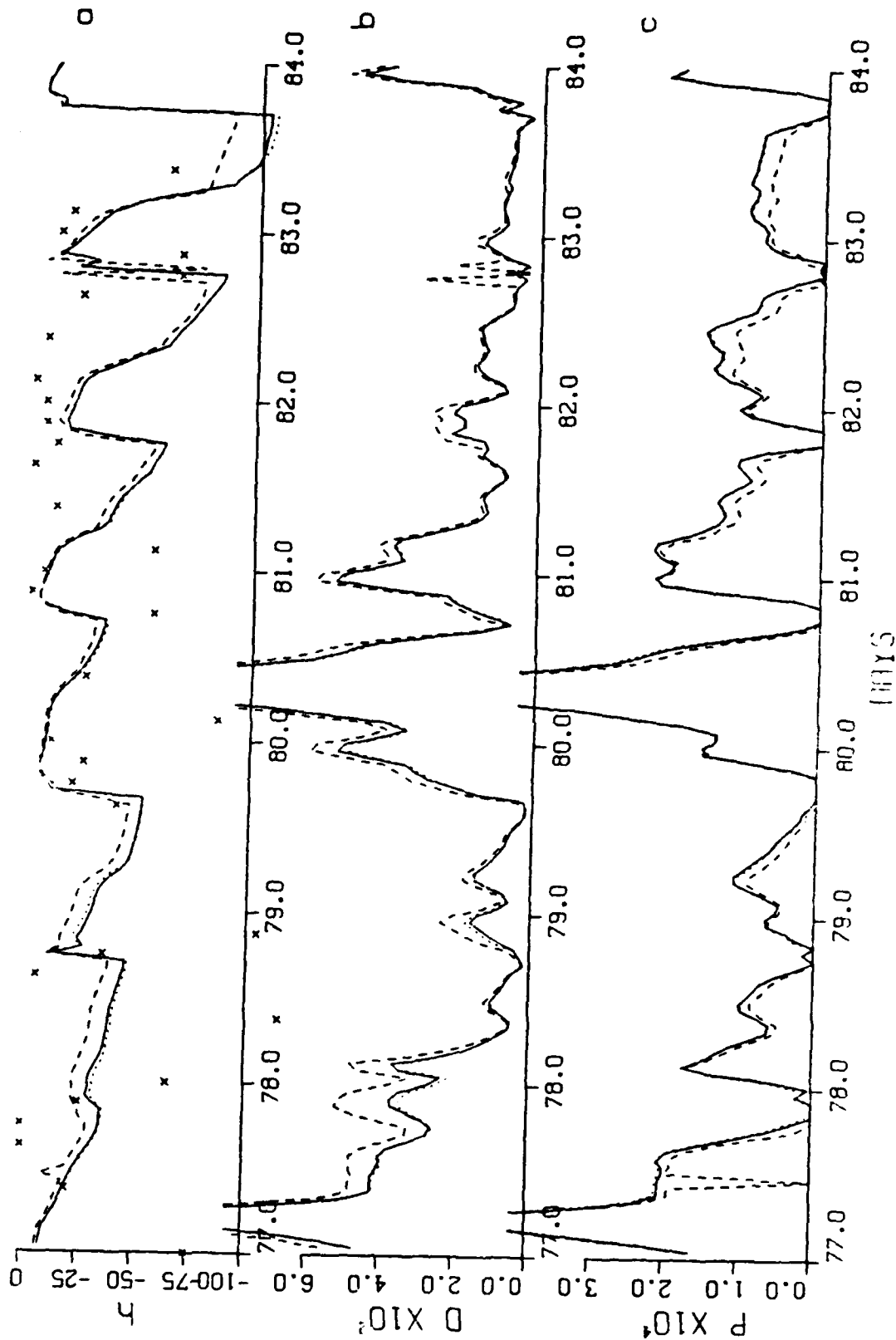


Figure 4.4. 1961 Days 77-84, OWS N. a) mixed layer depth (m), b) dissipation rate (cm<sup>2</sup> s<sup>-3</sup>) and c) entrainment rate (cm<sup>2</sup> s<sup>-3</sup>) for the RSTAR (solid), ISTAR (dotted) and ZSTAR (dashed) models. The X's are the mixed layer depths calculated from the BT's.

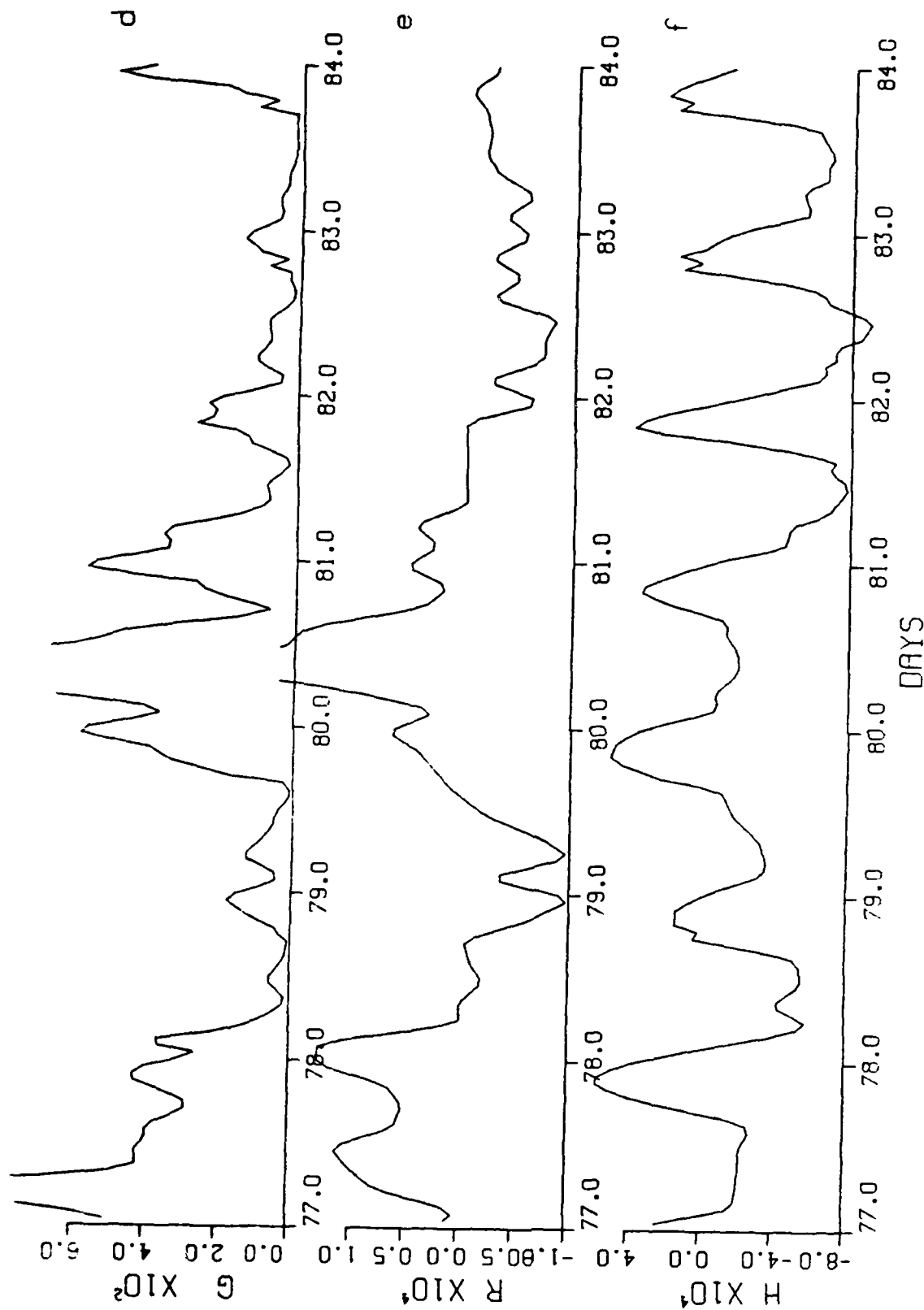


Figure 4.4. cont. d) wind-stress shear production, e) rotation stress, and f) surface buoyancy flux ( $\text{cm}^2\text{s}^{-3}$ ).

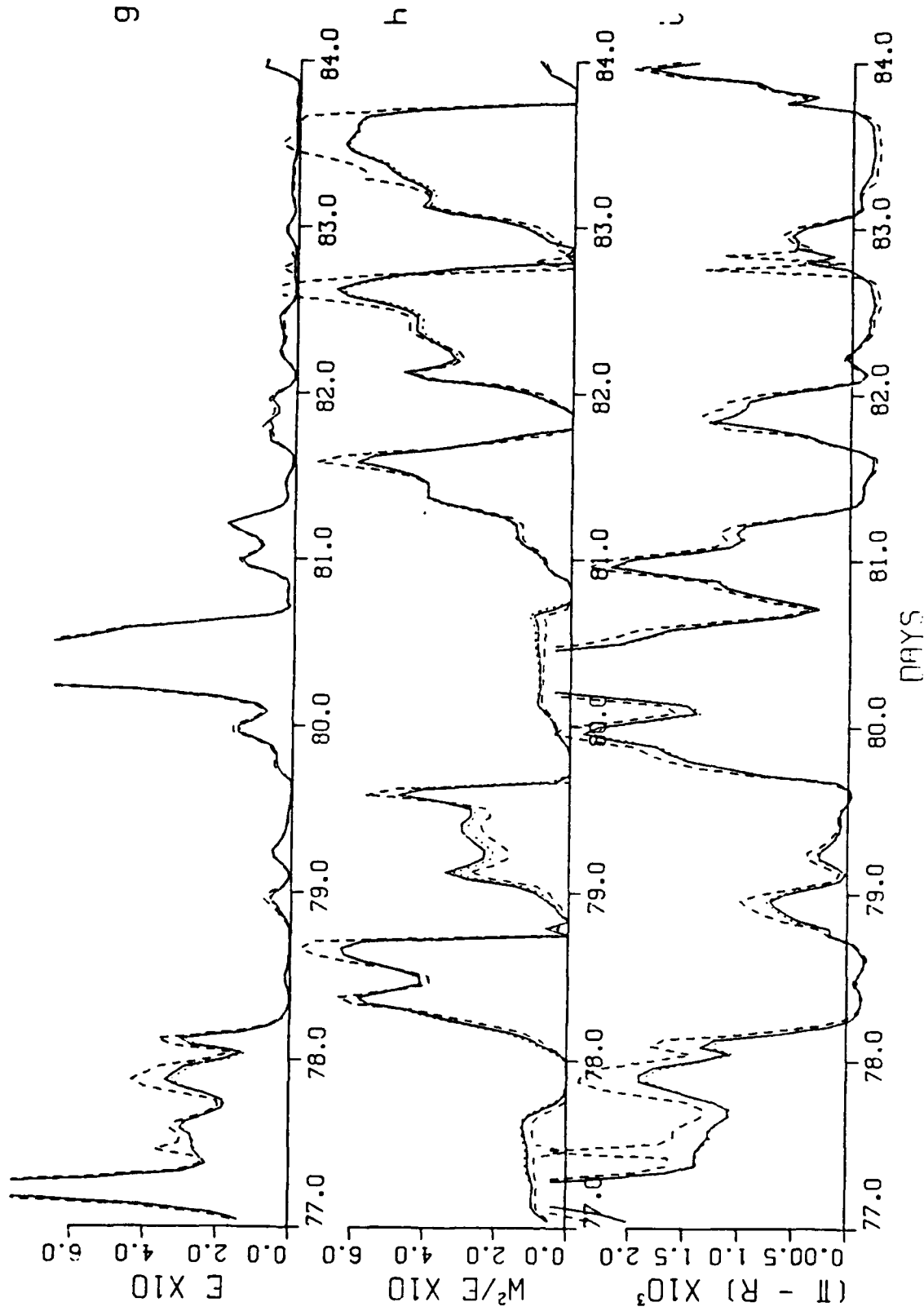


Figure 4.4. cont. g) total TKE ( $\text{cm}^2 \text{s}^{-2}$ ), h) ratio of vertical to total TKE, and i) IKE transfer rate due to the pressure-rate of strain minus rotation stress ( $\text{cm}^2 \text{s}^{-3}$ ).

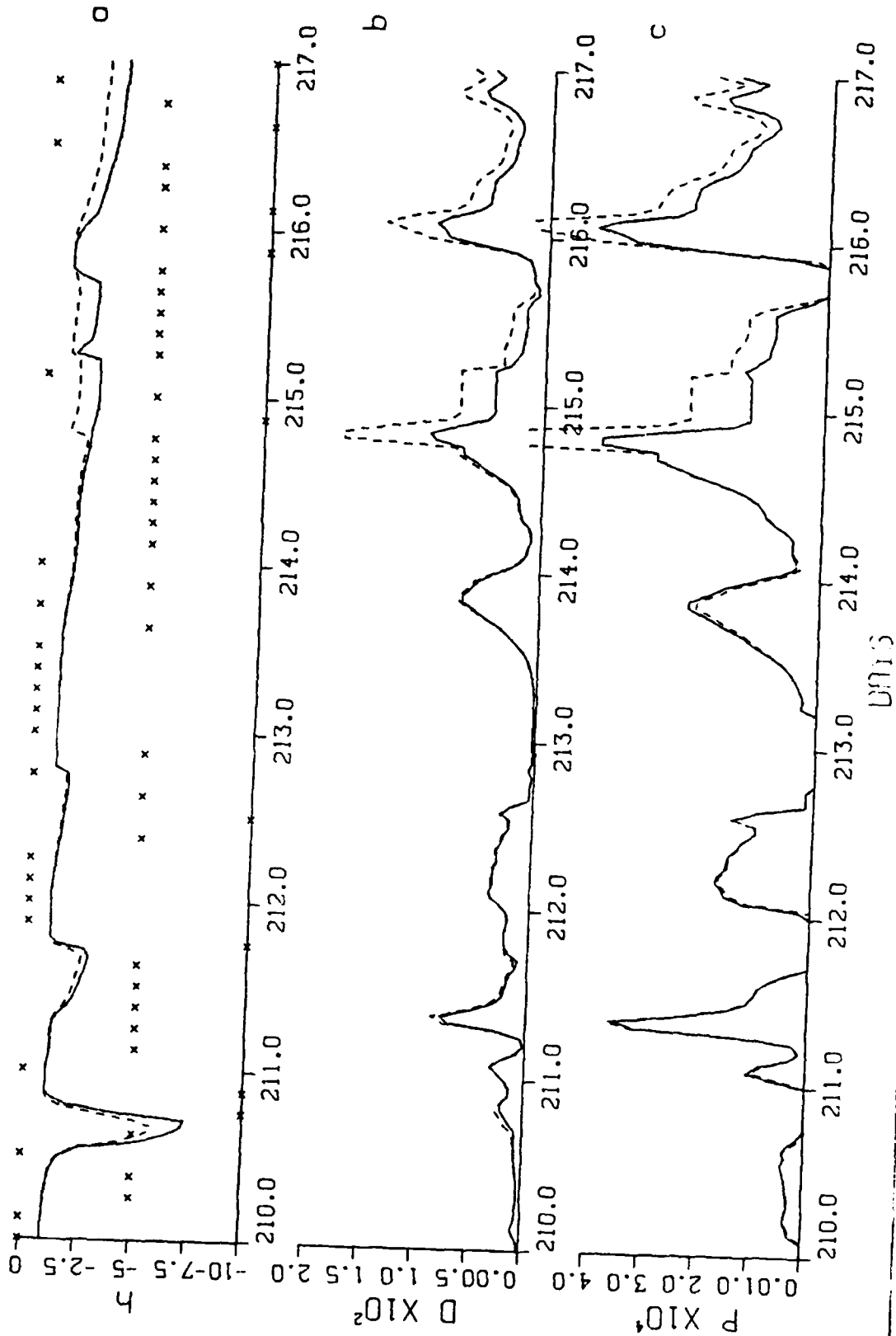


Figure 4.5. 1967 Days 210-217, OWS P<sub>3</sub>: a) mixed layer depth (m), b) dissipation rate ( $\text{cm}^2 \text{s}^{-3}$ ) and c) entrainment rate ( $\text{cm}^2 \text{s}^{-3}$ ) for the RSTAR (solid), ISTAR (dotted) and 7STAR (dashed) models. The X's are the mixed layer depths calculated from the BT's.

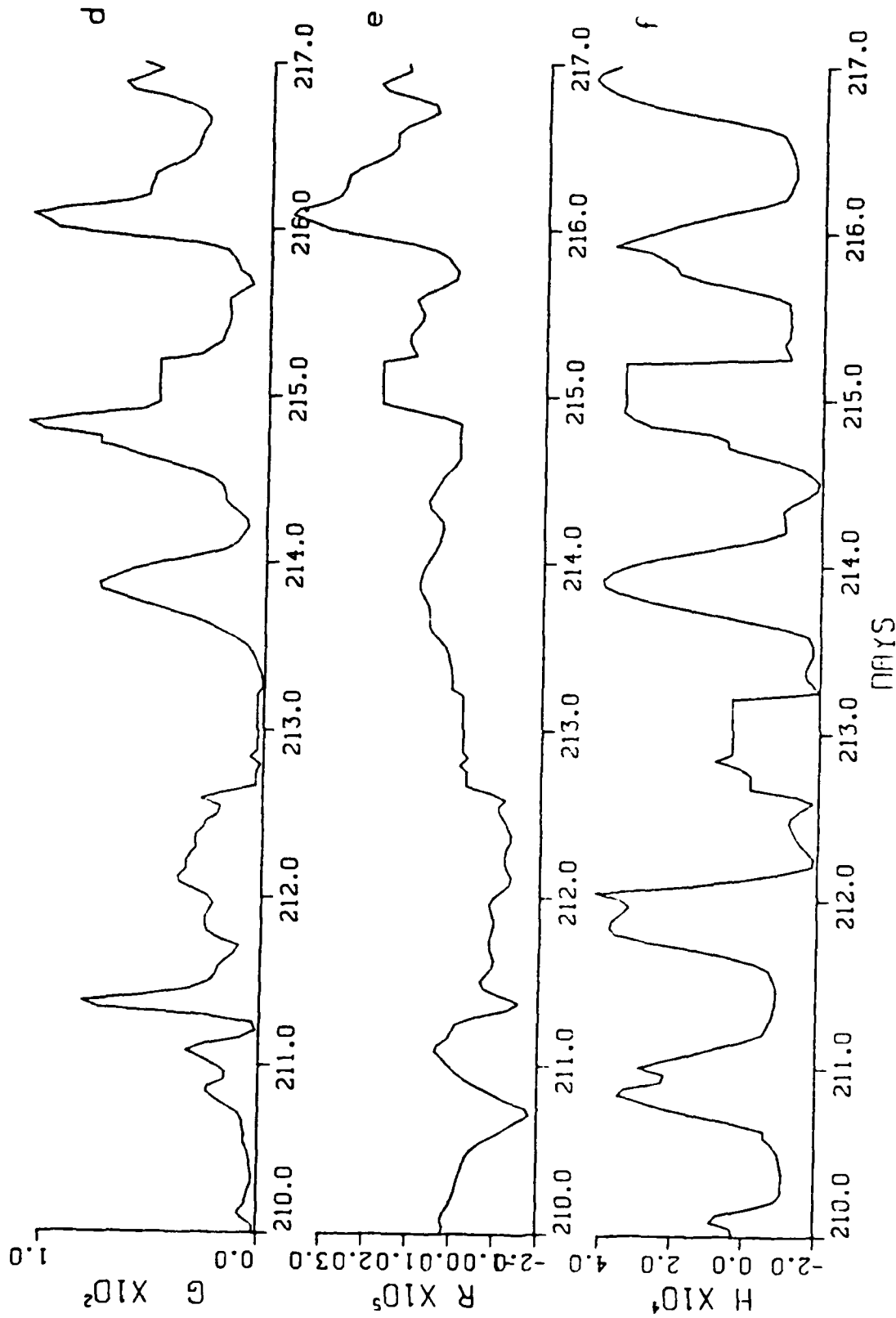


Figure 4.5. cont. d) wind-stress shear production, e) rotation stress, and f) surface buoyancy flux ( $\text{cm}^2 \text{s}^{-3}$ ).

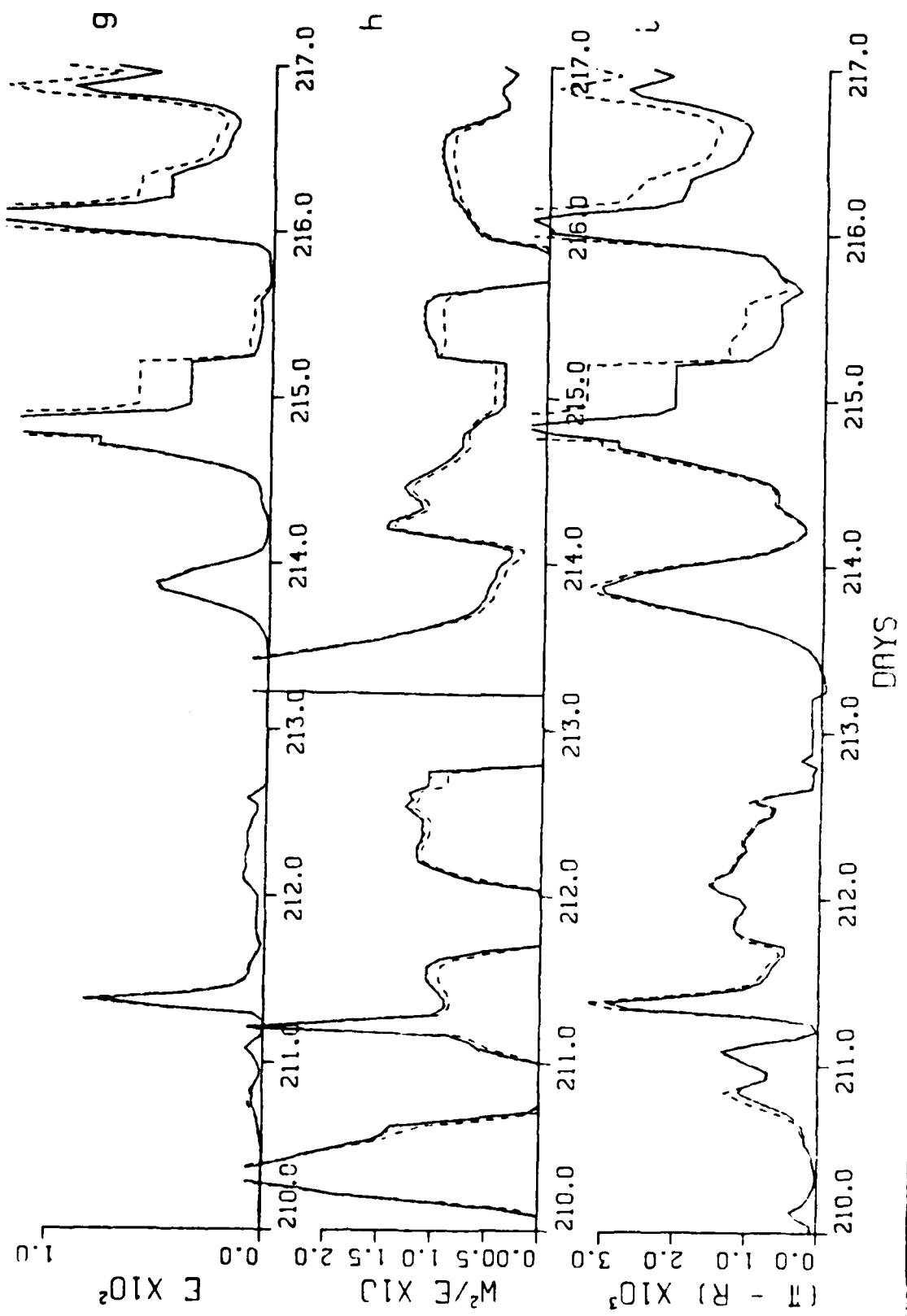


Figure 4.5. cont. g) total TKE ( $\text{cm}^2\text{s}^{-2}$ ), h) ratio of vertical to total TKE and i) TKE transfer rate due to the pressure-rate of strain minus rotation stress ( $\text{cm}^2\text{s}^{-3}$ ).

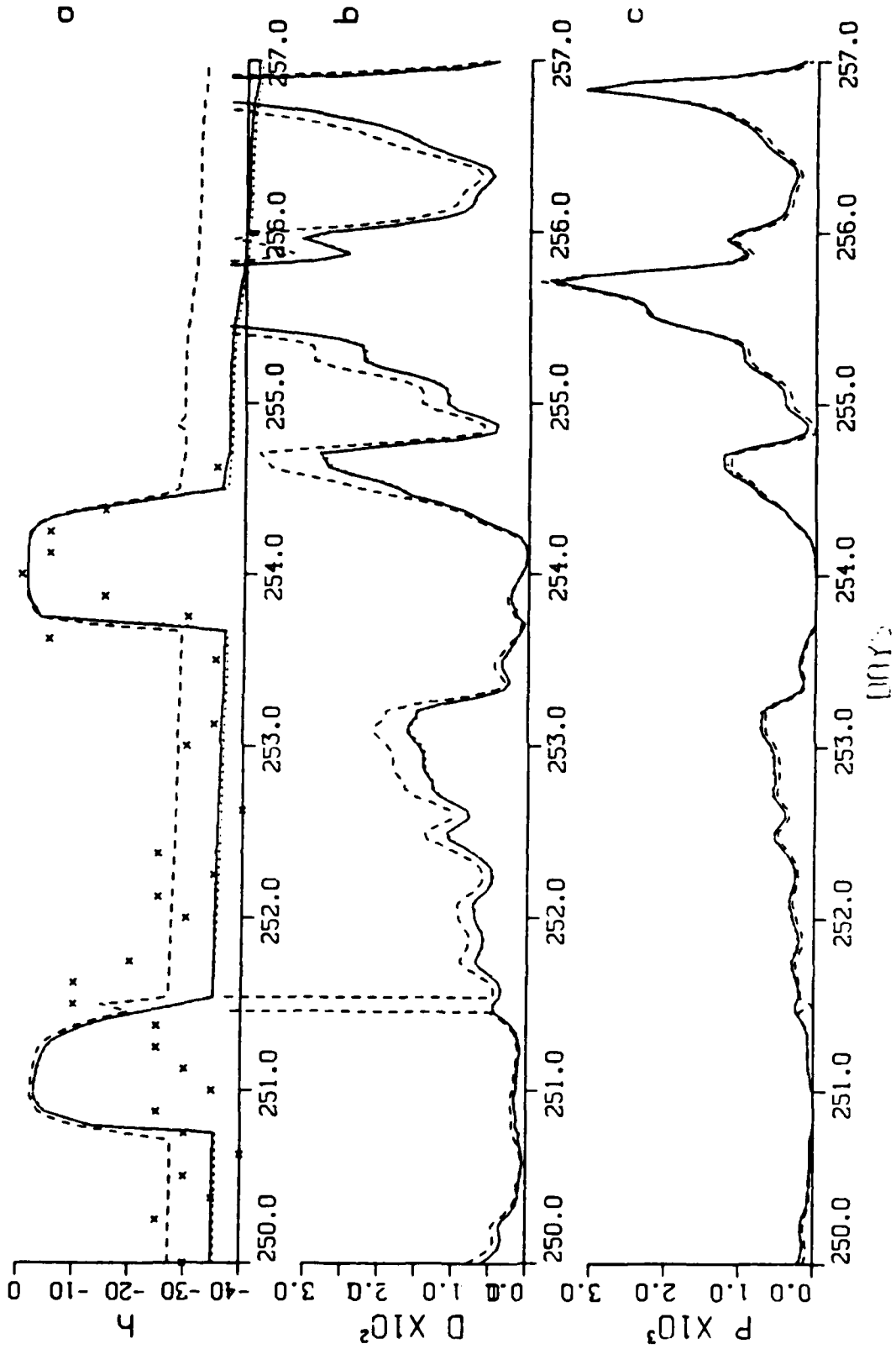


Figure 4.6. 1967 Days 250-257, OWS P<sub>1</sub> a) mixed layer depth (m), b) dissipation rate ( $\text{cm}^2\text{s}^{-3}$ ) and c) entrainment rate ( $\text{cm}^2\text{s}^{-3}$ ) for the RSTAR (solid), HISTAR (dotted) and ZSTAR (dashed) models. The X's are the mixed layer depths calculated from the BT's.



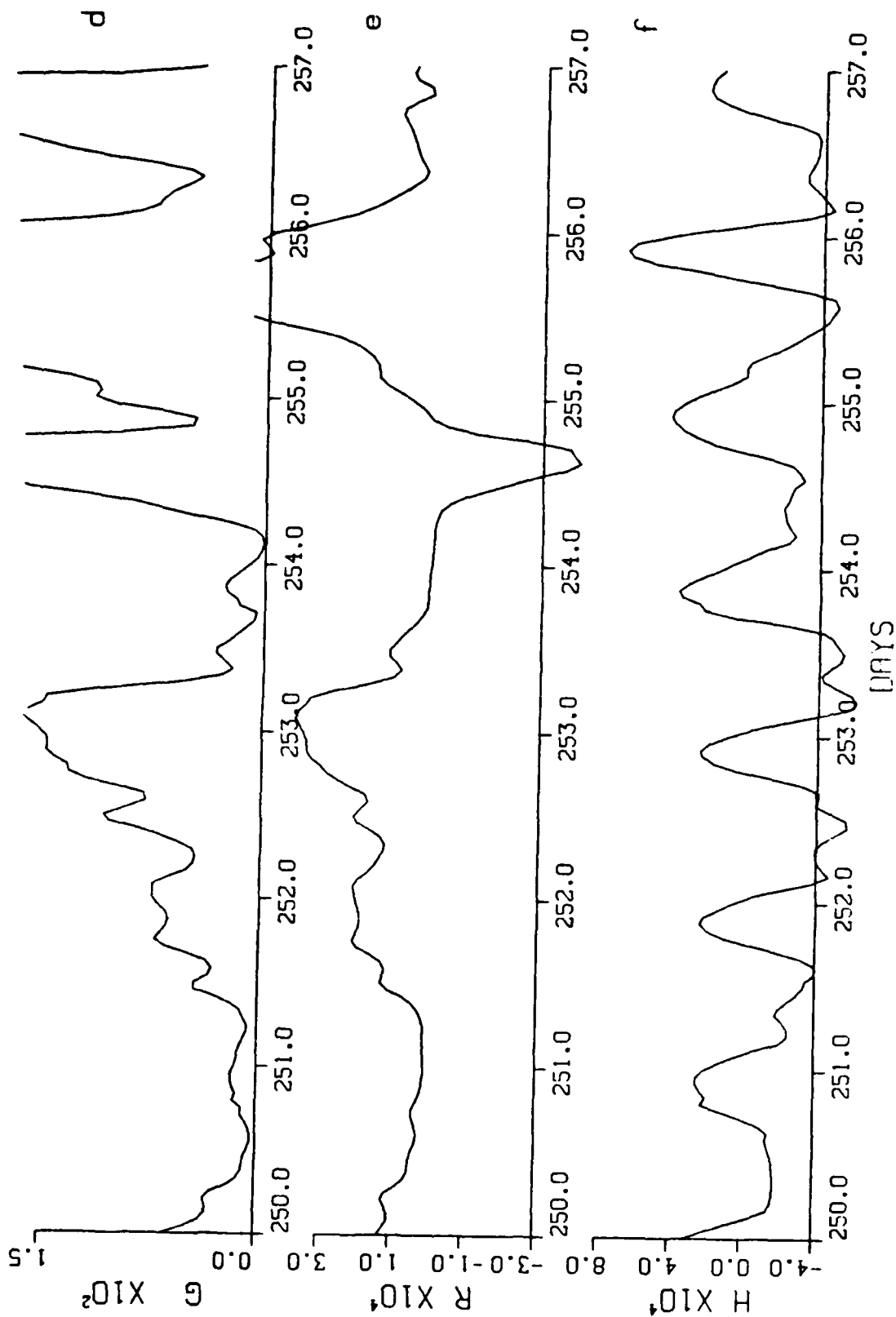


Figure 4.6, cont. d) wind-stress shear production, e) rotation stress, and f) surface buoyancy flux ( $\text{cm}^2\text{s}^{-3}$ ).

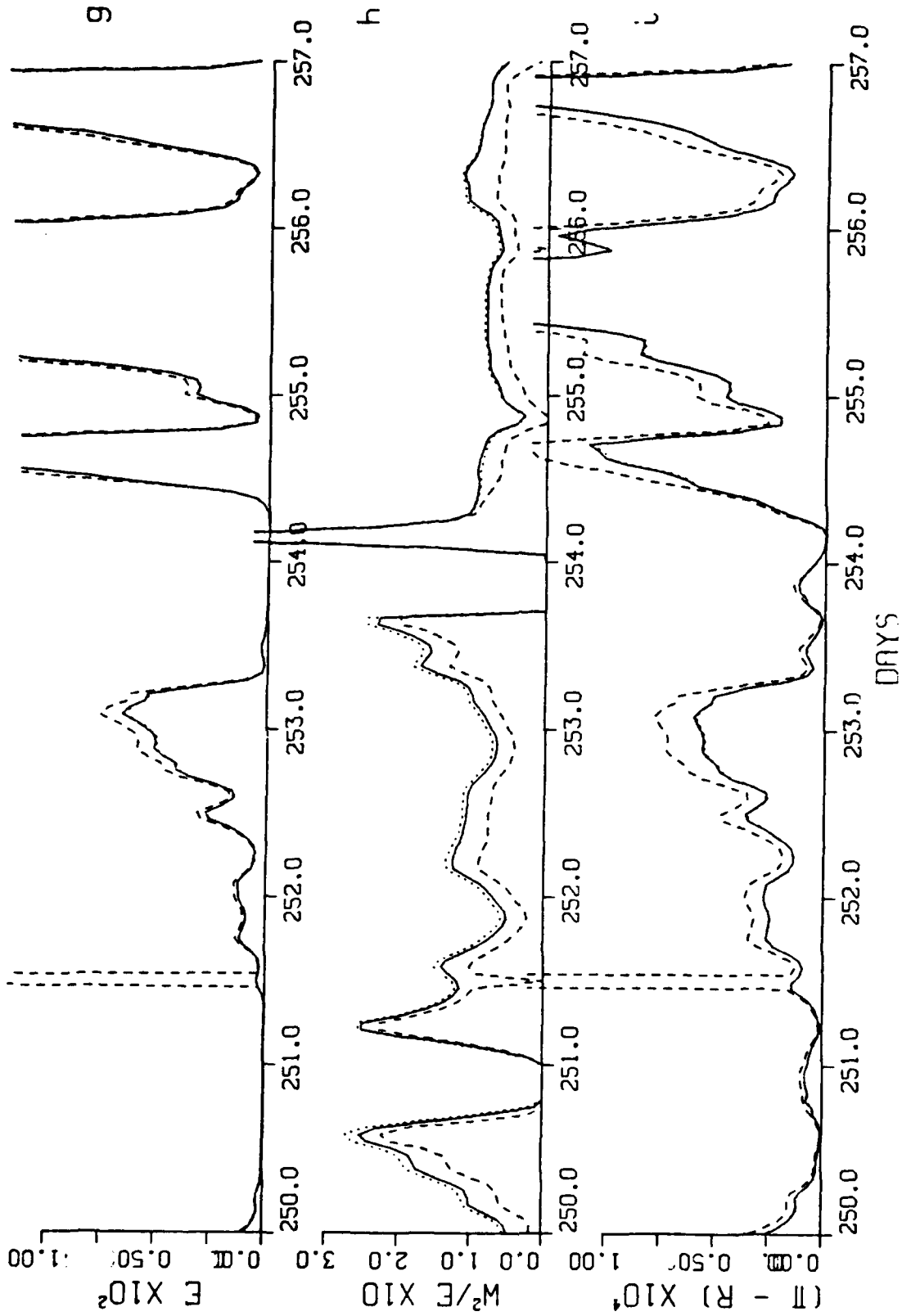


Figure 4.6. cont. g) total TKE ( $\text{cm}^2\text{s}^{-2}$ ), h) ratio of vertical to total TKE and i) TKE transfer rate due to the pressure-rate of strain minus rotation stress ( $\text{cm}^2\text{s}^{-3}$ ).

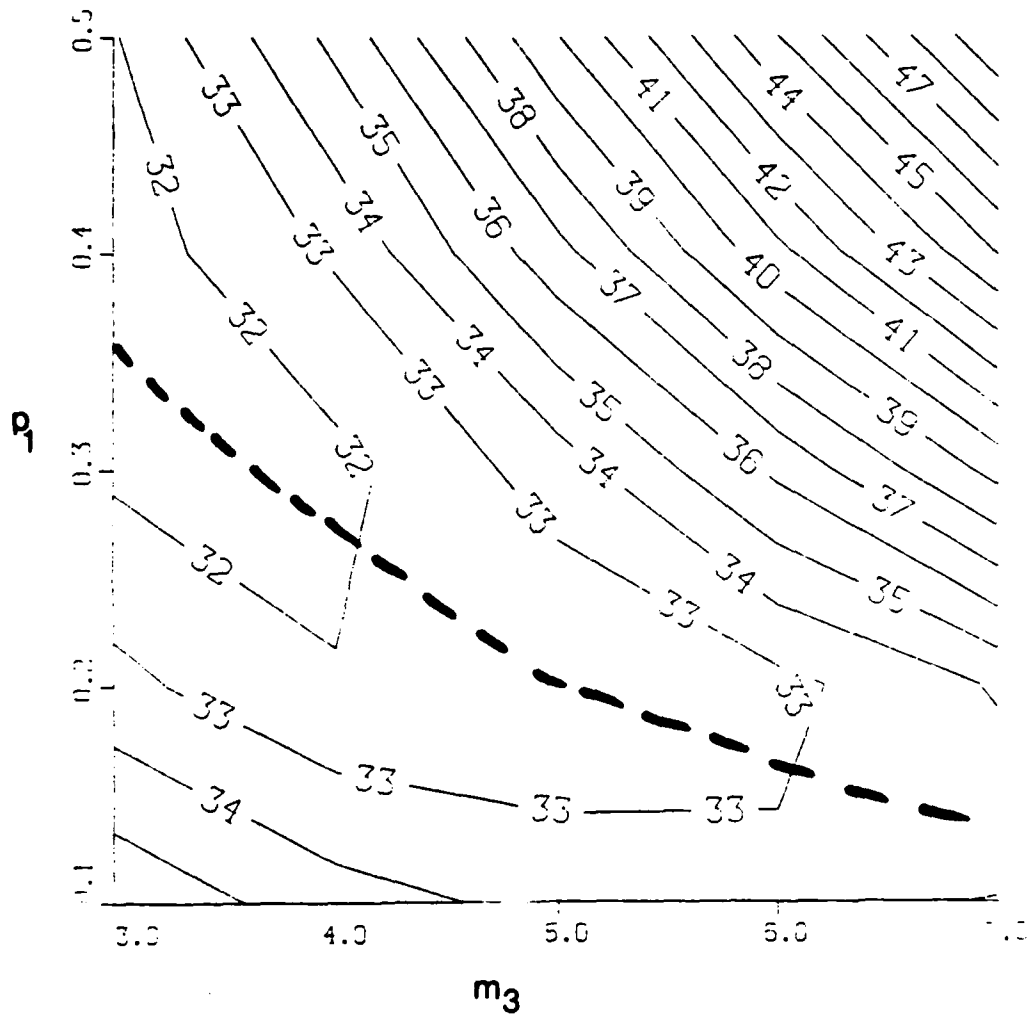


Figure 4.7b. Annual depth RMSE values during the tuning of the RSTAR model with  $p_2 = 0.5$  for the entire year of 1965 at OWS P.

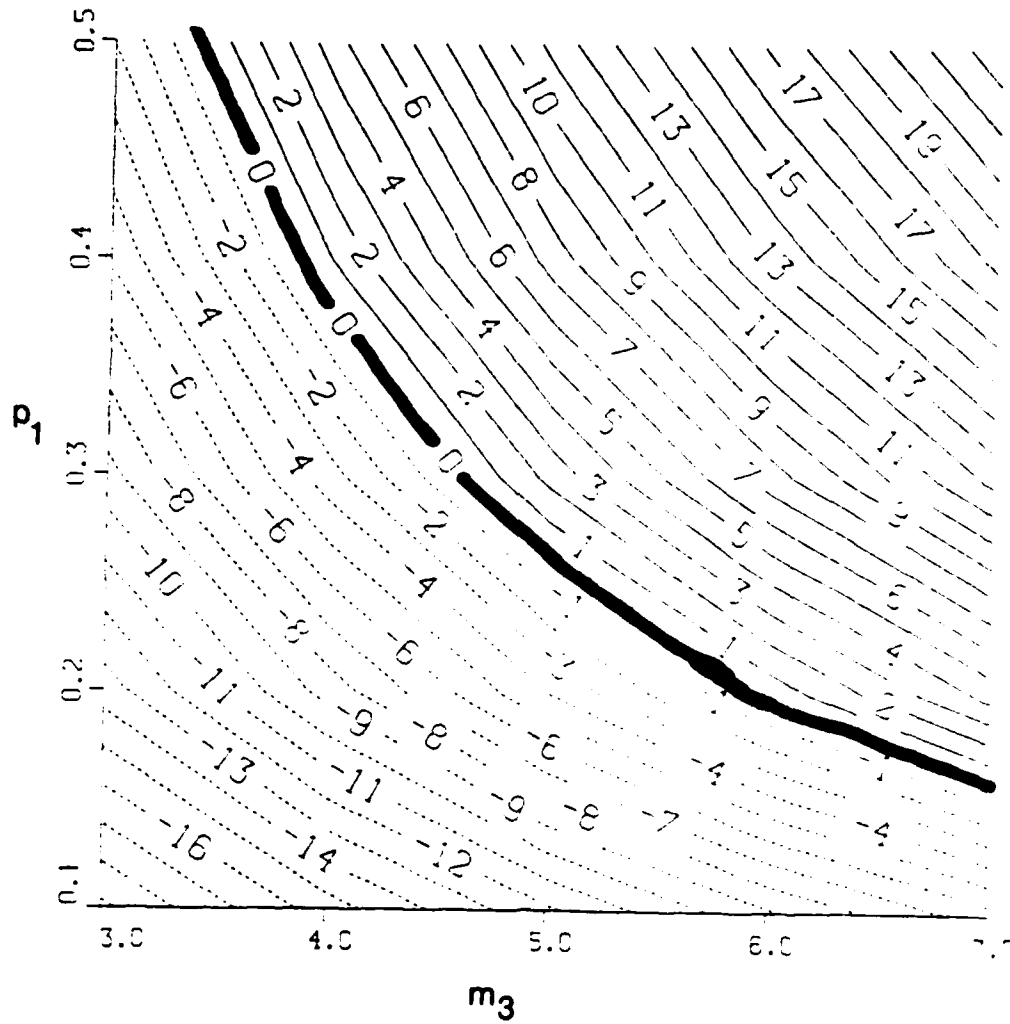


Figure 4.7a. Annual depth bias values during the tuning of the RSTAR model with  $p_2 = 0.5$  for the entire year of 1965 at OWS P.

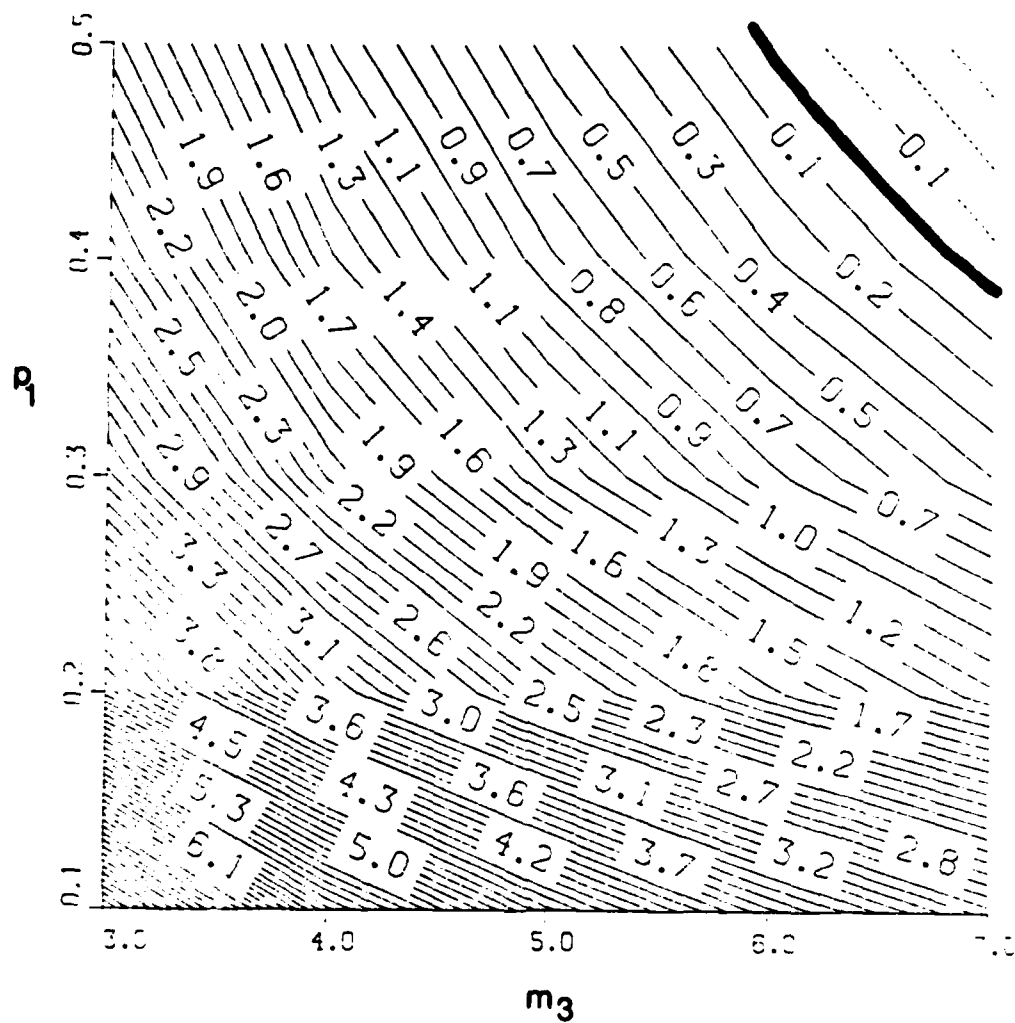


Figure 4.8a. Annual temperature bias values during the tuning of the RSTAR model with  $p_2 = 0.5$  for the entire year of 1965 at OWS P.

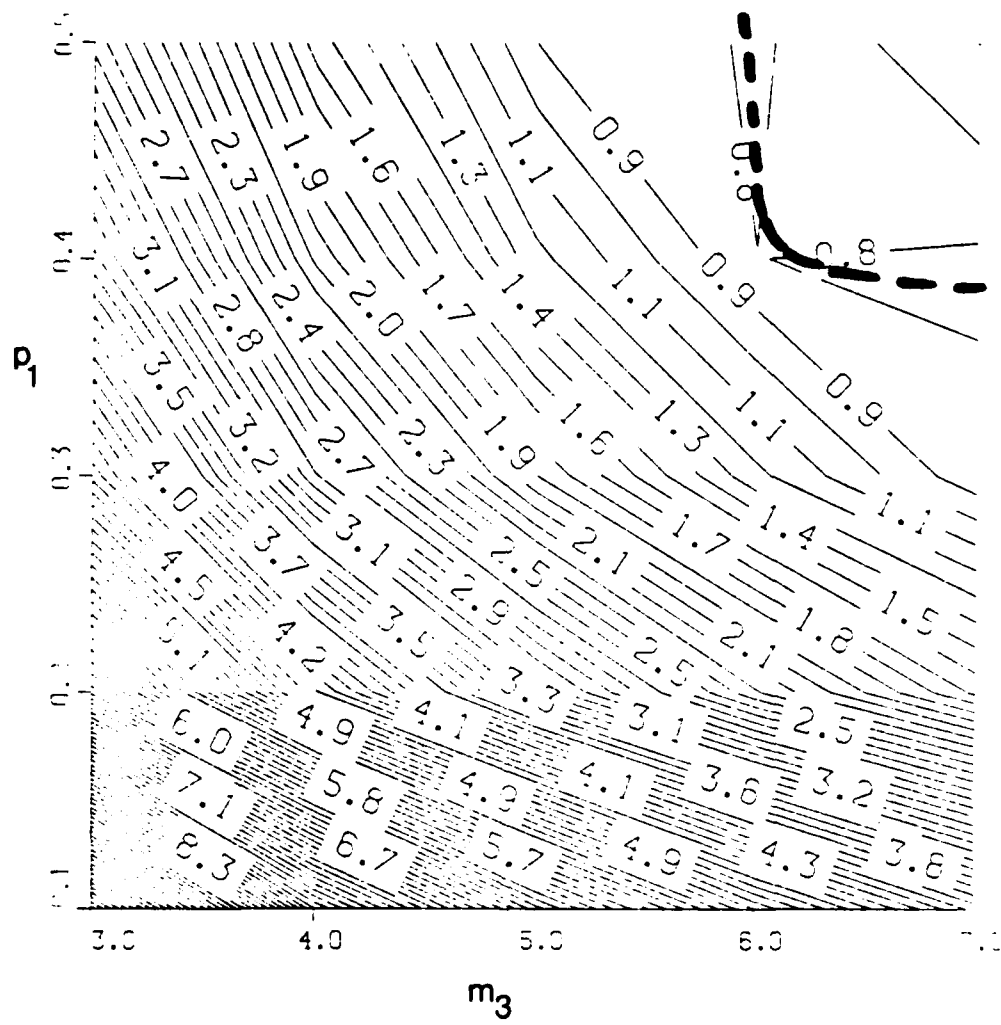


Figure 4.8b. Annual temperature RMSE values during the tuning of the RSTAR model with  $p_2 = 0.5$  for the entire year of 1965 at OWS P.

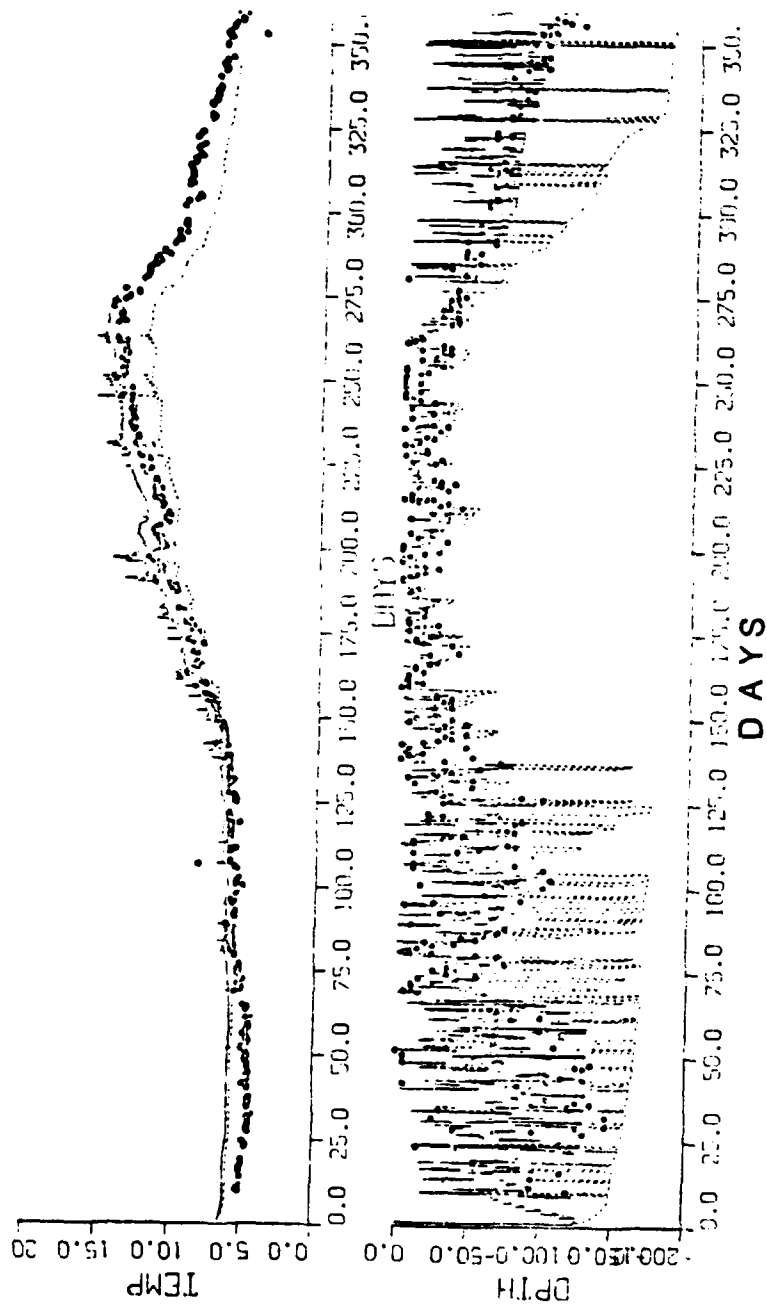


Figure 4.9. Comparison of annual simulations with the ZSTAR (solid) and HSTAR (dashed) models using the same tuning constant values with the observations (filled dots) for 1965 at OWS P to demonstrate the need for enhanced dissipation.

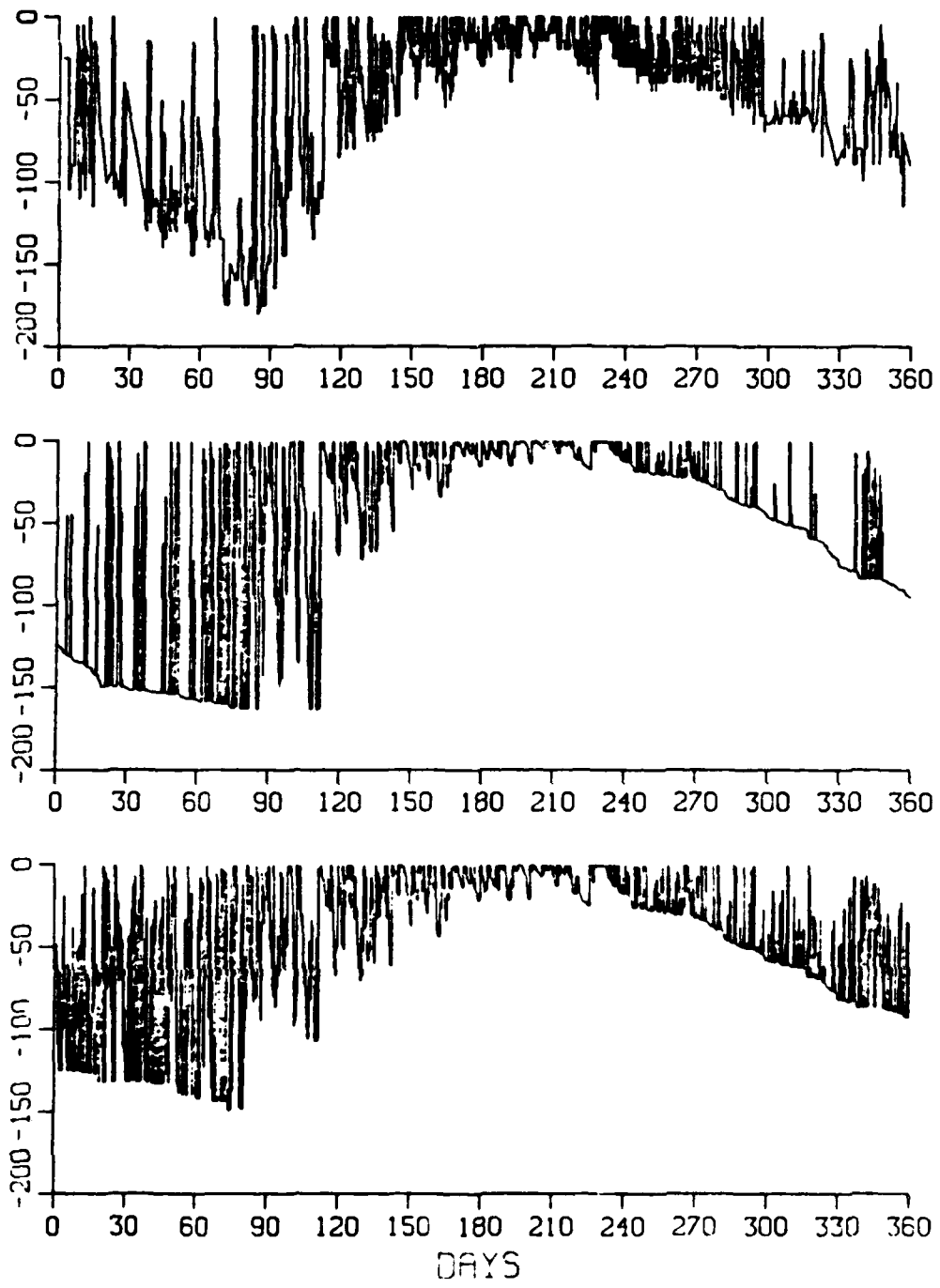


Figure 4.10a. OWS P, 1961. Mixed layer depth: top curve is the observations, middle curve is the RSTAR model, bottom curve is the ZSTAR model.



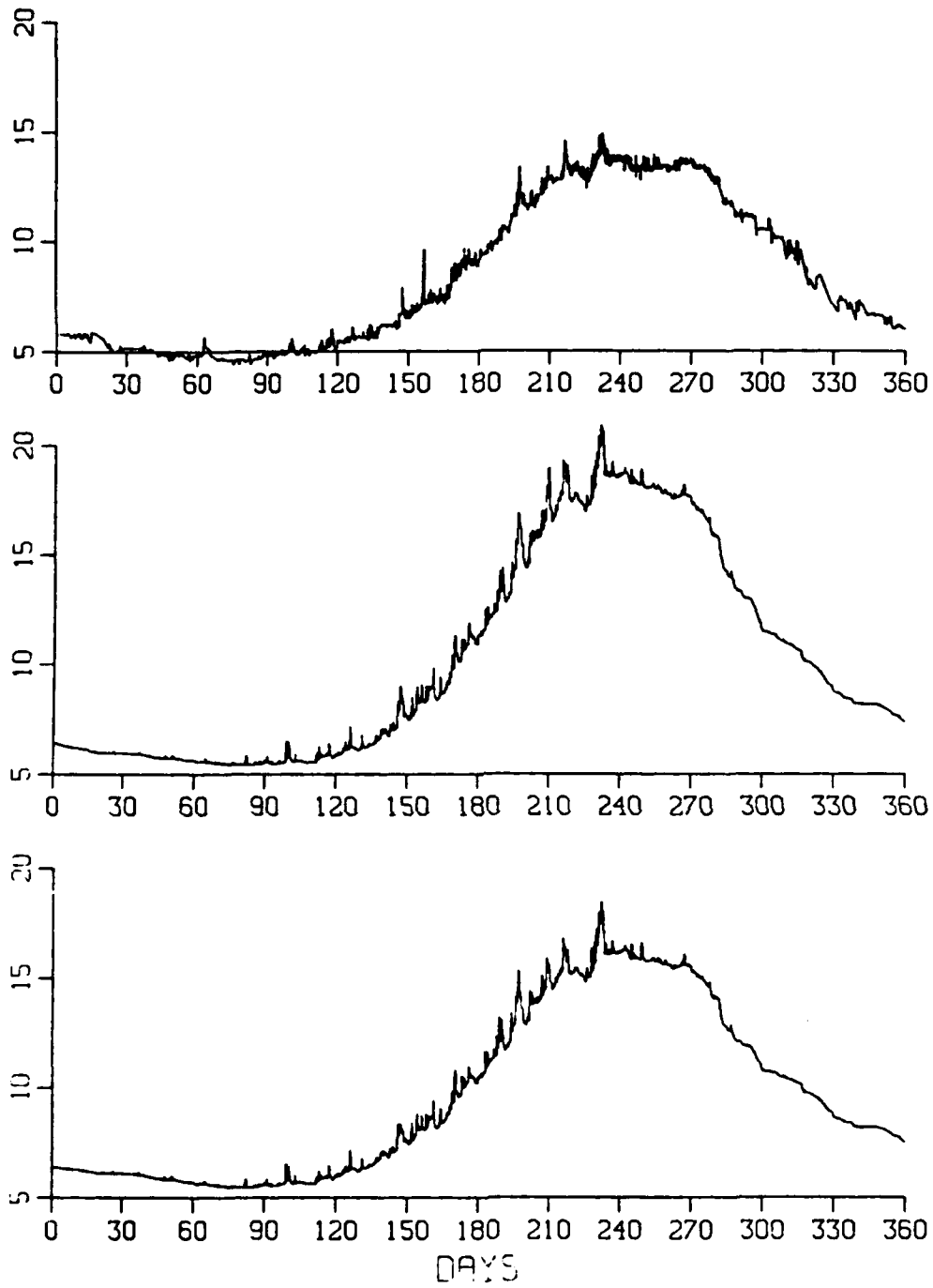


Figure 4.10b. OWS P. 1961. Mixed layer temperature: top curve is the observations, middle curve is the RSTAR model, bottom curve is the ZSTAR model.

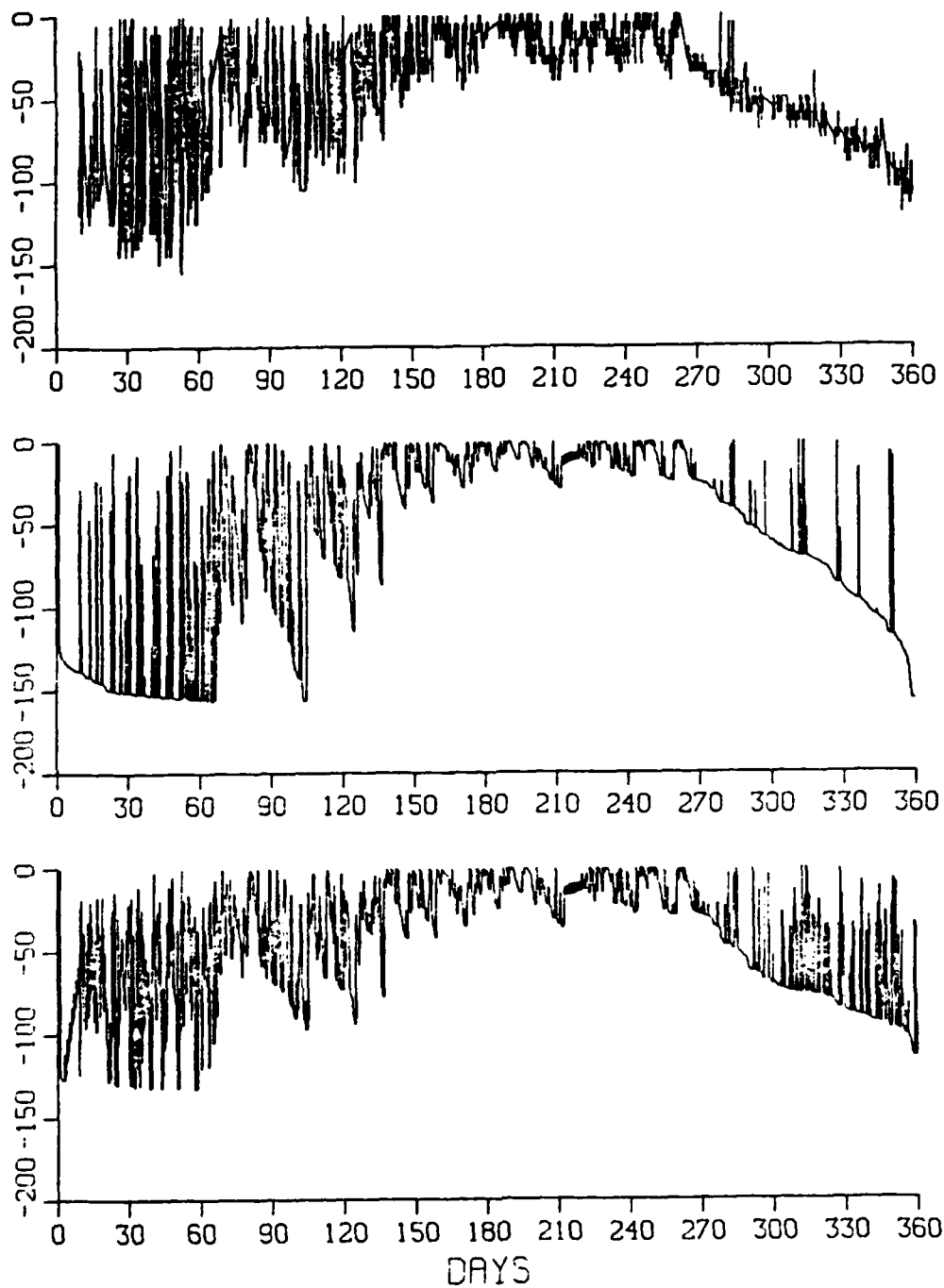


Figure 4.11a. OWS P. 1965, Mixed layer depth: top curve is the observations, middle curve is the RSTAR model, bottom curve is the ZSTAR model.

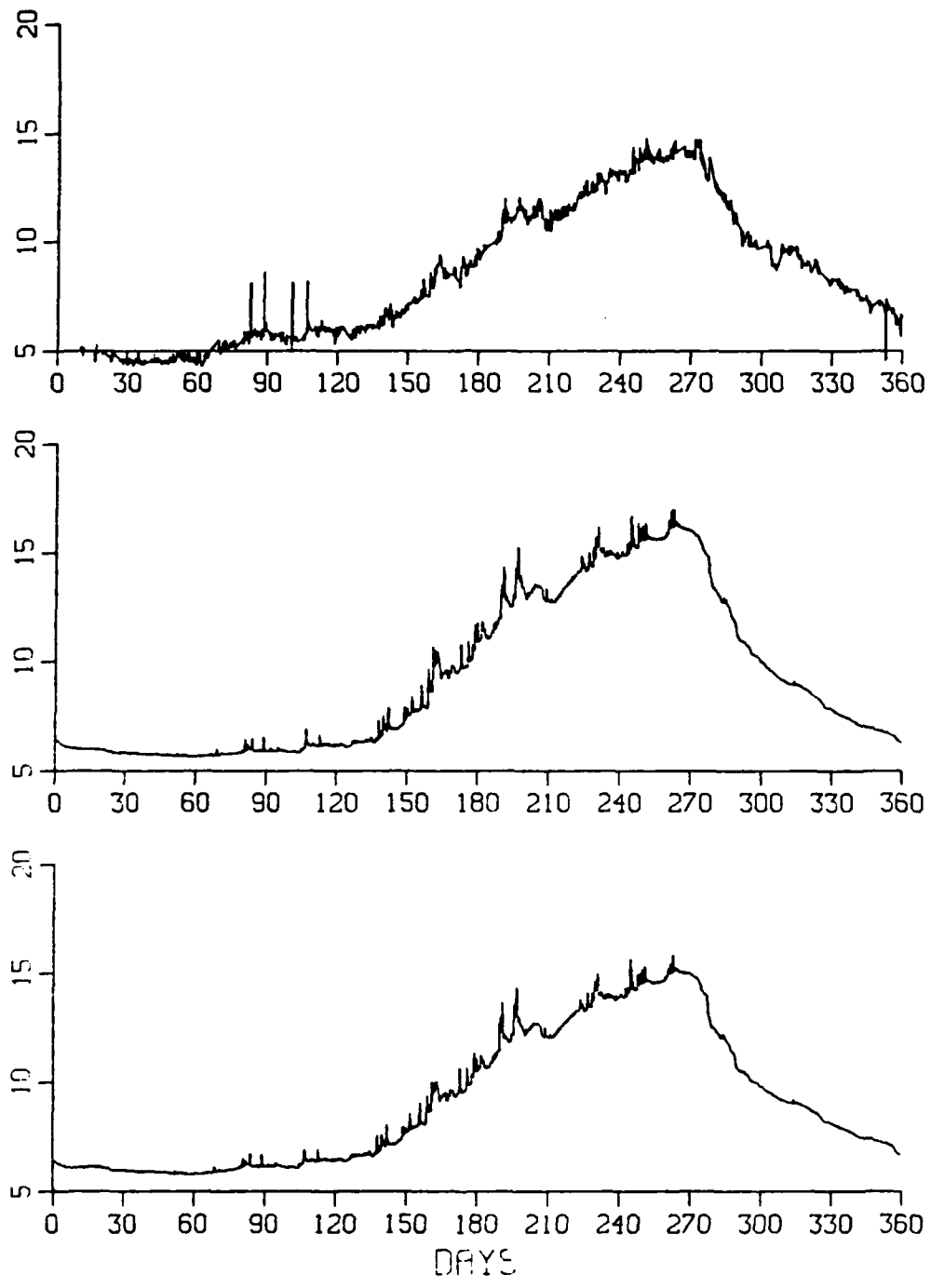


Figure 4.11b. OWS P, 1965. Mixed layer temperature: top curve is the observations, middle curve is the RSTAR model, bottom: curve is the ZSTAR model.

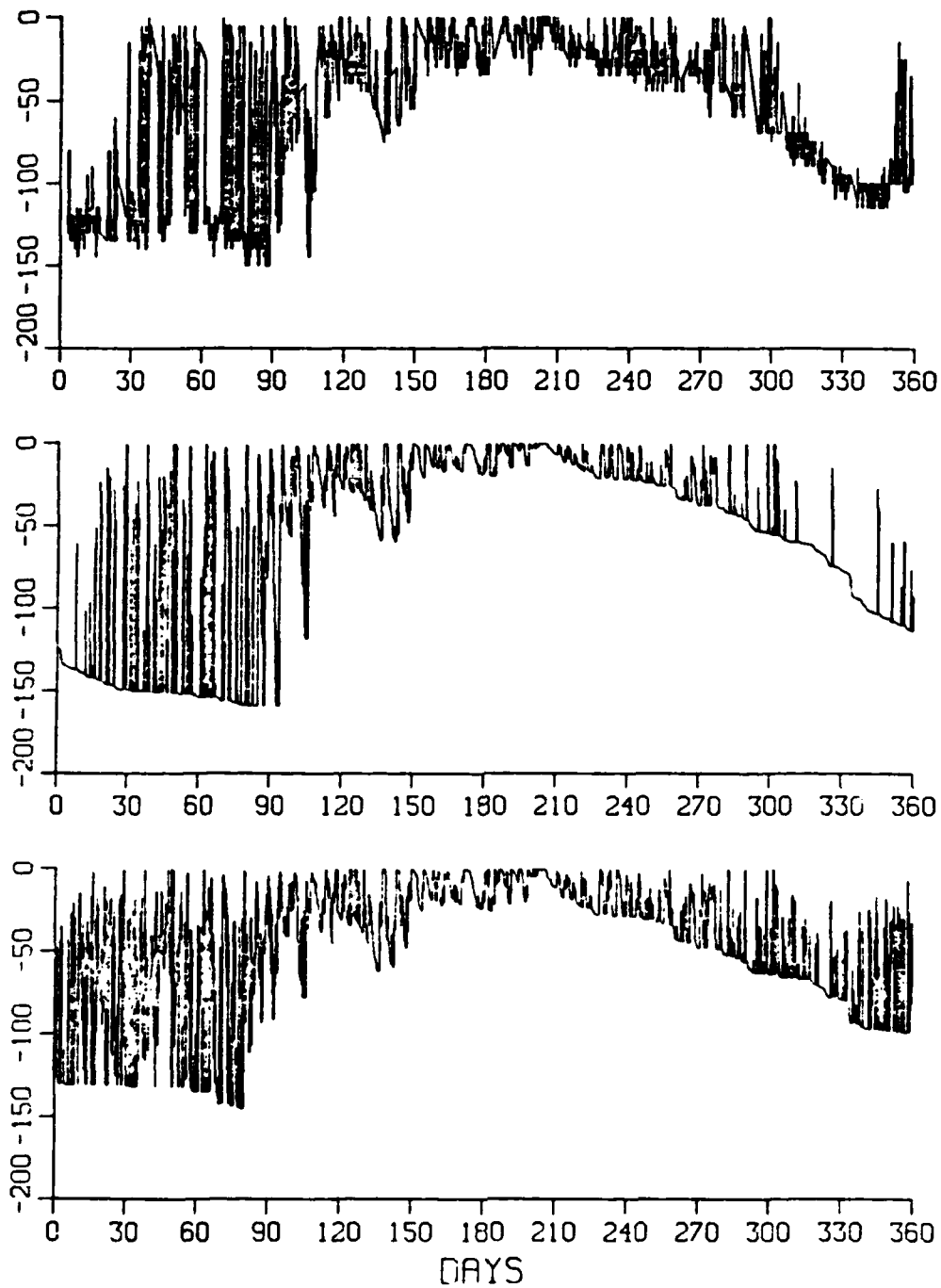


Figure 4.12a. OWS P, 1966. Mixed layer depth: top curve is the observations, middle curve is the RSTAR model, bottom curve is the ZSTAR model.

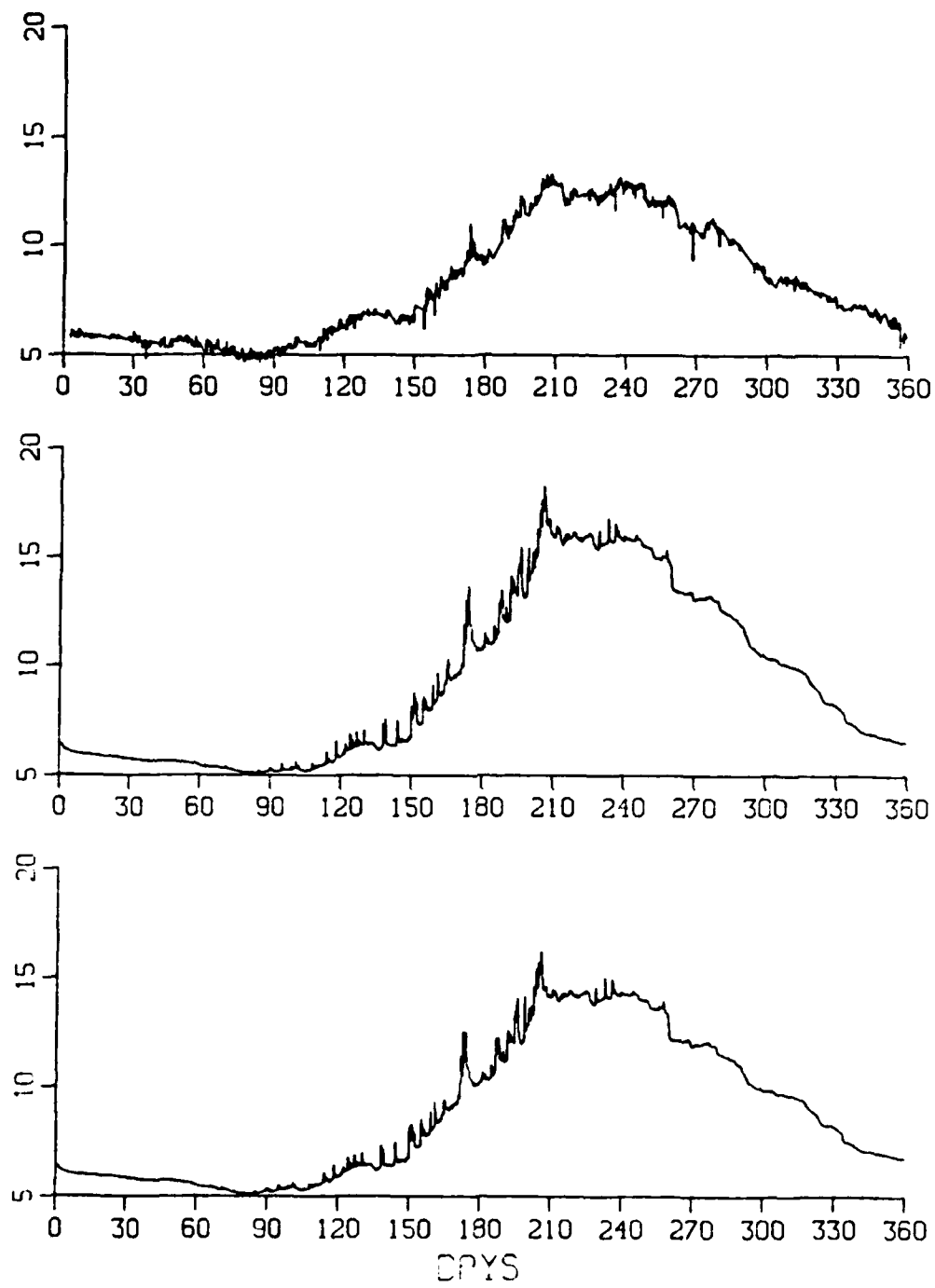


Figure 4.12b. OWS P, 1966. Mixed layer temperature: top curve is the observations, middle curve is the RSTAR model, bottom curve is the ZSTAR model.

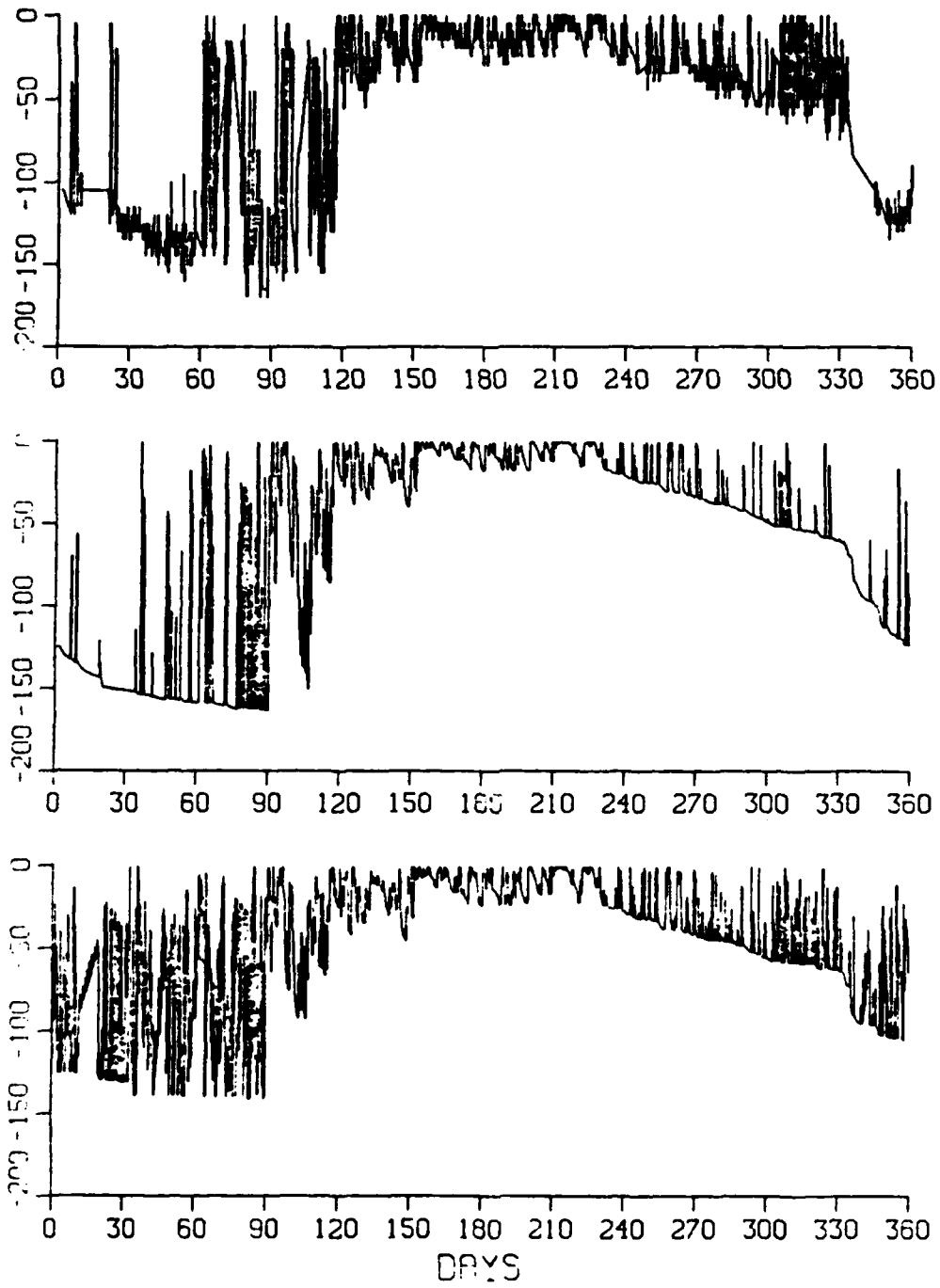


Figure 4.13a. OWS P, 1967, Mixed layer depth: top curve is the observations, middle curve is the RSTAR model, bottom curve is the ZSTAR model.

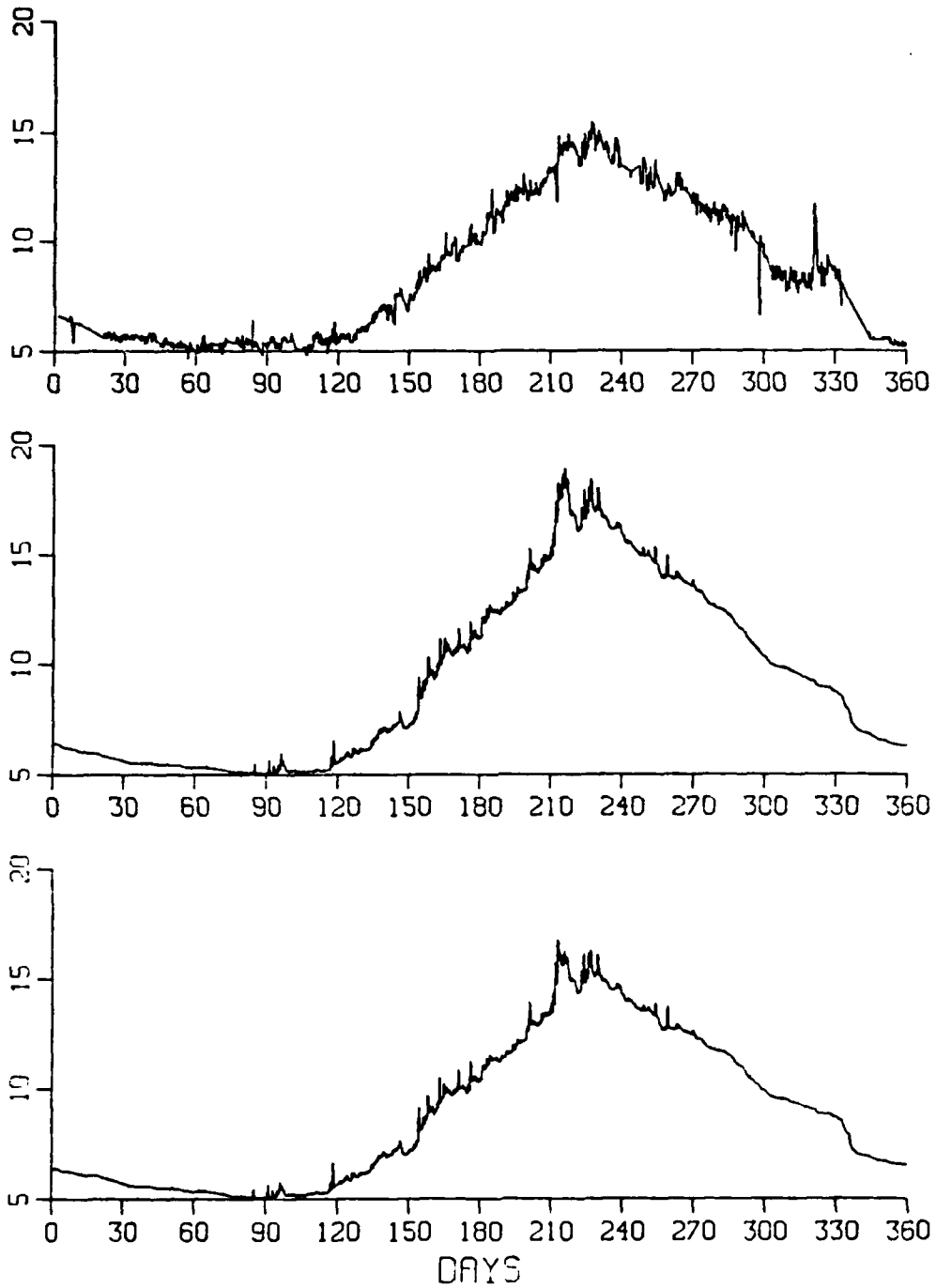


Figure 4.13b. OWS P. 1967. Mixed layer temperature: top curve is the observations, middle curve is the RSTAR model, bottom curve is the ZSTAR model.

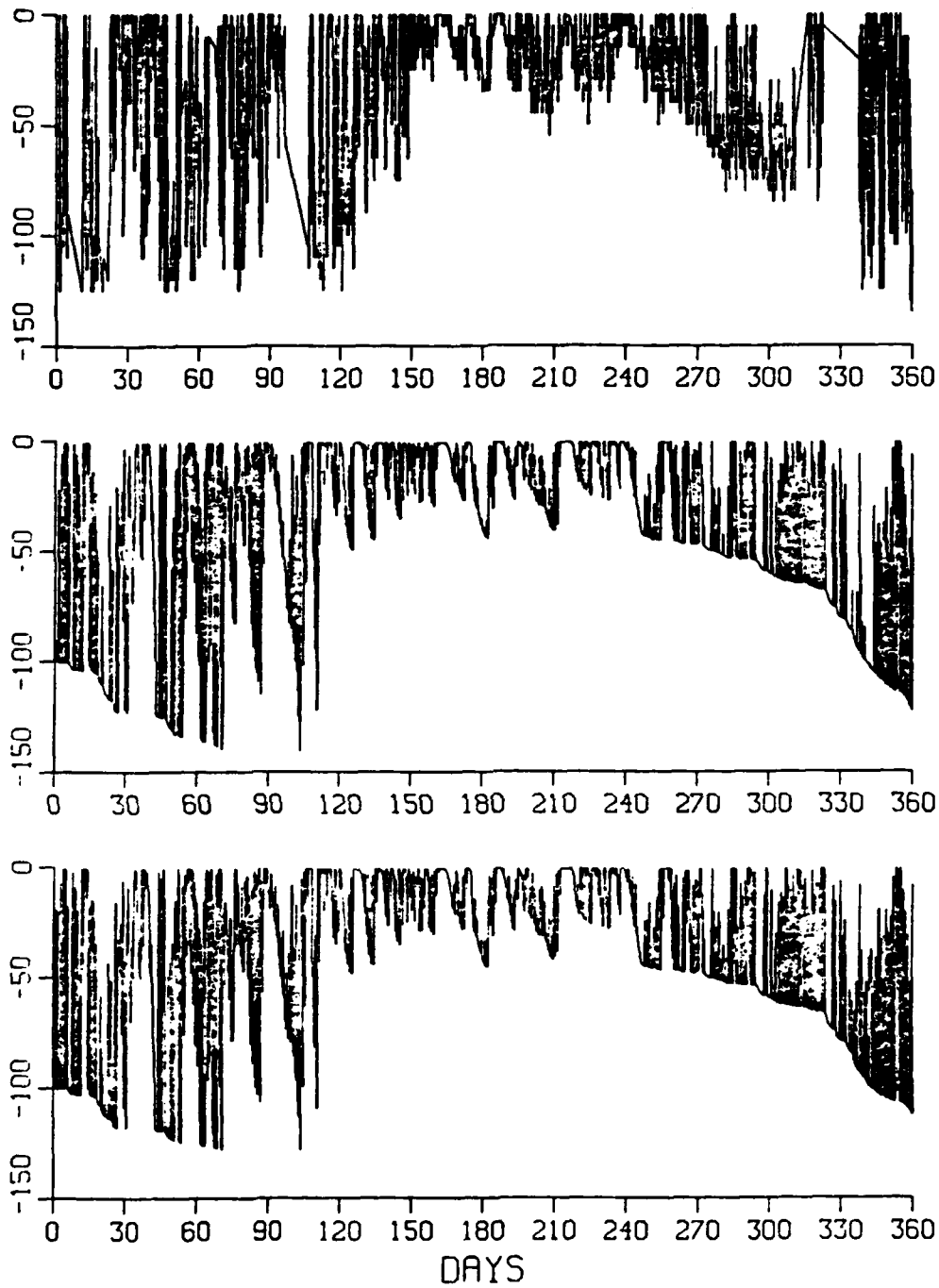


Figure 4.14a. OWS N, 1961. Mixed layer depth: top curve is the observations, middle curve is the RSTAR model. bottom curve is the ZSTAR model.



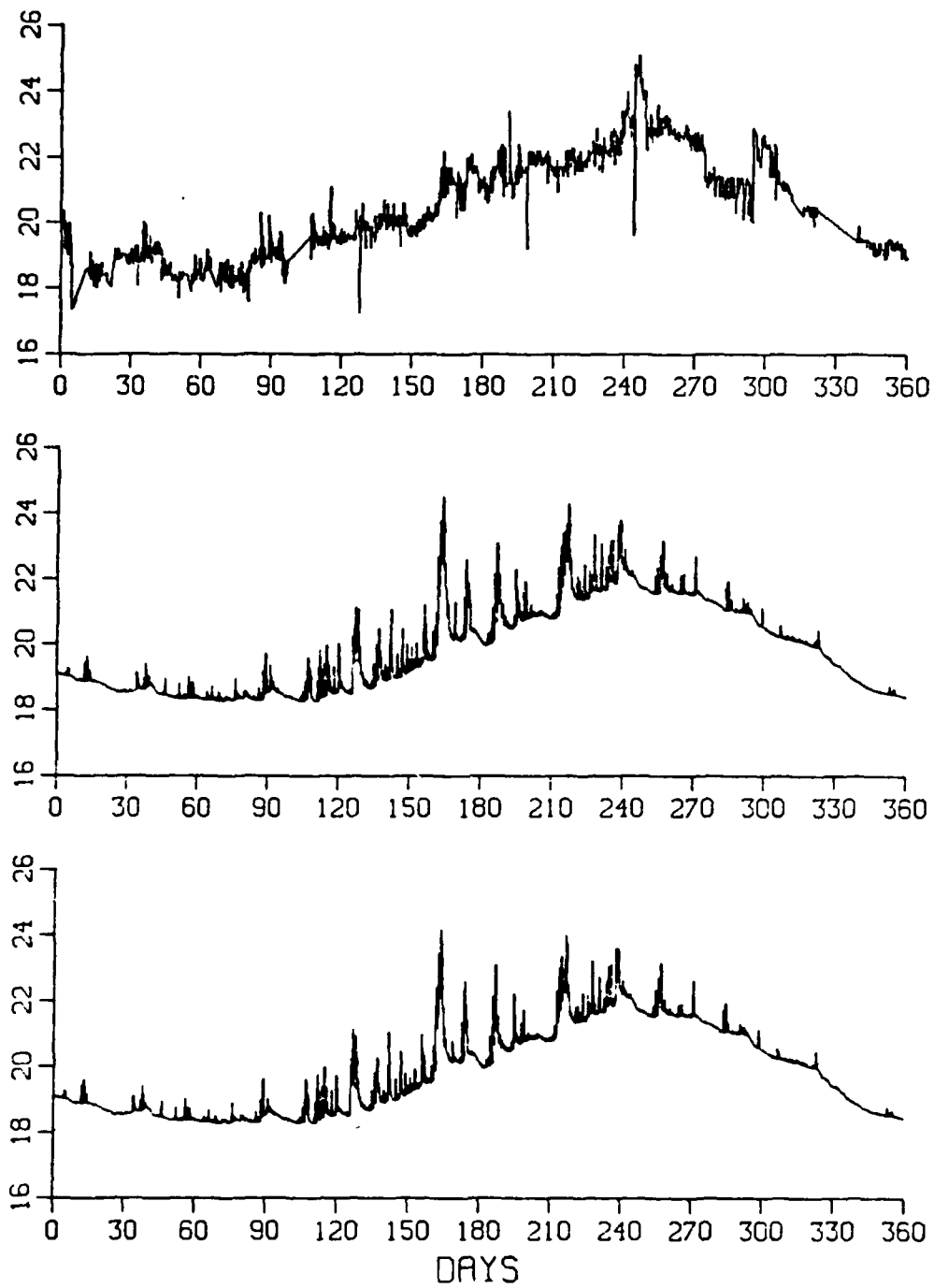


Figure 4.14b. OWS N, 1961, Mixed layer temperature: top curve is the observations, middle curve is the RSTAR model, bottom curve is the ZSTAR model.

## LIST OF REFERENCES

- Alexander, R. C., and J.-W. Kim, 1976: Diagnostic model study of mixed layer depths in the summer North Pacific. *J. Phys. Oceanogr.*, **6**, 293-298.
- Bradshaw, P., 1969: The analogy between streamline curvature and buoyancy in turbulent shear flow. *J. Fluid Mech.*, **36**, 177-191.
- \_\_\_\_\_, 1973: Effects of streamline curvature on turbulent flow. AGARDograph 169, 157 pp.
- Businger J. A., J. C. Wyngaard, Y. Izumi and E. Bradley 1971: Flux profile relationships in the atmospheric surface layer. *J. Atmos. Sci.*, **28**, 181-189.
- \_\_\_\_\_, 1982: Equations and concepts. In *Atmospheric Turbulence And Air Pollution Modelling*. F. T. M. Nieuwstabt and H. van Dop, Eds., D. Reidel, pp. 1-36.
- Cantwell, B. J., 1981: Organized motion in turbulent flow. *Ann. Rev. Fluid Mech.*, **13** 457-515.
- Champagne, F. H., V. G. Harris and S. Corrsin, 1970: Experiments on nearly homogeneous turbulent shear flow. *J. Fluid Mech.*, **41**, 81-139.
- Comte-Bellot, G., 1965: Ecoulement turbulent entre deux parois paralleles. *Publ. Sci. Tech. Ministere l'Air, Service de Documentation Scientifique et Technique de l'Armement, Paris, No. 419.*
- Cramer, H. E., 1967: Turbulent transfer processes for quasi-homogeneous flows within the atmospheric surface layer. *Phys. Fluids*, **10**, Suppl., S240-S246.
- Chou, P.-Y., 1945: On velocity correlation and the solution of the equation of turbulent fluctuation. *Q. Appl. Math.*, **3**, 38-54.
- Denman, K. L., and M. Miyake, 1973: Upper layer modification at ocean station Papa: Observations and simulation. *J. Phys. Oceanogr.*, **3**, 185-196.
- deSzoeko, R. A., and P. B. Rhines, 1976: Asymptotic regimes in mixed layer deepening. *J. Mar. Res.* **34**, 11-116.
- Dickinson, S. C., and R. R. Long, 1983: Oscillating-grid turbulence including effects of rotation. *J. Fluid Mech.*, **126**, 315-333.
- Donaldson, C. duP., 1972: Calculation of turbulent shear flows for atmospheric and vortex motions. *AAIA Jou.*, **10**, 4-12.

- Elsberry R. L., T. S. Fraim and R. N. Trapnell, Jr., 1976: A mixed layer model of the oceanic thermal response to hurricanes. *J. Geophys. Res.*, **81**, 1153-1162.
- \_\_\_\_\_, and N. T. Camp, 1978: Oceanic thermal response to strong atmospheric forcing I. The Characteristics of forcing events. *J. Phys. Oceanogr.*, **8**, 205-214.
- \_\_\_\_\_, and R. W. Garwood, Jr., 1978: Sea surface temperature anomaly generation in relation to atmospheric storms. *Bull. Am. Meteorol. Soc.*, **59**, 786-789.
- Fernando, H., 1987: Comments on 'Wind direction and equilibrium mixed layer depth: General theory'. *J. Phys. Oceanogr.*, **17**, 169-170.
- Gallacher, P. C., A. A. Bird, R. W. Garwood, Jr. and R. L. Elsberry, 1983: A determination of the constants for a second-order closure turbulence model from geophysical data. Naval Postgraduate School Technical Report NPS 63-83-004, 35 pp.
- Gallagher, B., L. Magaard, and E. Gutteling, 1981: Closure for velocity/pressure-gradient correlations in turbulent shear flow. *Phys. Fluids*, **24**, 1605-1610.
- Garratt, J. R., 1977: Review of drag coefficients over oceans and continents. *Mon. Weather Rev.*, **105**, 915-929.
- Garwood, R. W., Jr., 1976: A general model of the ocean mixed layer using a two-component turbulent kinetic energy budget with mean turbulent field closure. Technical Report, NOAA-TR-ERL-384 PMEL, 27, NTIS, U. S. Dept. of Commerce, 95 pp.
- \_\_\_\_\_, 1977: An oceanic mixed layer model capable of simulating cyclic states. *J. Phys. Oceanogr.*, **7**, 455-468.
- \_\_\_\_\_, and J. L. Yun, 1979: Bulk closure for the oceanic planetary boundary layer: a realistic and numerically efficient model. *Proc. 2nd Symposium on Turbulent Shear Flows*, Imperial College, London, pp. 12.6-12.11.
- \_\_\_\_\_, 1979: Air-sea interaction and dynamics of the surface mixed layer. *Rev. Geophys. Space Phys.*, **17**, 1507-1524.
- \_\_\_\_\_, P. C. Gallacher, and P. Muller, 1985a: Wind direction and equilibrium mixed layer depth: General Theory. *J. Phys. Oceanogr.*, **15**, 1325-1331.
- \_\_\_\_\_, P. Muller, and P. C. Gallacher, 1985b: Wind direction and equilibrium mixed layer depth in the tropical Pacific. *J. Phys. Oceanogr.*, **15**, 1332-1338.
- \_\_\_\_\_, P. C. Gallacher, and P. Muller, 1987: Reply to comments on 'Wind direction and equilibrium mixed layer depth: General theory' by H. Fernando. *J. Phys. Oceanogr.*, **17**, 171-172.

- Garzon, G., 1987: The effect of rainfall on the seasonal thermocline. M.S. Thesis, Naval Postgraduate School, 70 pp.
- Gaspar, P., 1986: Modeling the seasonal cycle of the upper ocean. Unpublished manuscript, Universite Catholique de Louvain, Belgium, 50pp.
- Geisler, J. E. and E. B. Kraus, 1969: The well-mixed Ekman boundary layer. *Deep Sea Res.*, **16**, Suppl., 73-84.
- Gibson, M. M., and W. Rodi, 1981: A Reynolds-stress closure model of turbulence applied to the calculation of a highly curved mixed layer. *J. Fluid Mech.*, **103**, 161-182.
- \_\_\_\_\_, W. P. Jones and B. A. Younis, 1981: Calculation of turbulent boundary layers on curved surfaces. *Phys. Fluids*, **24**, 386-395.
- \_\_\_\_\_, and B. E. Launder, 1978: Ground effects on pressure fluctuations in the atmospheric boundary layer. *J. Fluid Mech.*, **86**, 491-511.
- Giles, J. A., A. P. Hayes and R. A. Sawyer, 1966: Turbulent wall jets on logarithmic spiral surfaces. *Aeronaut. Q.* **17**, 201-215.
- Gill, A. E., and J. S. Turner, 1976: A comparison of seasonal thermocline models with observation. *Deep Sea Res.*, **23**, 391-401.
- Gutteling, E., 1981: Some aspects of second order closure for two dimensional turbulence. M.S. Thesis, University of Hawaii, 29 pp.
- Halleen, R. M., and J. P. Johnston, 1967: The influence of rotation on flow in a long rectangular channel - an experimental study. Report MD-18, Mech. Engr. Dept., Stanford University, 54pp.
- Hinze, J. O., 1975: *Turbulence*. Second Edition, McGraw-Hill, 790 pp.
- Hoffman P. H., K. C. Muck and P. Bradshaw 1985: The effect of concave surface curvature on turbulent boundary layers. *J. Fluid Mech.*, **161**, 371-403.
- Hopfinger E. J., F. K. Browand and Y. Gagne, 1982: Turbulence and waves in a rotating tank. *J. Fluid Mech.*, **125**, 505-534.
- Hunt I. A., and P. N. Joubert, 1979: Effects of small streamline curvature on turbulent duct flow. *J. Fluid Mech.*, **91**, 633-659.
- Ibbetson, A., and D. J. Tritton, 1975: Experiments on turbulence in a rotating fluid. *J. Fluid Mech.*, **68**, 639-672.
- Irwin, H. P. A. H., and P. A. Smith, 1975: Prediction of the effects of streamline curvature on turbulence. *Phys. Fluids*, **18**, 624-630.

- Johnston, J. P., R. M. Halleen and D. K. Lezius, 1972: Effects of span-wise rotation on the structure of two-dimensional fully developed turbulent channel flow. *J. Fluid Mech.*, **56**, 533-557.
- Johnston, J. P., 1973: The suppression of shear layer turbulence in rotating systems. *J. Fluid Mech.*, **95**, 229-236.
- Jerlov, N. G., 1976: *Marine Optics*. Elsevier, 213 pp.
- Klebanoff, P. S., 1955: Characteristics of turbulence in a boundary layer with zero pressure gradient. NACA Annual Report 41, Rept. No. 1247.
- Kim, J. W., 1976: A generalized bulk model of the oceanic mixed layer. *J. Phys. Oceanogr.*, **6**, 686-695.
- Kitaigorodsky, S. A., 1960: On the computation of the thickness of the wind mixed layer in the ocean. *Bull. Acad. Sci. U.S.S.R. Geophys. Ser.*, **3**, 284-287.
- Klein, P., and M. Coantic, 1981: A numerical study of turbulent processes in the marine upper layers. *J. Phys. Oceanogr.*, **11**, 849-863.
- Kondo, J., Y. Sasano and T. Ishi, 1979: On the wind-driven current and temperature profiles with diurnal period in the oceanic planetary boundary layer. *J. Phys. Oceanogr.*, **6**, 504-510.
- Kraus, E. B., and C. Rooth, 1961: Temperature and steady state heat flux in the ocean surface layer. *Tellus*, **13**, 231-238
- \_\_\_\_\_, and J. S. Turner, 1967: A one-dimensional model of the seasonal thermocline, part II. *Tellus*, **19**, 98-105.
- Kundu, P. K., 1980: A numerical investigation of mixed layer dynamics. *J. Phys. Oceanogr.*, **10**, 220-236.
- Large, W. G., and S. Pond, 1981: Open ocean momentum flux measurements in moderate to strong winds. *J. Phys. Oceanogr.*, **11**, 324-336.
- \_\_\_\_\_, J. C. McWilliams and P. P. Niiler, 1986: Upper ocean thermal response to strong autumnal forcing of the Northeast Pacific. *J. Phys. Oceanogr.*, **16**, 1524-1550.
- Launder, R. W., G. J. Reece and W. Rodi, 1975: Progress in the development of a Reynolds-stress turbulence closure. *J. Fluid Mech.*, **68**, 537-566.
- Leibovich, S., 1983: The form and dynamics of langmuir circulations. *Ann. Rev. Fluid Mech.*, **15**, 391-428.
- Lemasson, L., and B. Piton, 1968: Anomalie dynamique de la surface de la mer le long de l'equateur dans l'océan Pacifique. *Cashiers O.R.S.T.O.M., Ser. Oceanogr.*, **6**, 39-45.

- LeMone, M. A., 1973: The structure and dynamics of horizontal roll vortices in the planetary boundary layer. *J. Atmos. Sci.*, **30**, 1077-1091.
- Linden, P. F., 1973: The interaction of a vortex ring with a sharp density interface: a model for turbulent entrainment. *J. Fluid Mech.*, **60**, 467-480.
- List, R. L., 1984: *Smithsonian Meteorological Tables*. Smithsonian Institution Press, 527 pp.
- Lumley, J. L., and H. A. Panofsky, 1964: *The Structure of Atmospheric Turbulence*. Interscience (John Wiley and Sons), 239 pp.
- \_\_\_\_\_, and B. Khajeh-Nouri, 1974: Computational modeling of turbulent transport. In *Advances in Geophysics*, **18a**, Academic Press, 169-192.
- \_\_\_\_\_, 1978: Computational modeling of turbulent flows. In *Adv. Appl. Mech.*, **18**, 123-176.
- Martin, P. J., 1985: Simulation of the mixed layer at OWS November and Papa with several models. *J. Geophys. Res.*, **90**, 903-916.
- Maxworthy, T., 1986: On turbulent mixing across a density interface in the presence of rotation. *J. Phys. Oceanogr.*, **16**, 1136-1137.
- McPhaden, M. J., 1982: Variability in the central equatorial Indian ocean, Part I: Ocean dynamics. *J. Mar. Res.* **40**, 157-176.
- Mellor, G. L., and T. Yamada, 1974: A hierarchy of turbulence closure models for planetary boundary layers. *J. Atmos. Sci.*, **31**, 1791-1806.
- \_\_\_\_\_, 1975: A comparative study of curved flow and density-stratified flow. *J. Atmos. Sci.*, **32**, 1278-1282.
- \_\_\_\_\_, and P. A. Durbin, 1975: The structure and dynamics of the ocean surface mixed layer. *J. Phys. Oceanogr.*, **5**, 718-728.
- Meroney, R. N., and P. Bradshaw, 1975: Turbulent boundary layer growth over a longitudinally curved surface. *AIAA J.*, **13**, 1448-1483.
- Miles, J. W., 1961: On the stability of heterogeneous shear flows. *J. Fluid Mech.*, **10**, 496-508.
- Miropolsky, Yn. A., 1970: Nonstationary model of the wind-convection layer in the ocean. *Izv. Atm. and Ocean Phys.*, **6**, 1284-1294.
- Moeng, C-H., 1984: A large-eddy-simulation model for the study of planetary boundary-layer turbulence. *J. Atmos. Sci.*, **41**, 2052-2062.
- \_\_\_\_\_, and J. C. Wyngaard, 1986: An analysis of closures for pressure-scalar covariances in the convective boundary layer. Unpublished Manuscript, NCAR, Boulder, Colorado, 27 pp.

- Morris, P. J., 1984: Modeling the pressure redistribution terms. *Phys. Fluids*, **27**, 1620-1623.
- Morse, P. M, and H. Feshbach, 1953: *Methods of Theoretical Physics, Part I*, McGraw-Hill, 997 pp.
- Muck, K. C., P. H. Hoffmann and P. Bradshaw, 1985: The effect of convex surface curvature on turbulent boundary layers. *J. Fluid Mech.*, **161**, 347-369.
- Muller, P., R. W. Garwood, Jr. and J. P. Garner, 1984: Effect of vertical advection on the dynamics of the oceanic surface mixed layer. *Annales Geophys.*, **2**, 387-398.
- Niiler, P. P., 1975: Deepening of the wind-mixed layer. *J. Mar. Res.* **33**, 405-422.
- Oakey, N. S., and J. A. Elliott, 1982: Dissipation within the surface mixed layer. *J. Phys. Oceanogr.*, **12**, 171-185.
- Osborn, T. R., and R. G. Lueck, 1985: Turbulence measurements from a towed body. Unpublished manuscript, 30pp.
- Pedlosky, J., 1979: *Geophysical Fluid Dynamics*. Springer-Verlag, 624pp.
- Pollard, R. T., P. B. Rhines and R. O. R. Y. Thompson, 1973: The deepening of the wind mixed layer. *Geophys. Fluid Dyn.*, **3**, 81-404.
- Prandtl, L., 1930: Reprinted in L. Prandtl gesammelte Abhandlungen. **2**, 778, Springer, Berlin (1966).
- Reed, R. K., 1977: On estimating insolation over the ocean. *J. Phys. Oceanogr.*, **7**, 482-485.
- Reynolds, W. C., 1976: Computation of turbulent flows. *Ann. Rev. Fluid Mech.*, **8**, 183-208.
- Rotta, J. C., 1951: Statistische theorie nichthomogener turbulenz. *Z. Fuer Physik.*, **129**, 547-572.
- \_\_\_\_\_, 1967: Effect of streamwise wall curvature on compressible turbulent boundary layers. *Phys. Fluids*, **12, Suppl.**, 174-180.
- Saffman, P. G., 1980: Coherent structures in turbulent flow. In *Lecture Notes in Physics, The role of coherent structures in modelling turbulence and mixing, Proceedings of the International Conference, Madrid, Spain*, Springer-Verlag, pp. 1-9.
- Schmidbauer, H., 1936: Behavior of turbulent boundary layers on curved convex walls. Aero. Res. Council Report 2608.
- Schubauer, G. B., and P. S. Klebanoff, 1951: Investigation of separation of the turbulent boundary layer. Nat. Adv. Comm. Aero. Report 1030, 20pp.
- Schumann, U., 1977: Realizability of Reynolds stress turbulence models. *Phys. Fluids*, **20**, 721-725.

- Shaw, W. J., and J. A. Businger, 1985: Intermittency and the organization of turbulence in the near-neutral marine atmospheric boundary layer. *J. Atmos. Sci.*, **42**, 2563-2584.
- Simpson, J. J., and T. D. Dickey, 1981: The relationship between downward irradiance and upper ocean structure. *J. Phys. Oceanogr.*, **11**, 309-323.
- Smits A.J., S.T.B. Young and P. Bradshaw, 1979: The effects of short regions of high surface curvature on turbulent boundary layers. *J. Fluid Mech.*, **94**, 209-268.
- So, R.M.C., and G.L. Mellor, 1973: Experiments on convex curvature effects in turbulent boundary layers. *J. Fluid Mech.*, **60**, 43-62.
- Tabata, S., 1964: Insolation in relation to cloud amount and sun's altitude. In *Studies on Oceanography*, Y. Kozo, Ed., University of Washington Press, Seattle, pp. 202-210.
- \_\_\_\_\_, 1965: Variability of oceanographic conditions at ocean station "P" in the Northeast Pacific Ocean. *Trans. Roy. Soc. Can.*, **3**, 367-418.
- Taylor, G.I., 1935: Distribution of velocity and temperature between concentric rotating cylinders. *Proc. Roy. Soc.* **A151**, 494-512.
- Tchernia, P., 1980: *Descriptive Regional Oceanography*. Pergammon Press, 253 pp.
- Tennekes, H., and J.L. Lumley, 1972: *A First Course In Turbulence*. MIT Press, 300 pp.
- \_\_\_\_\_, 1973: A model for the dynamics of the inversion above a convective boundary layer. *J. Atmos. Sci.*, **30**, 558-567.
- Townsend, A.A., 1976: *The Structure Of Turbulent Shear Flow*. Cambridge University Press, 429 pp.
- Wallendorf, F.L., 1935: A study of the effects of curvature on fully developed turbulent flow. *Proc. Roy. Soc.* **A148**, 565-598.
- Warn-Varnas A. C., and S. A. Piacsek, 1979: An investigation of the importance of third-order correlations and choice of length scale in mixed layer modelling. *Geophys. Astrophys. Fluid Dynamics*, **13**, 225-243.
- Wyngaard, J. C., S. P. S. Arya and O. R. Cote, 1974: Some aspects of the structure of convective planetary boundary layers. *J. Atmos. Sci.*, **31**, 747-754.
- \_\_\_\_\_, 1980: The atmospheric boundary layer -- modeling and measurements. In *Turbulent Shear Flows II*, Springer-Verlag, pp. 352-365.
- \_\_\_\_\_, 1982: Boundary-layer modeling. In *Atmospheric Turbulence And Air Pollution Modelling*. F. T. M. Nieuwstabt and H. van Dop, Eds., D. Reidel, pp. 69-105.



- Wyrski, K., 1965: The average annual heat balance of the North Pacific Ocean and its relation to ocean circulation. *J. Geophys. Res.*, **70**, 4547-4559.
- Zaneveld, J. R., and R. W. Spinrad, 1980: An arctangent model of irradiance in the sea. *J. Geophys. Res.*, **85**, 4919-4922.
- Zeman, O., and H. Tennekes, 1975: A self-contained model for the pressure terms in the turbulent stress equations of the neutral atmospheric boundary layer. *J. Atmos. Sci.*, **32**, 1808-1813.
- \_\_\_\_\_, 1976: Modeling buoyancy driven mixed layers. *J. Atmos. Sci.*, **33**, 1974-1988.
- \_\_\_\_\_, 1981: Progress in the modeling of planetary boundary layers. *Ann. Rev. Fluid Mech.*, **13**, 253-272.
- Zilitinkevich, S. S., D. V. Chalikov, and Yu. D. Resnyansky, 1979: Modelling the oceanic upper layer. *Oceanologica Acta*, **2**, 219-240.

## INITIAL DISTRIBUTION LIST

		No. Copies
1.	Defense Technical Information Center Cameron Station Alexandria, VA 22304-6145	2
2.	Library, Code 0142 Naval Postgraduate School Monterey, CA 93943-5002	2
3.	Mr. Patrick C. Gallacher Code 68Ga Department of Oceanography Naval Postgraduate School Monterey, CA 93943-5000	15
4.	Prof. Roland W. Garwood, Jr. Code 68Gd Department of Oceanography Naval Postgraduate School Monterey, CA 93943-5000	2
5.	Prof. David C. Smith IV Code 68Si Department of Oceanography Naval Postgraduate School Monterey, CA 93943-5000	1
6.	Prof. Russell L. Elsberry Code 63Es Department of Meteorology Naval Postgraduate School Monterey, CA 93943-5000	1
7.	Prof. Herman E. Medwin Code 61Md Department of Physics Naval Postgraduate School Monterey, CA 93943-5000	1
8.	Dr. Rolf Lueck Suite 315 711 West 40th Street Chesapeake Bay Institute Baltimore, MD 21211	1
9.	Prof. Edward B. Thornton Code 68Tm	1

- Department of Oceanography  
Naval Postgraduate School  
Monterey, CA 93943-5000
10. Prof. Mary L. Batteen 1  
Code 68Bv  
Department of Oceanography  
Naval Postgraduate School  
Monterey, CA 93943-5000
  11. Prof. Robert H. Bourke 1  
Code 68Bf  
Department of Oceanography  
Naval Postgraduate School  
Monterey, CA 93943-5000
  12. Prof. Pecheng Chu 1  
Code 68Cu  
Department of Oceanography  
Naval Postgraduate School  
Monterey, CA 93943-5000
  13. Prof. Calvin R. Dunlap 1  
Code 68Du  
Department of Oceanography  
Naval Postgraduate School  
Monterey, CA 93943-5000
  14. Prof. Glen H. Jung 1  
Code 68Jg  
Department of Oceanography  
Naval Postgraduate School  
Monterey, CA 93943-5000
  15. Prof. Dale F. Leipper 1  
Code 68Lr  
Department of Oceanography  
Naval Postgraduate School  
Monterey, CA 93943-5000
  16. Prof. Jeffery A. Nystuen 1  
Code 68Ny  
Department of Oceanography  
Naval Postgraduate School  
Monterey, CA 93943-5000
  17. Prof. Albert J. Semtner 1  
Code 68Se  
Department of Oceanography  
Naval Postgraduate School  
Monterey, CA 93943-5000
  18. Prof. Timothy P. Stanton 1

- Code 68St  
 Department of Oceanography  
 Naval Postgraduate School  
 Monterey, CA 93943-5000
19. Dr. Thomas R. Osborn 1  
 Chesapeake Bay Institute  
 2212 Dallwood Road  
 Timonium, MD 21093
20. Dr. Christopher N. K. Mooers 1  
 INO  
 Bldg 1100  
 Room 311  
 NSTL, MS 39529
21. Prof. Peter Mueller 1  
 Department of Oceanography  
 University of Hawaii  
 1000 Pope Road  
 Honolulu, HI 96822
22. Dr. Alan Weinstein 1  
 Office of Naval Research  
 Code 1122  
 800 N. Quincy Street  
 Arlington, VA 22217
23. Dr. Alex Warn-Varnas 1  
 NORDA  
 Code 322  
 Building 1100  
 NSTL, MS 39520

END

7-87

Dtic